



저작자표시-비영리-변경금지 2.0 대한민국

이용자는 아래의 조건을 따르는 경우에 한하여 자유롭게

- 이 저작물을 복제, 배포, 전송, 전시, 공연 및 방송할 수 있습니다.

다음과 같은 조건을 따라야 합니다:



저작자표시. 귀하는 원저작자를 표시하여야 합니다.



비영리. 귀하는 이 저작물을 영리 목적으로 이용할 수 없습니다.



변경금지. 귀하는 이 저작물을 개작, 변형 또는 가공할 수 없습니다.

- 귀하는, 이 저작물의 재이용이나 배포의 경우, 이 저작물에 적용된 이용허락조건을 명확하게 나타내어야 합니다.
- 저작권자로부터 별도의 허가를 받으면 이러한 조건들은 적용되지 않습니다.

저작권법에 따른 이용자의 권리는 위의 내용에 의하여 영향을 받지 않습니다.

이것은 [이용허락규약\(Legal Code\)](#)을 이해하기 쉽게 요약한 것입니다.

[Disclaimer](#)

공학박사 학위논문

Integrated Electrochemical Sensors and Actuators for Multifunctional Surgical Endoscope and Glucose Monitoring System

다기능성 수술용 내시경과 당 모니터링
시스템을 위한 집적된 전기화학적 센서와
엑추에이터 시스템 구현

2016년 8월

서울대학교 대학원

화학생물공학부

이 현 재

Integrated Electrochemical Sensors and Actuators for Multifunctional Surgical Endoscope and Glucose Monitoring System

지도 교수 현 택 환

이 논문을 공학박사 학위논문으로 제출함
2016년 8 월

서울대학교 대학원
화학생명공학부
이 현 재

이현재의 공학박사 학위논문을 인준함
2016 년 8 월

위원장	장 정 석	(인)
부위원장	현 택 환	(인)
위원	김 대 형	(인)
위원	박 원 철	(인)
위원	이 노 현	(인)

Abstract

Integrated Electrochemical Sensors and Actuators for Multifunctional Surgical Endoscope and Glucose Monitoring System

Hyunjae Lee

School of Chemical and Biological Engineering

The Graduate School

Seoul National University

Over the past decade, flexible and stretchable electronics have achieved remarkable progress with regard to materials, designs, and manufacturing processes for biomedical applications. The electronics resolve the intrinsic mechanical mismatch between the devices and soft/curvilinear biological substrates. This enables a wide range of

applications in noninvasive, minimally invasive, and wearable devices. This dissertation includes two examples of multifunctional, flexible, and stretchable electronic systems for biomedical applications, especially in dealing with colon cancer and diabetes.

First, the multifunctional endoscope system is introduced as a minimally invasive surgical tool for colon cancer treatment. Transparent bioelectronics based on a graphene hybrid are fabricated for impedance- and pH-based colon cancer detection. Bioelectronics can ablate colon cancer by using radio frequency as a feedback therapy. The bioelectronics placed in the endoscope can provide both characterization and treatment of colon cancer without optical hindrance.

Second, wearable and/or disposable sweat monitoring devices with microneedle-based transdermal drug delivery devices are developed for noninvasive blood glucose control. The glucose in sweat is correlated with the glucose in blood, which enables sweat-based blood glucose monitoring. The sensors monitor the sweat glucose concentration with a correction based on pH, temperature, and humidity measurements for accurate sensing. A thermoresponsive microneedle with drug loading is integrated for controlled transdermal

drug delivery when hypoglycemia occurs.

The dissertation herein provides two representative examples of a multifunctional system as the basis for a closed-loop solution from disease monitoring to treatment. *In-vitro*, *ex-vivo*, and *in-vivo* experiments highlight the utility of the demonstrated technologies for colon cancer and diabetes treatment.

Key words: Flexible electronics, Stretchable electronics, Wearable electronics, Electrochemical sensors, Endoscope, Glucose monitoring system

Student Number: 2010-21007

Contents

Chapter 1 Recent advances in flexible and stretchable bio-electronic devices

1.1	Introduction	1
1.2	Bio-integrated flexible and stretchable system.....	3
1.3	Flexible and stretchable bioelectronics systems	7
1.4	Conclusion.....	19
	References	20

Chapter 2 An endoscope with integrated transparent bioelectronics for colon cancer treatment

2.1	Introduction	27
2.2	Experimental Section	30
2.3	Result and Discussion	36
2.4	Conclusion.....	67
	References	68

**Chapter 3 A graphene-based electrochemical device with
thermoreponsive microneedles for diabetes
monitoring and therapy**

3.1	Introduction	71
3.2	Experimental Section	74
3.3	Result and Discussion	84
3.4	Conclusion.....	123
	References	125

**Chapter 4 Wearable/disposable sweat glucose monitor
for non-invasive blood glucose monitoring**

4.1	Introduction	131
4.2	Experimental Section	133
4.3	Result and Discussion	140
4.4	Conclusion.....	167
	References	168

국문 초록 (Abstract in Korean)	173
----------------------------------	-----

List of Figures

Figure 1.1	Bio-integrated flexible and stretchable systems.....	6
Figure 1.2	Epidermal electronics.....	10
Figure 1.3	Invasive applications.....	13
Figure 1.4	Stretchable optoelectronic devices.. ..	16
Figure 1.5	Stretchable power supply devices.....	18
Figure 2.1	A multifunctional endoscope system.. ..	38
Figure 2.2	Schematic illustrations of tumor treatment procedures.. ...	39
Figure 2.3	Transparency and detailed designs of transparent bio-electronics.....	40
Figure 2.4	Detailed designs of transparent bio-electronics.....	41

Figure 2.5 Integration process of the transparent bio-electronics on the endoscope	43
Figure 2.6 Integration process related characterizations of the transparent bio-electronics.....	44
Figure 2.7 Transparent bio-electronic system installed on the endoscope with the external interconnection.....	45
Figure 2.8 Graphene hybrid	47
Figure 2.9 Comparison of the IrOx film quality without (left column) and with (right column) Au doping.....	48
Figure 2.10 Transparency and impedance of bio-electronics based on the graphene-hybrid	49
Figure 2.11 Material characterizations of graphene-hybrid.....	50
Figure 2.12 Electrical stability of graphene-hybrid under biofluidic	

environments.....	51
Figure 2.13 Device fabrication process	54
Figure 2.14 Characterization of tumor and pH sensors	55
Figure 2.15 Characterization of the graphene-hybrid pH sensor	56
Figure 2.16 Characterization of ablation electrodes.....	57
Figure 2.17 Comparison of the graphene-hybrid RF ablation electrode to conventional commercial RF ablation electrode	58
Figure 2.18 Characterization of contact and temperature sensors	59
Figure 2.19 Characterization of viability sensors.....	60
Figure 2.20 <i>In-vivo</i> experimental setup of the transparent bio- electronics.....	63
Figure 2.21 In-vivo colon cancer detection	64
Figure 2.22 In-vivo colon cancer therapy	65

Figure 2.23 <i>Ex-vivo</i> tumor mapping through the theranostic NPs and the transparent bio-electronics	66
Figure 3.1 <i>Ex-vivo</i> tumor mapping through the theranostic NPs and the transparent bio-electronics	86
Figure 3.2 Electrochemical and electrical characterization of the graphene-hybrid	92
Figure 3.3 Electrochemical characterization of graphene-hybrid	94
Figure 3.4 Electrochemical properties of graphene film and Au mesh/graphene	95
Figure 3.5 Reproducibility of electrochemical characterization of electrodes (Au film, Au mesh, and graphene-hybrid electrode) after functionalization	96
Figure 3.6 Mechanical characterization of the graphene-hybrid.....	97
Figure 3.7 Transparency of the array of graphene-hybrid electrochemical sensors and the heater/temperature sensor.....	98

Figure 3.8 Device fabrication process	103
Figure 3.9 Selective functionalization process of the graphene-hybrid sensors and Ag/AgCl solid-state counter electrode	104
Figure 3.10 Electrochemical and electrical characterization of individual devices	105
Figure 3.11 Characterization of glucose sensor	106
Figure 3.12 Characterization of pH sensor and pH dependency of glucose sensor	107
Figure 3.13 Combined operation of individual devices <i>in vitro</i>	108
Figure 3.14 Influence of sweat amount test on glucose and pH sensors	109
Figure 3.15 Temperature dependency of glucose/pH sensors and drug interaction test of the glucose sensor	110
Figure 3.16 Demonstration of the wearable diabetes monitoring in vivo.....	115

Figure 3.17 Portable electrochemical analyzer	117
Figure 3.18 Sweat generation, statistical correlation, and multiple reuses	118
Figure 3.19 Demonstration of the wearable therapy system <i>in vivo</i> ...	119
Figure 3.20 Fabrication process of the drug-loaded microneedles	121
Figure 3.21 Characterization of microneedles, embedded heaters, and a temperature sensor	122
Figure 4.1 Images and system design of wearable sweat monitoring patch.....	142
Figure 4.2 Images and system design of disposable sweat analysis strip.....	143
Figure 4.3 Device fabrication process	144
Figure 4.4 Miniaturization and electrode design of the glucose sensor	146
Figure 4.5 Electrochemical analysis of the planar and porous gold	

electrode	147
Figure 4.6 Sweat control layers.....	149
Figure 4.7 Sweat absorption of the disposable sweat analysis strip..	150
Figure 4.8 Reliable operation of the glucose sensor with small volume of sweat	151
Figure 4.9 Characterization of the humidity sensor	154
Figure 4.10 Characterization of the glucose sensor	155
Figure 4.11 Characterization of the glucose sensor	156
Figure 4.12 Characterization of the pH sensor	157
Figure 4.13 Characterization of the temperature sensor.....	158
Figure 4.14 Effect of pH and temperature variation on the glucose sensor.....	159
Figure 4.15 System set up for human sweat analysis by using wearable	

sweat monitoring patch	162
Figure 4.16 Human sweat monitoring by wearable sweat monitoring patch	163
Figure 4.17 Temperature stability and reuse test of the wearable sweat monitoring patch	164
Figure 4.18 Human sweat monitoring by disposable sweat monitoring strip.....	165
Figure 4.19 Human sweat analysis and correlation between glucose concentrations in sweat and blood	166

Chapter 1. Recent advances in flexible and stretchable bio-electronic devices

1.1 Introduction

Rapid advances in the design of ultrathin electronic/optoelectronic devices, sensors¹⁻³ and actuators^{4,5}, and soft biocompatible/bioresorbable encapsulating layers^{6,7} have broadened the scope of flexible/stretchable electronics from foldable displays and curved solar panels to new classes of soft bioelectronics systems that interface with the complex geometries, curved surfaces, and time dynamic tissues of the human body⁸⁻¹⁰. A wide range of biological signals, including electrophysiological (*e.g.*, electroencephalogram (EEG), electrocardiogram (ECG))^{11,12}, physiological (*e.g.*, pulse, temperature)^{13,14}, thermal (*e.g.*, thermal conductivity, temperature distribution)^{14,15}, mechanical (*e.g.*, strain, pressure)^{13,16}, and biochemical (*e.g.*, glucose, pH) information^{17,18}, continuously emanate from the human body. Each of these signals contains important clinical cues about normal bodily functions and the manifestation and progression of various

diseases¹⁹⁻²¹. There are significant challenges, however, in our ability to access target tissues/organs for high quality signal capture due to the rigid and bulky characteristics of conventional medical systems.

To achieve soft, stretchable bioelectronics requires novel approaches in material designs: i) strain minimization via nanoscale processing of established materials and ii) synthesis of new functional nanomaterials. Once bulk rigid materials are thinned and oriented into nano-structures, they become deformable. For example, the flexural rigidity of silicon nano-membranes (Si NMs) (~ 2 nm) is fifteen orders of magnitude smaller than that of silicon (Si) wafers (~ 200 μm)²². In the following, I summarize the recent state of the art in soft, flexible and stretchable electronics/optoelectronics being employed in biomedicine for implantable, minimally invasive, and wearable applications.

*** The contents of this chapter were published in *Advanced Materials* (2016, 28, 4203-4218).**

1.2 Bio-integrated flexible and stretchable system

Figure 1.1 shows examples of bio-integrated electronics/optoelectronics using flexible and stretchable devices. Electrophysiological signals from the brain (*e.g.*, EEG, electrocorticography (ECoG)) consist of complex neural activity patterns, which provide insight into normal brain function as well as neurological disorders, including epilepsy, dementia, Parkinson's disease, and restless leg syndrome (left top). Similarly, electrophysiological signals from the heart are coordinated by similar electrical signals, which provide critical insight into normal cardiac function as well as dysfunctions such as arrhythmias (center bottom). These biological signals emanate from soft and distributed cells and tissues, which are orders of magnitude smaller than the medical systems being applied to probe them. Novel microscale and nanoscale sensor designs, in arrayed formats, are thus required for measuring these fine signals. Sensor material properties, geometry (*i.e.*, surface area), and conformal interfacial contact govern the sensing properties of these systems (*e.g.*, signal to noise ratio). Furthermore, the mechanical properties of individual sensors must be closely matched with those of target organ tissues.

Additional circuits, sensors (*e.g.*, strain gauges, thermal flux sensors),

and actuators (LEDs, pacing/ablation electrodes) have been designed with these design considerations in order to enable conformal integration with soft and curvilinear organs. A few noteworthy examples include vision prosthesis systems consisting of stretchable photodiode arrays for image detection²³ and injectable flexible LED arrays for optogenetic applications²⁴ (left top). Minimally invasive systems have also exploited the soft, stretchable mechanical properties of bio-integrated electronics/optoelectronics. Instrumented balloon catheters integrated with stretchable electrodes and sensors have recently been demonstrated²⁵ to provide sensing and feedback therapy during cardiac mapping and ablation²⁶ procedures. Endovascular stents instrumented with flexible sensors and microelectronics for monitoring blood hemodynamics and the physical properties of arteries have also been recently shown to provide sensing capability onboard an otherwise purely mechanical system²⁷.

Wearable bio-integrated systems consist of a similar class of flexible/stretchable sensors and electronics as in minimally invasive and implantable applications; however, these skin-based sensors and electronics have a different set of electrical, mechanical, and optical constraints during monitoring, storing, analyzing, and transferring of data from the surface of human skin (right top)²⁸. Artificial skin instrumented with sensors and

actuators, constitutes another important branch of skin electronics for advanced prosthetics applications (left middle)²⁹. Transdermal drug delivery with pharmacological agents and activated with heat or electric field has been demonstrated in combination with these skin-based monitoring capabilities (right bottom)^{28,30}, thereby achieving both therapy and diagnostic capabilities onboard the same system. In the following sections, this chapter presents recent advances in these flexible and stretchable bioelectronic systems at the materials, device designs, and systems level, which present key demonstrations in implantable, minimally invasive, and wearable healthcare that highlight their important clinical needs.

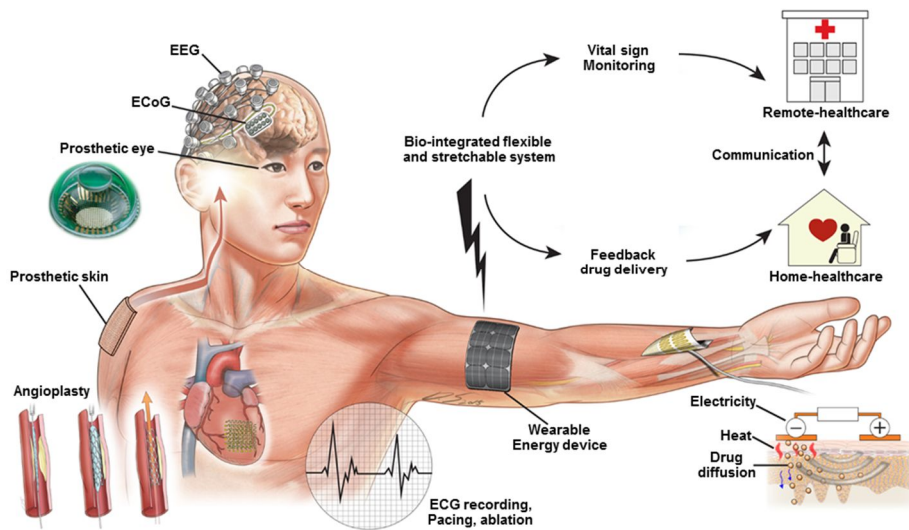


Figure 1.1. Bio-integrated flexible and stretchable systems. Schematic illustration of bio-integrated electronics in development today across a broad range of biomedical applications. Minimally invasive and implantable devices include electrophysiological sensors (ECoG, ECG), angioplasty tools, prosthetic eye²³/skin, and optoelectronic nerve stimulator, etc. Wearable bioelectronics include physiological sensors (pressure, strain, temperature sensors) integrated with transdermal drug delivery devices and data storage devices. Continuous monitoring and real time feedback therapy are performed in conjunction with the wireless communication. Energy supply module is an essential component to bioelectronics systems for mobile and personalized healthcare.

1.2 Flexible and stretchable bioelectronics systems

Soft bio-integrated electronic/optoelectronic systems require high quality materials, novel processes, and unconventional design strategies to achieve high performance as well as flexibility and stretchability. In this section, we introduce several different classes of sensors, associated circuits, and power modules in ultrathin, deformable formats to achieve differentiated mechanical properties from existing conventional electronics. These systems are applied in non-invasive, minimally-invasive and implantable applications where diagnostic monitoring and therapeutic actuation are required.

1.2.1 Epidermal electronics

Strain and/or pressure sensors are widely employed in skin-based devices to detect motions (*e.g.*, activity, tremor), cardiac signals (*e.g.*, heartbeat, pulse shape), blood pressures, respiration conditions, and mechanical properties of skin. Figure 1.2a shows flexible strain gauges composed of vertical polymer rod structures coated with platinum³¹. Resistance changes in the interlocked conducting arrays allow detection of changes in pressure, shear force, and torsion. The high sensitivity of the hair-

like sensor arrays allows capture of faint signals, like pulse from the wrist³². Figure 1.2b highlights another unique engineering approach for sensing pressure perturbations on human skin¹³. The micro-structured, soft gate dielectric of an organic transistor (left) has a measurable channel conductance, which can be modulated with an applied external pressure³³, such as pulse wave signals measured from radial artery (right).

Further improvements in the signal to noise ratio can be achieved by reducing the bending stiffness and thickness of the system, or alternatively, by enhancing adhesion of the device to the skin. Ultrathin devices below tens of micrometers in thickness with gel-type adhesives, for example, have high sensitivity (Fig. 1.2c)³⁴. Another strategy to achieve reduced stiffness is to adopt serpentine pattern designs. Mechanically optimized serpentine geometries, such as the optimized arc angle in the 2D serpentine filament, can help soft network composites to match with the mechanical property of human epidermis (Fig. 1.2d left)³⁵. These design improvements provide better conformal contact, which give rise to reduced effective impedance and noise for ECG measurements (right). Strategies that minimize stiffness are also applied for devices temperature mapping of skin (Fig. 1.2e), and/or hydration sensing based on thermal conductivity¹⁴ and elastic modulus³⁶ of skin using similar geometries and encapsulation

approaches.

A representative epidermal electronics system combines these multiple sensing modalities and device design strategies to yield a functional system of electronics and network of sensors (Fig. 1.2f)³. Other functional units integrated in the system include a display component (LED) and wireless communication units (RF coil and high frequency diode). Although these skin-based devices are successfully applied for physiological and electrophysiological sensing, thermal mapping, and wound healing measurement³⁷, high capacity ultrathin batteries, wireless communication¹¹ via radio frequency connectivity, and other optoelectronic functionality are required to achieve practical utility in clinical applications. The multifunctional epidermal electronic system can be fabricated over large area by simply cutting and transferring electronic devices onto target substrates³⁸.

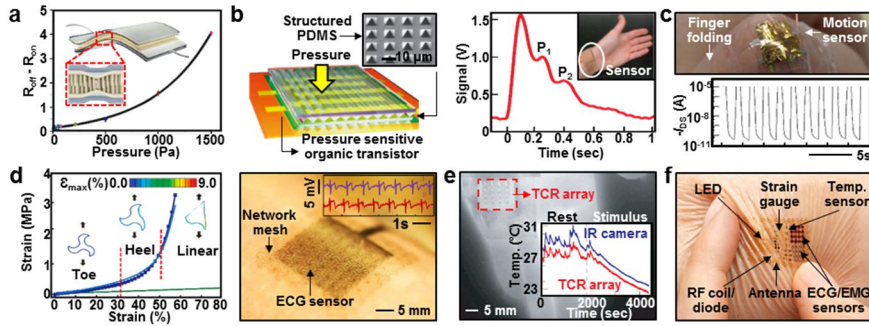


Figure 1.2. Epidermal electronics. **a**, Multiplexed, flexible strain-gauge array using an interlocked structure of Pt-coated polymer fibers³¹. **b**, Flexible polymer transistor sensors using micro-structured PDMS as a gate dielectric layer (left). The highly sensitive pressure sensor attached on the wrist monitors pulse waves from the radial artery (right)¹³. **c**, Stretchable motion sensor based on the organic transistor array detects finger motions (bottom). The device is attached by the PVA adhesive gel (top)³⁴. **d**, The stress-strain response of the soft composite with a triangular lattice geometry: experimental (blue line) and computational (line with squares) data (left). Optical image of a skin-laminated ECG sensor on the forearm. The inset shows ECG signals measured by using the devices (right)³⁵. **e**, IR camera image and corresponding temperature sensor measurement data (inset) of a palm under resting state and after stimulus¹⁴. **f**, An integrated epidermal electronic system with multiple sensors (strain, temperature, ECG, EMG sensor) and other functional units (LED, RF coil/diode, antenna)³.

1.2.2 Invasive applications

Similar to the methodology employed for epidermal electronics, invasive medical systems consisting of ultrathin, stretchable circuits exploit similar mechanical properties in order to laminate or interface on the surface of organs. Figure 1.3a shows a balloon catheter integrated with ECG/tactile/temperature/flow sensors and RF ablation electrodes²⁵. The stretchable designs are well suited for repetitive inflation/deflation cycle of the balloon, which accommodates large strains exceeding ~130%. A multifunctional system, in the format of a sleeve, contains a similar class of multifunctional devices, such as sensors for spatiotemporal epicardial monitoring (*e.g.* ECG, pH) (Fig. 1.3b)³⁹ and actuators for defibrillation and ablation⁴⁰. The soft, elastic encapsulating membrane provides robust, conformal contact with the epicardium under minimal mechanical loading stresses applied to the heart.

Incorporating high performance Si multiplexing circuits enables significant new capabilities in high spatiotemporal resolution mapping (Fig. 1.3c)⁴¹. High density, multiplexed electrode arrays consisting of active circuitry have been demonstrated to conformally contact the surface of the cortex (left) and record sleep spindles, visual evoked responses, and

micro/macro seizures (right) in live animal models. The signal quality of electrophysiological recording was further enhanced with conductive polymers, such as poly(3,4-ethylenedioxythiophene) doped with poly(styrene sulfonate) (PEDOT:PSS) as shown in Fig. 1.3d⁴². Conductive polymers that interface with cortical neurons decrease electrochemical impedance and enable high quality recordings of local field potentials and action potentials^{43,44}. Adding stretchability to sensors further enhances conformal contact, giving rise to better signal outputs. For example, the combination of an elastomeric substrate with gold nano-belts provides 130% stretchability and robust recording of ECoG from live epileptic rats (Fig. 1.3e)⁴⁵. Integration of soft microfluidic delivery mechanisms and stimulation electrodes in an e-dura mater (Fig. 1.3f left)⁴⁶ enables electrochemical and electrical stimulation on spinal cord, as a way to restore motion in paralyzed rats. The soft electrode array of the e-dura also records neural signals over cortical surfaces (right).

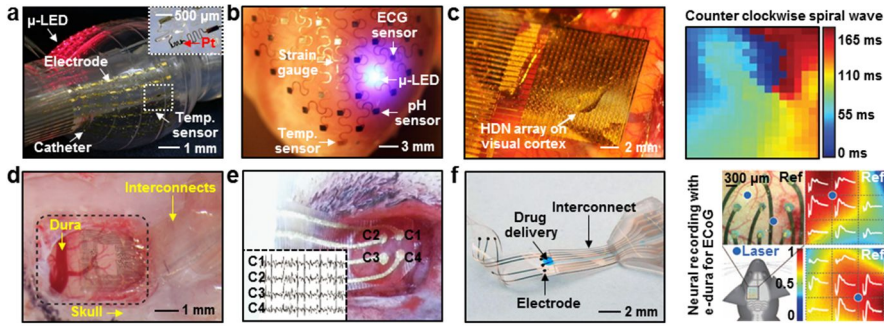


Figure 1.3. Invasive applications. **a**, Multifunctional balloon catheter in an inflated state, equipped with temperature sensors, microscale light-emitting diodes, and tactile sensors (facing downward). The inset image shows a Pt-based temperature sensor²⁵. **b**, An optical camera image of 3D multifunctional integumentary membrane (3D-MIM) with ECG electrodes, strain gauge, LED, pH sensor, and temperature sensor, enveloping a rabbit heart *ex vivo*³⁹. **c**, An optical camera image of a flexible, high-density active electrode array placed on the visual cortex of cat to map neural activities (left). Two-dimensional mapping data of a cat's brain (right)⁴¹. **d**, PEDOT:PSS-based electrodes that cover the cortical surface of a rat⁴². **e**, An optical camera image of highly stretchable gold nanobelt electrodes on a rat brain (left). ECoG signals recorded from an epileptic rat (inset)⁴⁵. **f**, An optical camera image of a soft, biocompatible electronic dura (e-dura) (left). The spatial mapping data from the e-dura during laser stimulation on the brain (right)⁴⁶.

1.2.3 Stretchable optoelectronic devices

Although optoelectronic device researches including photodetector, phototransistor, and LED are widely implemented in biomedical applications (e.g. light-based mechanical sensors⁴⁷, visual prosthesis⁴⁸, and optogenetics⁴⁹), conventional optoelectronic devices have had limitations due to the mechanical mismatch between soft, curvilinear human body and rigid optoelectronic devices. Soft, stretchable optoelectronics for stimulation and sensing provide new possibilities for phototherapy and optogenetics research, while solving these issues. Figure 1.4a left, for example, shows images of stretchable LED arrays, undergoing twisting (360° and 720°)⁵⁰. The stretchable micro-LED array can be mounted on various substrates including elastomeric ones for various medical-related functionalities. As a representative example, micro-LED arrays on an inflatable balloon catheter easily get access to the target sites inside the human body, such as endovascular and endocardial surfaces, and enable light-based sensing and therapies *in vivo*. Moreover, light-based stimulation of skin wounds using micro-LED arrays mounted on sutures can help accelerate healing processes (right). The close proximity between the LEDs and target tissue maximizes photon absorption over a given surface area. A hemispherical photodetector

array inspired by the arthropod's eye is shown in Fig. 1.4b left⁵¹. The micro-lens and hemispherical design provide wide field of view and minimize image distortions, respectively (right).

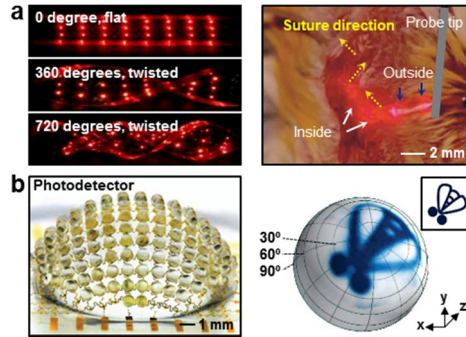


Figure 1.4. Stretchable optoelectronic devices. **a**, An optical camera images of a μ -ILED array in a flat (0°) and twisted (360° and 720°) state (left). An *in vivo* animal experiment demonstration of the light-emitting suture (right)⁵⁰. **b**, An optical camera image of a photodetector array inspired by an arthropod eye (left). An illustration of a fly is captured by the photodetectors and rendered on a hemispherical surface (right)⁵¹.

1.2.4 Stretchable power supply devices

Stretchable energy harvesting and energy storage devices that can be intimately integrated with soft bioelectronics are required for continuous power supply to portable and mobile health monitoring systems. Fig. 1.5a (left) shows a stretchable, wavy organic solar cells in stretched and unstretched configurations with active (P3HT:PCBM) and anode (PEDOT:PSS) regions⁵². This device exhibits stable performances in response to applied strains reaching ~22.2% (right). In addition to energy harvesting components, stretchable energy storage devices (*e.g.* battery, supercapacitor) are needed. Stretchable rechargeable batteries coupled together with serpentine interconnect design and the low modulus silicone elastomers can be stretched up to ~300% without noticeable dimming of the connected LED (Fig. 1.5b left)⁵³, preserving their output powers (right). Wireless power transmission successfully recharges the stretchable battery on human skin. The thin, lightweight, and flexible near field communication device is also one of the most promising wireless power supply and communication modalities⁵⁴⁻⁵⁶. These stretchable energy devices and wireless power transmission/communication units provide portability/wearability to stretchable biointegrated electronics systems.

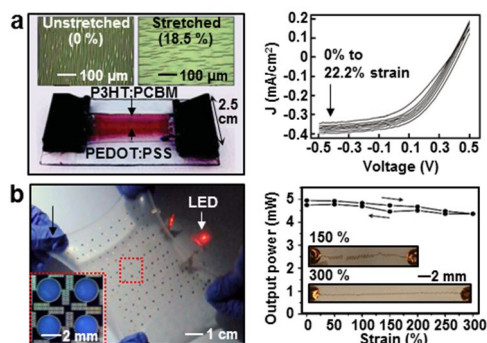


Figure 1.5. Stretchable power supply devices. **a**, A photograph of a stretchable solar cell (left) and its optical microscope images before and after 18.5% stretching (inset). Photovoltaic device characterization (I-V curve) under applied tensile strain from 0% to 22.2% (right)⁵². **b**, An optical camera image of a stretchable battery under biaxial stretching (~300%) without noticeable dimming of a red LED. The inset shows its magnified view (left). Output power data of a stretchable battery at various applied strains. The inset shows its serpentine interconnection under applied tensile strain (right)⁵³.

1.3 Conclusion

Over the past decade, advances in device designs, mechanical analysis, and micro-/nano-fabrication techniques have accelerated development of soft electronics and optoelectronics applied for biomedicine. This development in bio-electronics with unique mechanical and multifunctional characteristics is facilitated particularly with the advent of novel material strategies. Further study in optimization of materials, assemblies, surface/interface, and device designs can make the bio-electronics be effective and complete for biomedical application. Consequently, the development of new materials and processes, innovative flexible/stretchable devices, and their integrated systems for soft bio-electronics confers significant importance, whose accomplishment would extend the scope of current diagnostic and therapeutic technologies and innovate health care systems.

References

1. Kaltenbrunner, M. *et al.* An ultra-lightweight design for imperceptible plastic electronics *Nature* **499**, 458-463 (2016).
2. Drack, M. *et al.* An imperceptible plastic electronic wrap. *Adv. Mater.* **27**, 34-40 (2015).
3. Kim, D. -H. *et al.* Epidermal electronics. *Science* **333**, 838-843 (2011).
4. Tao, H. *et al.* Silk-based resorbable electronic devices for remotely controlled therapy and in vivo infection abatement. *Proc. Natl. Acad. Sci. U.S.A.* **111**, 17385-17389 (2014).
5. Farra, R. *et al.* First-in-human testing of a wirelessly controlled drug delivery microchip. *Sci. Transl. Med.* **4**, 122ra21 (2012).
6. Hwang, S.-W. *et al.* A Physically Transient Form of Silicon Electronics. *Science* **337**, 1640-1644 (2012).
7. Kim, D. -H. *et al.* Dissolvable films of silk fibroin for ultrathin conformal bio-integrated electronics. *Nat. Mater.* **9**, 511-517 (2010).
8. Yamada, T. *et al.* A stretchable carbon nanotube strain sensor for human-motion detection. *Nat. Nanotech.* **6**, 296-301 (2011).
9. Norton, J. J. S. *et al.* Soft, curved electrode systems capable of integration on the auricle as a persistent brain–computer interface. *Proc. Natl. Acad. Sci. U.S.A.* **112**, 3920 (2015).

10. Yeo, W. H. *et al.* Multifunctional epidermal electronics printed directly onto the skin. *Adv. Mater.* **25**, 2773-2778 (2013).
11. Xu, S. *et al.* Soft microfluidic assemblies of sensors, circuits, and radios for the skin. *Science* **344**, 70-74 (2014).
12. Jeong, J. W. *et al.* Materials and Optimized Designs for Human-Machine Interfaces Via Epidermal Electronics. *Adv. Mater.* **25**, 6839-6846 (2013).
13. Schwartz, G. *et al.* Flexible polymer transistors with high pressure sensitivity for application in electronic skin and health monitoring. *Nat. Commun.* **4**, 1859 (2013).
14. Webb, R. C. *et al.* Ultrathin conformal devices for precise and continuous thermal characterization of human skin. *Nat. Mater.* **12**, 938-944 (2013).
15. Park, M. *et al.* Oxide nanomembrane hybrids with enhanced mechano- and thermo-sensitivity for semitransparent epidermal electronics. *Adv. Healthc. Mater.* **4**, 992-997 (2015).
16. Lipomi, D. J. *et al.* Skin-like pressure and strain sensors based on transparent elastic films of carbon nanotubes. *Nat. Nanotech.* **6**, 788-792 (2011).

17. Bandodkar, A. J. *et al.* Tattoo-based potentiometric ion-selective sensors for epidermal pH monitoring. *Analyst* **138**, 123-128 (2013).
18. Bandodkar, A. J. *et al.* Tattoo-based noninvasive glucose monitoring: a proof-of-concept study. *Anal. Chem.* **87**, 394-398 (2015).
19. Nattel, S. New ideas about atrial fibrillation 50 years on. *Nature* **415**, 219-226 (2002).
20. Sanguinetti, M. C., Tristani-Firouzi, M., hERG potassium channels and cardiac arrhythmia. *Nature* **440**, 463-469 (2006).
21. Massey, C. A., Sowers, L. P., Dlouhy, B. J., Richerson, G. B., *Nat. Rev. Neurol.* **10**, 271-282 (2014).
22. Rogers, J. A., Lagally, M. G., Nuzzo, R. G., Synthesis, assembly and applications of semiconductor nanomembranes. *Nature* **477**, 45-53 (2011).
23. Ko, H. C. *et al.* A hemispherical electronic eye camera based on compressible silicon optoelectronics. *Nature* **454**, 748-753 (2008).
24. Kim, T. I. *et al.* Injectable, cellular-scale optoelectronics with applications for wireless optogenetics. *Science* **340**, 211-216 (2013).
25. Kim, D.-H. *et al.* Materials for multifunctional balloon catheters with capabilities in cardiac electrophysiological mapping and ablation therapy. *Nat. Mater.* **10**, 316-323 (2011).

26. Kim, D.-H *et al.* Electronic sensor and actuator webs for large-area complex geometry cardiac mapping and therapy. *Proc. Natl. Acad. Sci. U.S.A.* **109**, 19910-19915 (2012).
27. Son, D. *et al.* Bioresorbable electronic stent integrated with therapeutic nanoparticles for endovascular diseases. **9**, 5937-5946 (2015).
28. Son, D. *et al.* Multifunctional wearable devices for diagnosis and therapy of movement disorders. *Nat. Nanotech.* **9**, 398-404 (2014).
29. Kim, J. *et al.* Stretchable silicon nanoribbon electronics for skin prosthesis. *Nat. Commun.* **5**, 5747 (2014).
30. Choi, M. K. *et al.* Cephalopod-Inspired Miniaturized Suction Cups for Smart Medical Skin. *Adv. Healthc. Mater.* **5**, 80-87 (2015).
31. Pang, C. *et al.* A flexible and highly sensitive strain-gauge sensor using reversible interlocking of nanofibres. *Nat. Mater.* **11**, 795-801 (2012).
32. Pang, C. *et al.* Highly skin-conformal microhairy sensor for pulse signal amplification. *Adv. Mater.* **27**, 634-640 (2015).
33. Mannsfeld, S. C. *et al.* Highly sensitive flexible pressure sensors with microstructured rubber dielectric layers. *Nat. Mater.* **9**, 859-864 (2010).
34. Lee, S. *et al.* A strain-absorbing design for tissue-machine interfaces using a tunable adhesive gel. *Nat. Commun.* **5**, 5898 (2014).

35. Jang, K. I. *et al.* Soft network composite materials with deterministic and bio-inspired designs. *Nat. Commun.* **6**, 6566 (2015).
36. Dagdeviren, C. *et al.* Conformal piezoelectric systems for clinical and experimental characterization of soft tissue biomechanics. *Nat. Mater.* **14**, 728-736 (2015).
37. Hattori, Y. *et al.* Multifunctional skin-like electronics for quantitative, clinical monitoring of cutaneous wound healing. *Adv. Healthc. Mater.* **3**, 1597-1607 (2014).
38. Yang, S. *et al.* “Cut-and-Paste” Manufacture of Multiparametric Epidermal Sensor Systems. *Adv. Mater.* **27**, 6423-6430 (2015).
39. Xu, L. *et al.* 3D multifunctional integumentary membranes for spatiotemporal cardiac measurements and stimulation across the entire epicardium. *Nat. Commun.* **5**, 3329 (2014).
40. Xu, L. *et al.* Materials and fractal designs for 3D multifunctional integumentary membranes with capabilities in cardiac electrotherapy. *Adv. Mater.* **27**, 1731-1737 (2015).
41. Viventi, J. *et al.* Flexible, foldable, actively multiplexed, high-density electrode array for mapping brain activity *in vivo*. *Nat. Neurosci.* **14**, 1599-1605 (2011).

42. Khodagholy, D. *et al.* NeuroGrid: recording action potentials from the surface of the brain. *Nat. Neurosci.* **18**, 310-315 (2015).
43. Khodagholy, D. *et al.* Highly conformable conducting polymer electrodes for in vivo recordings. *Adv. Mater.* **23**, H268-H272 (2011).
44. Sesseolo, M. *et al.* Easy-to-Fabricate Conducting Polymer Microelectrode Arrays. *Adv. Mater.* **25**, 2135-2139 (2013).
45. Qi, D. *et al.* Highly stretchable gold nanobelts with sinusoidal structures for recording electrocorticograms. *Adv. Mater.* **27**, 3145-3151 (2015).
46. Mineev, I. R. *et al.* Electronic dura mater for long-term multimodal neural interfaces. *Science* **347**, 159-163 (2015).
47. Ramuz, M. *et al.* Transparent, Optical, Pressure-Sensitive Artificial Skin for Large-Area Stretchable Electronics. *Adv. Mater.* **24**, 3223-3227 (2012).
48. G. J. Chader, J. Weiland, M. S. Humayun, in *Neurotherapy: Progress in Restorative Neuroscience and Neurology*, Vol. 175 (Eds: J. Verhaagen, E. M. Hol, I. Huitenga, J. Wijnholds, A. B. Bergen, G. J. Boer, D. F. Swaab), Elsevier, Amsterdam, Netherlands, 317-331 (2009)
49. Deisseroth, K. *Nat. Methods* **8**, 26-29 (2011).

50. Kim, R. H. *et al.* Waterproof AlInGaP optoelectronics on stretchable substrates with applications in biomedicine and robotics. *Nat. Mater.* **9**, 929-937 (2010).
51. Song, Y. M. *et al.* Digital cameras with designs inspired by the arthropod eye. *Nature* **497**, 95-99 (2013).
52. Lipomi, D. J., Tee, B. C., Vosgueritchian, M., Bao, Z. Stretchable organic solar cells. *Adv. Mater.* **23**, 1771-1775 (2011).
53. Xu, S. *et al.* Stretchable batteries with self-similar serpentine interconnects and integrated wireless recharging systems. *Nat. Commun.* **4**, 1543 (2013).
54. Kim, J. *et al.* Miniaturized flexible electronic systems with wireless power and near-field communication capabilities. *Adv. Funct. Mater.* **25**, 4761-4767 (2015).
55. Kim, J. *et al.* Epidermal electronics with advanced capabilities in near-field communication. *Small* **11**, 906-912 (2015).
56. Huang, X. *et al.* Stretchable, wireless sensors and functional substrates for epidermal characterization of sweat. *Small* **10**, 3083-3090 (2014).

Chapter 2. An endoscope with integrated transparent bioelectronics for colon cancer treatment

2.1 Introduction

Conventional endoscopes consist of a flexible tube fitted with a camera, lens, and light delivery system, providing both maneuverability and direct visualization of the gastrointestinal tract. More advanced endoscopes allow for enhanced flexibility and maneuvering within tightly spaced orifices, while offering both diagnostic and therapeutic capabilities including tissue biopsy and resection of tumors and polyps¹. Despite the proven utility of current surgical endoscopes, onboard sensors coupled with treatments are unavailable because of the macro-scale size of conventional system, preventing diagnosis serves as effective alternative or a supplementation to surgical resection. To understand the detailed physiological dynamics and treat cancerous tissues simultaneously *in-vivo*, a new integrated system with targeted therapies and diagnostics is required^{2,3}. Radio frequency (RF)

ablation and localized photo-/chemo- therapies. The small surface area of the endoscope tip, however, limits the number of useful sensing and therapeutic features that can be integrated on endoscopes using existing packaged electronics.

Here, we demonstrate a multifunctional surgical endoscope system to diagnose and treat intestinal diseases, such as colon cancers. This ‘smart’ endoscope system contains transparent bio-electronics, which provides impedance- and pH-based sensing, in combination with RF ablation therapy to facilitate the characterization and removal of colon cancers. Additional sensors for monitoring mechanical contacts and mapping temperatures provide accurate physiological sensing capabilities during cancer detection and ablation. The transparency of devices enables optimal integration of a number of multifunctional sensing and therapeutic components on the endoscope tip without blocking the line of sight of the camera or light. By loading transparent bio-electronics on the camera of the endoscope, the tissue observed through the camera can be exactly matched with the characterized and/or ablated tissues by transparent devices. This multifunctional endoscopic system could be useful for the detection of flat or depressed neoplasms⁴ and for the treatment of patients with chronic inflammatory bowel diseases and with increased risks of developing

malignancy due to undetected dysplastic lesions⁵. The transparent bio-electronics can enhance the tumor detection accuracy and provide treatment capabilities in response to the detection.

*** The contents of this chapter were published in Nature Communications (2015, 6, 10059).**

2.2 Experimental Section

Fabrication and transfer of transparent bio-electronics: The microfabrication process begins with the deposition of a sacrificial nickel layer (100 nm, via thermal evaporation) on a handle silicon wafer. Then a bottom epoxy layer is patterned using SU8-2. The graphene is synthesized on the Cu foil through a chemical vapor deposition process. The synthesized graphene is transferred to the target substrate by the GP scooping method using PMMA A4 after the wet etching of the Cu foil. Next, the Ag NW solution (0.5 wt% in IPA) is spin-coated at 2,000 rpm, followed by the annealing at 130 °C for 1 min. Ag NW/GP layers are patterned by a photolithographic process. Ag NWs on the active sites of the temperature sensors are selectively removed to enhance the temperature monitoring sensitivity. Then, another GP layer is transferred onto Ag NW/GP layers. After patterning of the top graphene, the device is encapsulated by epoxy layer (SU8-2). External interconnection parts are also fabricated for power supply and data acquisition. These interconnections consist of a polyimide (PI) encapsulation layer and an Au/Cr metal layer, which is evaporated thermally and patterned via photolithography and etching processes. The fabricated transparent bio-electronics is transferred onto endoscope. We use

the Fujinon endoscope (ES-410WE, Fujinon; 13.0 mm of diameter, 760 mm of working channel length, flexible type) for imaging integrated devices on the endoscope. We use the Olympus endoscope (CF Type H260AL, Olympus; 13.2 mm of diameter, 1680 mm of working channel length, flexible type) for imaging the tumor by the camera of the endoscope through devices.

Electroplating IrO_x for graphene-hybrid: Prior to the electroplating of IrO_x , GP/Ag NW/GP electrodes are immersed in a 20 mM AuCl_3 solution for 10 min for doping, which enhances the uniformity of the IrO_x film deposition. The IrO_x solution for the electroplating is prepared by dissolving 150 mg of iridium tetrachloride in 100 mL of ultrapure distilled water with 20 min of stirring. 1 mL aliquot of aqueous 30 % H_2O_2 is added and stirred for 10 min, and after which 500 mg of oxalic acid dihydrate is added and stirred for another 10 min. Finally, anhydrous potassium carbonate is used to adjust the solution pH to 10.5. The resulting solution is stored at the room temperature for one week to stabilize iridium ions, resulting in a solution of the light-violet color. Electrodeposition is performed by the three-electrode method using an electrochemical analyzer. Chronopotentiometry is conducted at 0.7 V for 5 min across the graphene-hybrid working electrode,

the Pt wire counter electrode, and the Ag/AgCl reference electrode in the IrO_x solution.

Electrical stability of graphene-hybrids in biofluids: To be suitable as sensors and actuators (*e.g.* ablation electrodes) in a smart endoscope procedure, the materials of electronics have to withstand temperature fluctuations during RF ablation and exposure to multiple electrochemical cycles in bio-fluidic environments. The graphene-hybrid maintains a stable impedance value in the temperature range of 20 and 50 °C in PBS. The change in the resistance of the interconnection is small. The graphene-hybrid maintains electrochemical stability after multiple cyclic voltammetry tests in PBS. The stability of its impedance in fetal bovine serum (Life technologies, 16000) is also confirmed over 6 hours, demonstrating stable electrochemical operation in bio-fluidic environments.

***Ex-vivo* and *in-vivo* tumor sensing:** *Ex-vivo* and *in-vivo* tumor sensing is based on the detection of different impedance values between resected normal tissues and tumors (HT-29). Tumors are grown on the thigh region of a mouse (BALB/c-nude mouse). Normal tissues of the opposite thigh region are used as a control group. The resected tissues are positioned on the

working and counter electrode of tumor sensor, which are connected to an electrochemical analyzer for impedance measurements (two electrode method). *In-vivo* impedance-based tumor sensing requires conformal contacts to target tissues for precise measurements. After incision of skin, the tumor sensor directly contacted to target tumor and normal tissues. The conformal contact is confirmed with integrated contact sensors.

***In-vitro* and *in-vivo* pH sensing:** The zeta potential of the IrO_x film surface is dependent on the pH of the solution and directly affects the open circuit potential (OCP). The pH dependence of surface zeta potential is characterized using an electro-kinetic analyzer. The pH sensor is connected to an electrochemical analyzer and operated by two electrode method using pH sensitive graphene-hybrid working electrode and Au-doped GP/Ag NW/GP counter electrode. The OCP is calibrated using standard buffer solutions (pH 5, 7, 9 solution, Alfa Aesar; product # 42417, 38172, 42421). The reliability of pH sensors are tested with 10 pH sensors in repetitive uses using graphene-hybrid working electrode, platinum counter electrode, and Ag/AgCl reference electrode. The measured OCP values are converted to pH values based on the calibration curve. During the *in-vivo* experiment, pH sensor is directly contacted to the target tissues (tumor, dermis, muscle) after

incision of skin and collection of blood from the mouse. For the pH measurement of blood, heparin is added to prevent coagulation of the collected blood (5 IU heparin/mL of blood).

RF ablation and feedback monitoring: An electrochemical analyzer is used to measure the impedance change of the contact sensor, the tumor detector and the viability sensor, which are all made from the same graphene-hybrid but have different designs for each specific application. The RF ablation is conducted by connecting the ablation electrode to a RF generator and using the conventional RF ablation conditions (45~60 W). The on- and off-contact is monitored through impedance changes of the contact sensor. The temperature during the RF ablation is continuously monitored by measuring resistance changes of the temperature sensor by a digital multimeter, which is confirmed by a commercial IR camera. Tissue viability is measured impedance change through pre- and post- RF ablation.

Animal experiment and animal model of HT-29 cancer: All procedures are approved by the Institutional Animal Care and Use Committee (IACUC) of the Biomedical Research Institute of Seoul National University Hospital, and all experimental procedures are performed according to the IACUC

guidelines. HT-29 cancer cells (1×10^6) in 50 μ L of serum-free media are mixed with an equivalent volume of Matrigel (BD Biosciences). The mixture is subcutaneously injected into the flank of female BALB/c-nude mouse (aged 6-8 weeks). The maximum weight of tumors is allowed by 10 % of the weight of whole body according to IACUC (Institutional Animal Care and Use Committee) guideline. The weight of tumors does not exceed 10 % of weight of whole body during that period. All experiments are performed when the size of tumor is $100 \pm 30 \text{ mm}^3$ (2 weeks after the tumor implantation). After the photo-therapies, the mice are divided into two groups. One group is used to monitor the efficacy of the treatment. The size of tumors is checked every three days. The mice are sacrificed 20 days after the treatment. The mice in the other group are used for immunohistochemistry and sacrificed at 7 days post treatment.

2.3 Result and Discussion

2.3.1 Multifunctional endoscope system for colon cancer treatment

A representative clinical application of this smart endoscope system (Figs. 2.1a and b) involves the treatment of colon cancer as schematic illustrations described in Fig. 2.2. The treatment begins with optical observation of cancer cells (HT-29) through endoscope. Imaging of the optical information provides about the spatial distribution of cancer cells. The endoscope allows laser light to access suspicious sites exposed to NPs (Figs. 2.1a and b left). These regions are readily observed due to transparency of the integrated transparent bio-electronics on the endoscope camera, which have an overall transmittance of ~80% in the visible range (Figs. 2.3a and b). The transparent bio-electronics and associated sensors (Figs. 1a and b right) provide additional electro-chemical analysis of the tumor distribution. The detailed design of electronics is shown in Figs. 2.4a-c.

After a suspicious area of tissue is optically observed and potentially cancerous tissue is identified, these tissues are resected using forceps, followed by RF ablation using the transparent bio-electronics. Feedback modulations of this ablation therapy are based on the continuous

monitoring of temperature, contact, and cell/tissue viability. Before procedures, the transparent bio-electronics are cleaned, sterilized⁶, and attached to the endoscope (Figs. 2.5a and b). The sterilization procedure is performed using hot saturated steam in an autoclave (120 °C, 200 kPa, 15 min), which does not alter the performance of the electronics (Fig. 2.6a). The repetitive application of normal and shear stress does not change the performance of electronics (Fig. 2.6b). Note that the transparent bio-electronics can be mechanically bent and twisted without causing fractures (Figs. 2.6c and d) during the installation, removal (Figs. 2.5a and b) due to the high degree of mechanical deformability achieved by neutral mechanical plane designs^{7,8}, ultrathin structures^{9,10} and flexible properties of graphene^{11,12}. The transparent bio-electronics also shows higher mechanical reliability than indium tin oxide, which is well-known material for transparent electrodes but has brittle mechanical property (Fig. 2.6e). The transparent bio-electronics is wired to external interconnection as shown in Fig. 2.7. The simple attachment and detachment of the multifunctional transparent bio-electronic system provide the wide applicability to endoscopic devices. The multifunctional endoscopic system can be potentially used for the targeted ablation of unresectable multiple metastatic lesions^{13,14} or the natural orifice transluminal endoscopic surgery¹⁵ to detect

and treat metastatic lesions as well as primary intraluminal lesions.

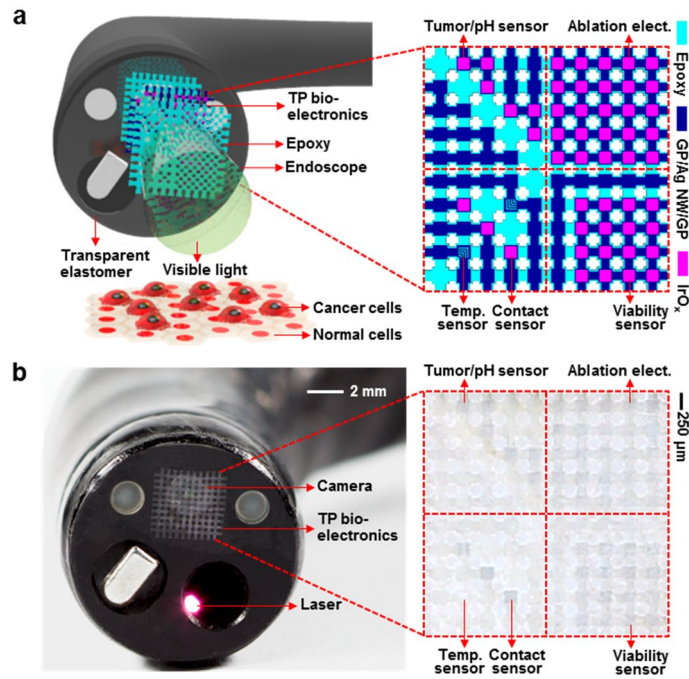


Figure 2.1. A multifunctional endoscope system. a, Schematic illustrations of the design strategy and mode of use for the multifunctional endoscope system based on transparent bio-electronic devices. **b,** Images of the system corresponding to illustrations in Fig. 2.1a.

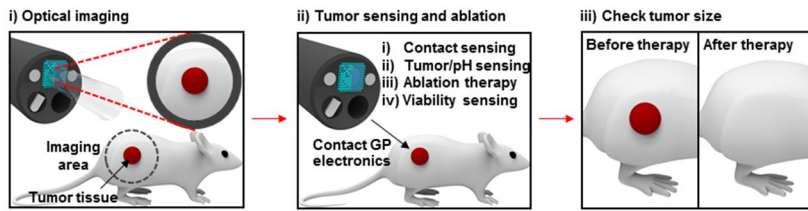


Figure 2.2. Schematic illustrations of tumor treatment procedures.

Schematic illustrations of tumor treatment procedures by using the multifunctional endoscope with integrated transparent bio-electronics.

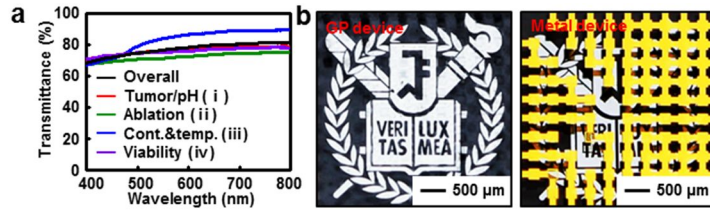


Figure 2.3. Transparency and detailed designs of transparent bio-electronics. **a**, Transparency of each device region (see Fig. 2.4 for (i), (ii), (iii), (iv)) in transparent bio-electronic devices. **b**, Comparison of the transparency between transparent bio-electronic devices and gold-based ones (control). The university logo can be clearly seen through the transparent bio-electronic electronics.

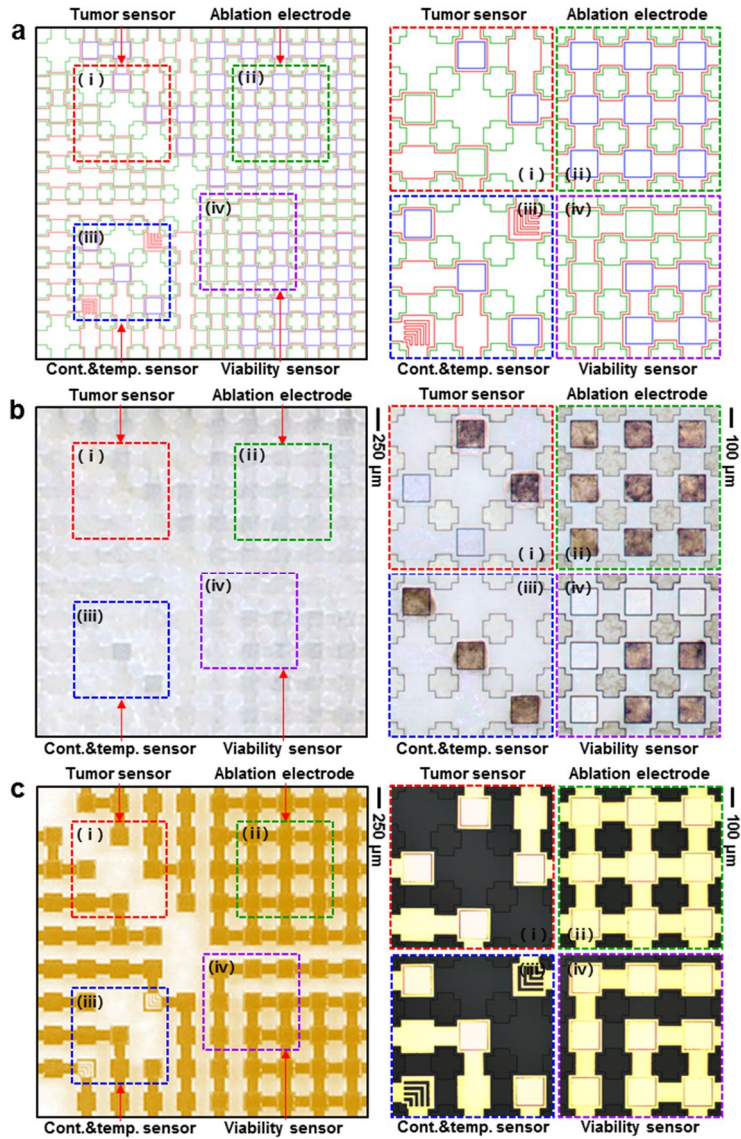


Figure 2.4. Detailed designs of transparent bio-electronics. a, CAD (computer aided design) of transparent bio-electronic devices. Right frames show the magnified view of dotted boxes ((i), (ii), (iii), (iv)). **b,** Images of transparent bio-electronic devices corresponding to CAD in Fig. 2.4a. **c,**

Images of gold-based devices corresponding to CAD of Fig. 2.4a (control sample that clearly shows the pattern of Fig. 2.4b).

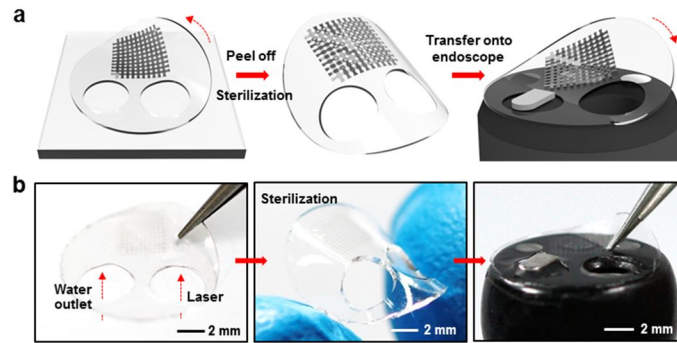


Figure 2.5. Integration process of the transparent bio-electronics on the endoscope. a, Schematic illustration of the integration process of transparent bio-electronic devices on the endoscope. **b,** Images of the integration process of transparent bio-electronic devices on the endoscope.

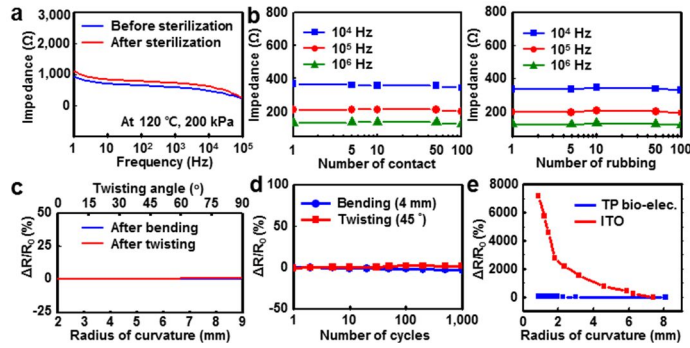


Figure 2.6. Integration process related characterizations of the transparent bio-electronics. **a**, Impedance measurements before and after the sterilization in the autoclave (120 °C, 200 kPa, 15 min). **b**, Impedance measurements in repetitive on/off-contact and rubbing tests on the pig intestine *ex-vivo*. **c**, The mechanical stability of the transparent bio-electronics is shown by measuring percentage resistance changes of transparent bio-electronics after bending (blue line) and twisting (red line) deformations at the various radius of curvature. **d**, The mechanical endurance of the transparent bio-electronics is shown by measuring percentage resistance changes of transparent bio-electronic devices in repetitive cycles. **e**, Comparison of mechanical reliability between transparent bio-electronics and ITO electrode is shown by measuring percentage resistance changes under applied strains.

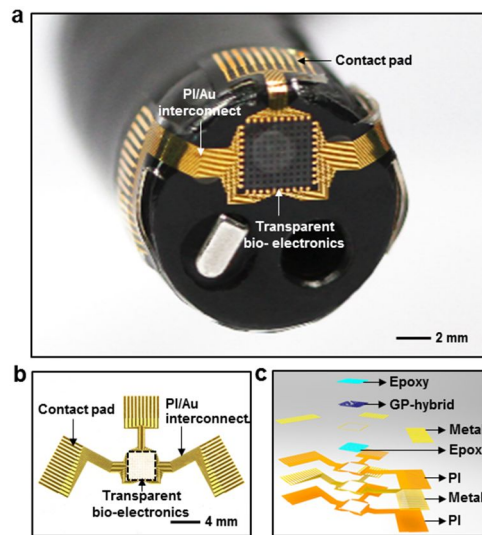


Figure 2.7. Transparent bio-electronic system installed on the endoscope with the external interconnection. a, Transparent bio-electronics installed on the endoscope. Flexible interconnections are separately fabricated and installed. **b,** Image of flexible interconnections for the transparent bio-electronics. **c,** Schematic illustration of flexible interconnections (exploded view) for the transparent bio-electronics.

2.3.2 Characterization of the graphene-hybrid

Figure 2.8 shows a schematic diagram and scanning electron microscope (SEM) images of the graphene-hybrid. CVD-grown graphene^{11,12} is modified with Au chemical doping and iridium oxide (IrO_x) deposition¹⁶. Au doping on graphene helps achieve uniform IrO_x plating (Fig. 2.9). Ag nanowires are then embedded to boost the electrical conductivity¹⁷. This hybrid structure provides good transparency (Fig. 2.10a). By selectively electroplating the IrO_x onto active sites, the device-tissue interface with low contact impedance is realized (Fig. 2.10b) with preserved high transparency. Additional characterization of graphene-hybrid is included in Fig. 2.11. The stability of graphene-hybrid immersed in biofluids at various temperatures (Fig. 2.12; including hot steam for sterilization in Fig. 2.6a) is confirmed through cyclic voltammetry tests.

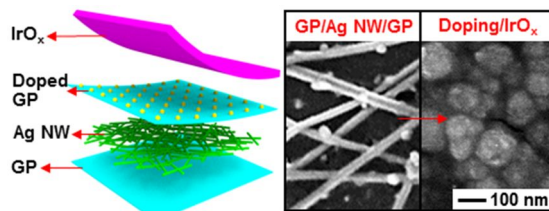


Figure 2.8. Graphene hybrid. Schematic illustration of the graphene-hybrid in the exploded view (left) and SEM images before and after the IrO_x electrodeposition (right).

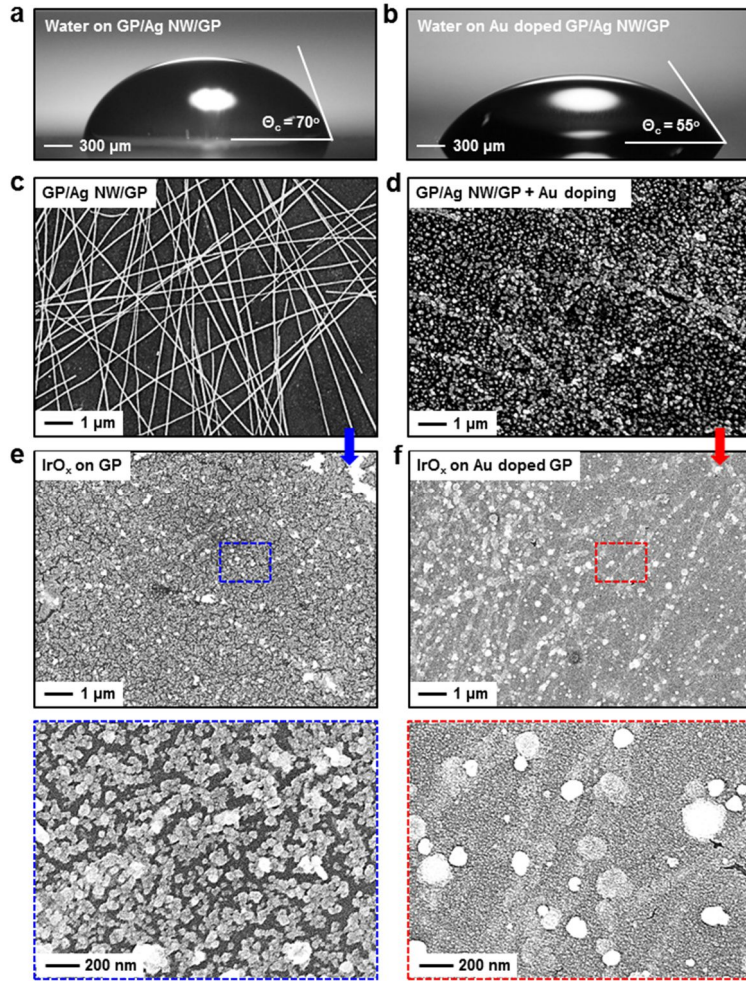


Figure 2.9. Comparison of the IrO_x film quality without (left column) and with (right column) Au doping. a, Water contact angle of GP/Ag NW/GP. b, Water contact angle of Au doped GP/Ag NW/GP. c, SEM image of GP/Ag NW/GP. d, SEM image of Au doped GP/Ag NW/GP. e, SEM images of the IrO_x film electroplated on GP/Ag NW/GP. f, SEM images of the IrO_x film electroplated on Au doped GP/Ag NW/GP.

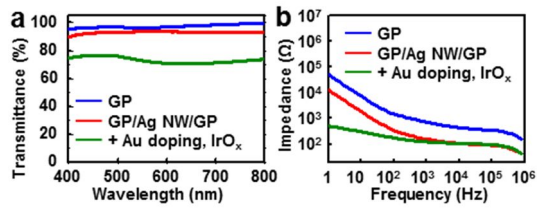


Figure 2.10. Transparency and impedance of bio-electronics based on the graphene-hybrid. a, Optical transmittance measurement of the graphene-hybrid. **b,** Bode plots of the graphene-hybrid.

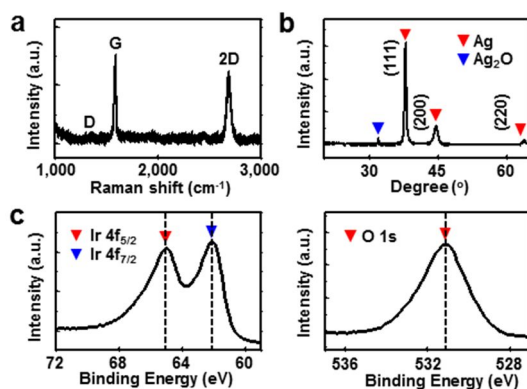


Figure 2.11. Material characterizations of graphene-hybrid. **a**, Raman spectroscopy data of the synthesized graphene. **b**, XRD (X-ray diffraction) data of Ag NWs. **c**, XPS (X-ray photoelectron spectroscopy) data of the electroplated IrO_x film.

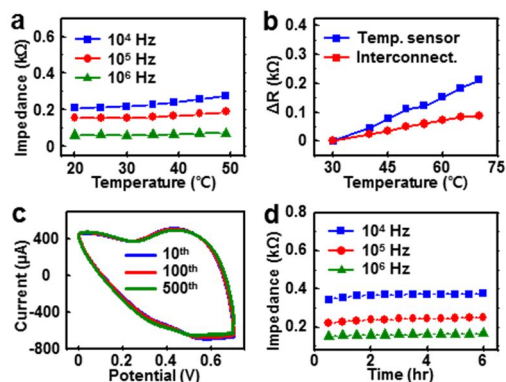


Figure 2.12. Electrical stability of graphene-hybrid under biofluidic environments. **a**, Stable impedance of graphene-hybrid at different temperatures and frequencies of the alternating current. **b**, Temperature dependent resistance changes of the temperature sensor and interconnection. Temperature sensors show higher resistance changes than the interconnection for temperature changes. **c**, Stability of the electrodeposited IrO_x film during cyclic voltammetry measurements. **d**, Stable impedance of the electroplated IrO_x film in the fetal bovine serum.

2.3.3 *In-vitro* and *ex-vivo* studies of transparent bio-electronics

Upon the completion of micro-fabrication on a handle substrate (Fig. 2.13), the transparent bio-electronics is transfer-printed onto a pre-shaped PDMS segment (Figs. 2.5a and b) and wired (Fig. 2.7). Tumor/pH sensors, ablation electrodes, and viability sensors are calibrated and characterized *ex-vivo* using both resected HT-29 tissues and healthy tissues excised from the BALB/c-nude mouse model. The tumor sensor is able to differentiate HT-29 tissues from normal tissues according to impedance differences (Figs. 2.14a and b). Shift in pH levels around tumors due to the rapid cancer metabolization serves as another important marker used to detect tumors¹⁸. We monitor pH changes by measuring the open circuit potential (OCP)¹⁶, since the surface zeta potential of graphene-hybrid has the pH dependence (Figs. 2.14c and d). After the calibration, pH sensors show reliable and stable performances over different pH ranges, by different pH sensors, and in repeated multiple uses (Figs. 2.15a-c). RF ablation studies using graphene-hybrid electrodes are conducted *in-vitro*, *ex-vivo* and *in-vivo* (Figs. 2.16a-c and Fig. 2.17). The spatial (lateral and vertical) thermal distribution of RF ablation using graphene-hybrid electrodes are compared with that using conventional commercial ablation electrodes (Boston

Scientific Corporation; Model 5031T) on agar (*in-vitro*) and BALB/c-nude mouse model (*in-vivo*), whose temperature distribution and lesion sizes are imaged with the IR and optical camera, respectively (Fig. 2.17). Both electrodes show similar results. To control lesion profiles effectively, conformal contact and temperature are constantly monitored during ablation (Figs. 2.18a-c). Finally, the viability sensor differentiates ablated tissues from non-ablated ones by measuring local impedance changes (Figs. 2.19a-c). Although the direct mapping of the 3D thermal profile during RF ablation is challenging, it is clinically important. Previous reports provide a theoretical model for the prediction of the 3D thermal profile during the ablation by using the 2D surface temperature profile and the lesion size¹⁹.

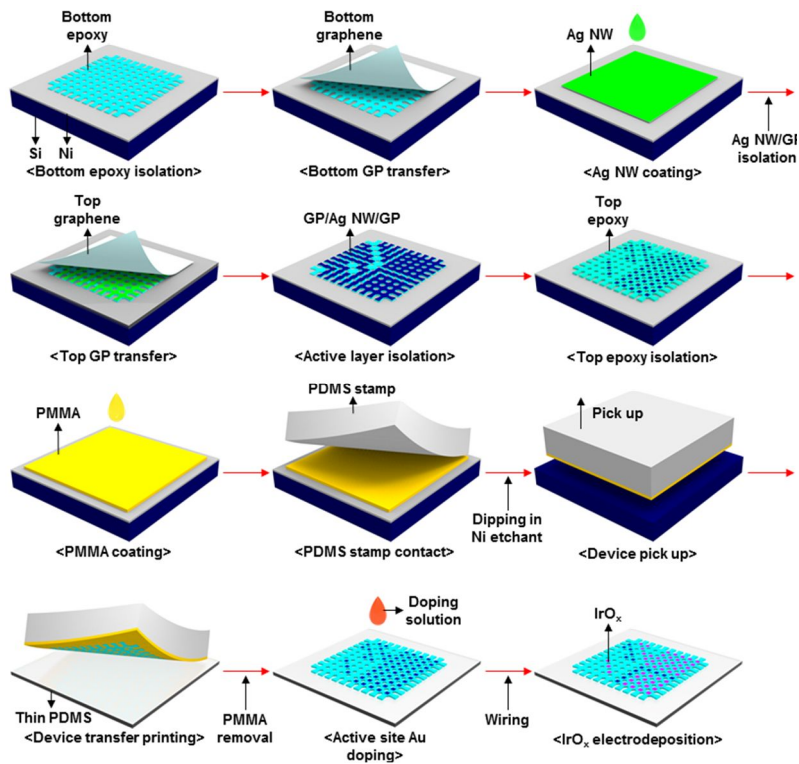


Figure 2.13. Device fabrication process. Schematic illustrations of the microfabrication process of transparent bio-electronic devices on a handle substrate.

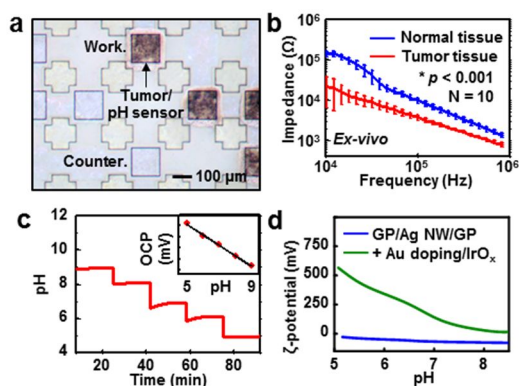


Figure. 2.14. Characterization of tumor and pH sensors. **a**, Optical microscope image of tumor and pH sensors. **b**, impedance measurement of tumor (HT-29) and normal tissues *ex-vivo* (mouse number = 10; $*p < 0.001$, Student's t-test). **c**, pH monitoring in sequential additions of the acidic buffer solution). Working and counter electrodes for electrochemical measurement are shown in the top frame. **d**, Zeta potential changes of GP/Ag NW/GP and graphene-hybrid at different pHs.

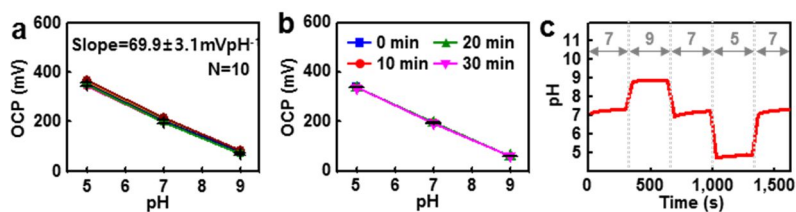


Figure 2.15. Characterization of the graphene-hybrid pH sensor. a, Open circuit potential changes as a function of pH, measured by using 10 different pH sensors. **b,** Open circuit potential changes as a function of pH in repeated uses with different time scales. **c,** Characterization of pH sensors in standard buffer solutions whose pH changes $7 \rightarrow 9 \rightarrow 7 \rightarrow 5 \rightarrow 7$.

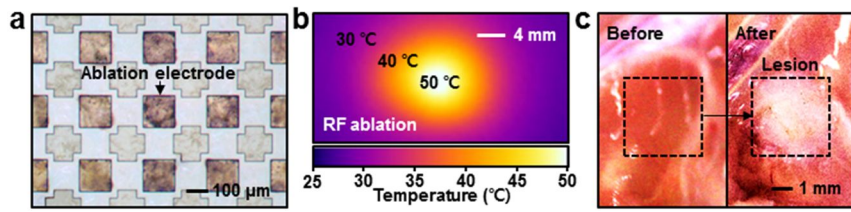


Figure 2.16. Characterization of ablation electrodes. **a**, Optical microscope image of ablation electrode. **b**, IR camera image during the RF ablation. **c**, optical camera images before and after RF ablations of mouse thigh tissues *ex-vivo*.

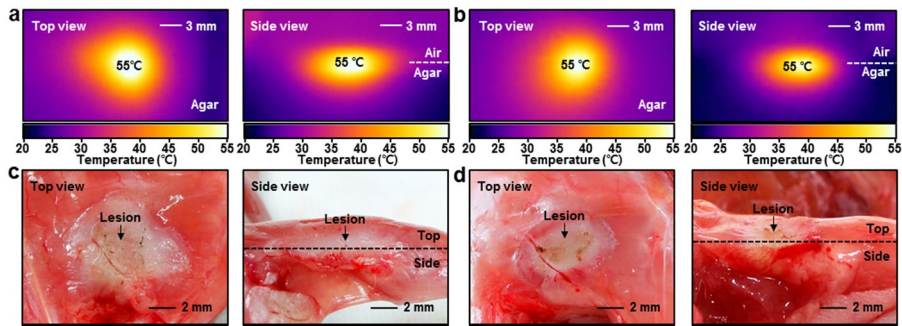


Figure 2.17. Comparison of the graphene-hybrid RF ablation electrode to conventional commercial RF ablation electrode. **a**, IR images of agar during RF ablation using the graphene-hybrid based electrode (left: top view, right: side view). **b**, IR images of agar during RF ablation using conventional commercial ablation electrode (left: top view, right: side view). **c**, Optical camera images of the lesion size and depth on the mouse thigh muscle after RF ablation *in-vivo* using the graphene-hybrid ablation electrode (left: top view, right: side view). **d**, Optical camera images of the lesion size and depth on the mouse thigh muscle after RF ablation *in-vivo* using conventional commercial ablation electrode (left: top view, right: side view).

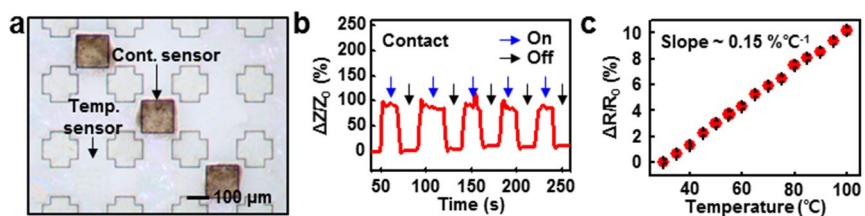


Figure 2.18. Characterization of contact and temperature sensors. a, Optical microscope image of contact and temperature sensors. **b,** Impedance measurements in on- and off-contacts. **c,** Calibration curve of the temperature sensor.

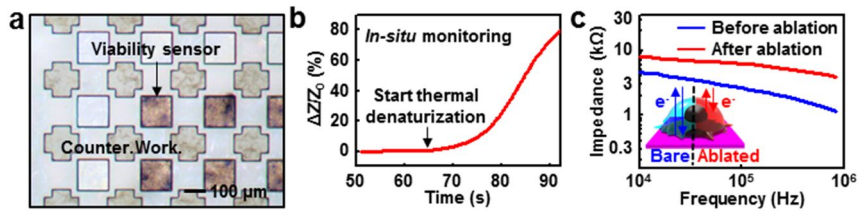


Figure 2.19. Characterization of viability sensors. **a**, Optical microscope image of viability sensor. **b**, *In-situ* impedance measurement during the thermal denaturation of mouse tissues. **c**, bottom: impedance measurement before and after the RF ablation of tumor tissues.

2.3.4 *In-vivo* colon cancer treatment.

The transparent electronics system on the endoscope can be applied to *in-vivo* models. The *in-vivo* experimental set-up is shown in Fig. 2.20. Endoscopic treatment is conducted on colon cancer (HT-29) grown on the sub-dermis surface of BALB/c-nude mouse. Since colon cancer models are not available in large animals and endoscopes are too large for gastrointestinal tracts of small animals, we conduct *in-vivo* studies using mouse subcutaneous colon cancer models.

Images of the tumor-grown surface captured by the endoscope camera reveal that the transparent bio-electronics do not disturb the visual observation, while the control standard metal device causes severe interferences (Fig. 2.21a). Upon identifying the cancerous cells, RF ablation therapy is employed to destroy the tumors. In this case, contact sensors are used to detect conformal contacts between electronics and tissues (Fig. 2.21b). In the contact mode during RF ablation, the visual observation of tumors is unavailable. Therefore, the impedance-based tumor and pH sensors are used to locate cancer tissues (Fig. 2.21c,d), according to the lower impedance and pH levels of tumor cells. The calibrated impedance and pH sensor successfully detects pH of target tissues *in-vivo* under the contact

mode (Fig. 2.21d). Monitoring temperature changes (Fig. 2.22a) provides additional guidance during RF ablation (Fig. 2.22b). Finally, tissue viabilities are measured to confirm the ablation therapy (Fig. 2.22c). We also conduct *ex-vivo* studies using mouse colon cancer tissues attached on a porcine colon to show potential applicability of a current system to large animals (Fig. 2.23). Although the experiment is conducted *ex-vivo*, the results validate proper operation of designed device structure.

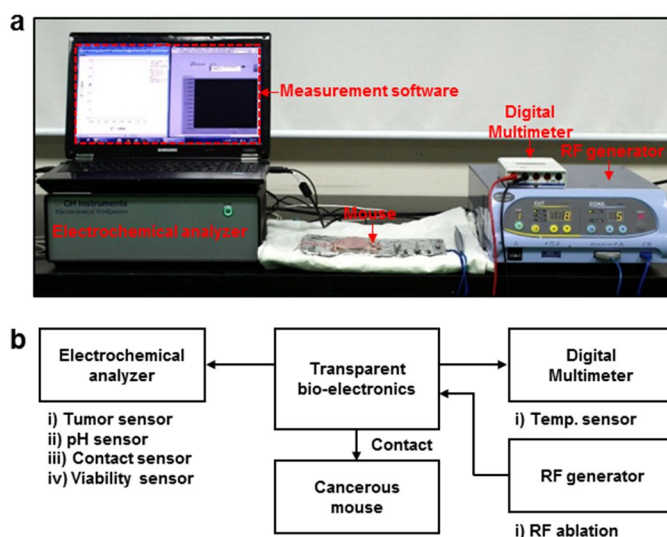


Figure. 2.20. *In-vivo* experimental setup of the transparent bio-electronics. **a**, Image of the *in-vivo* experimental setup of the transparent bio-electronic system including the electrochemical analyzer and the RF ablation therapy equipment. **b**, Schematic diagram of the *in-vivo* experimental setup of the transparent bio-electronic system.

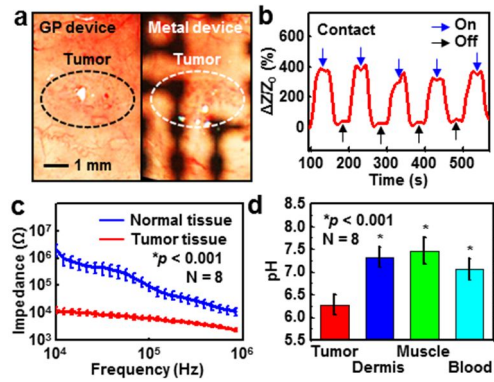


Figure 2.21. In-vivo colon cancer detection. **a**, Images of the tumor, captured by the camera of the endoscope through electronic devices (left: through transparent bio-electronic devices, right: through control metal devices). **b**, Contact sensing of tumors on the mouse sub-dermis. **c**, Tumor detection using the subcutaneous colon cancer model in the BALB/c nude mouse (mouse number = 8; $*p < 0.001$, Student's t-test). **d**, pH measurements of the tumor tissue, dermis tissue, muscle tissue, and blood of the corresponding mouse model (mouse number = 8; $*p < 0.001$, Student's t-test).

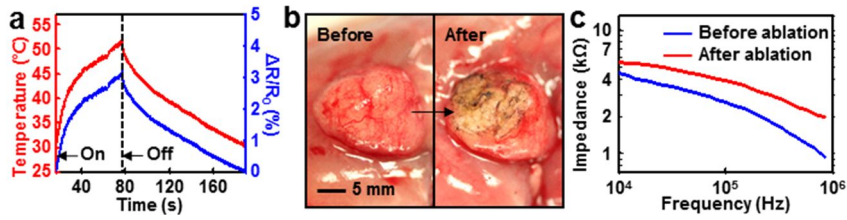


Figure. 2.22. *In-vivo* colon cancer therapy. **a**, *In-situ* temperature measurement during the RF ablation therapy. **b**, Images of tumor tissues before and after the RF ablation therapy. **c**, Viability sensing before and after the ablation therapy of tumor tissues.

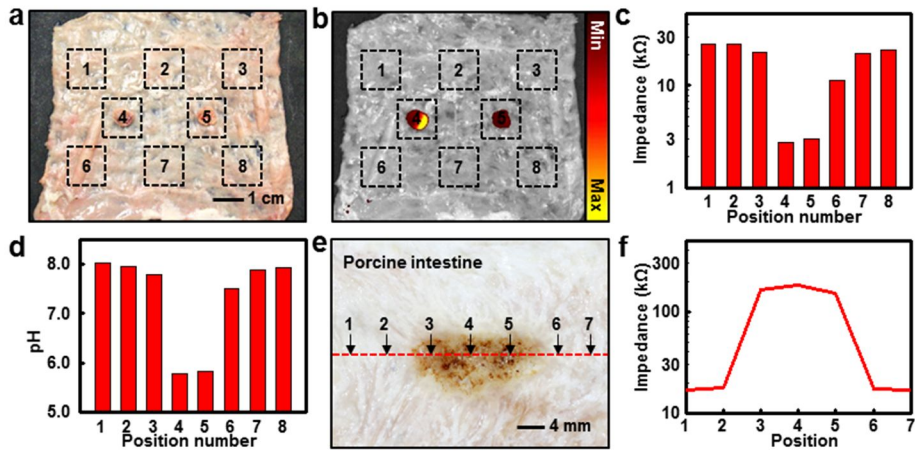


Figure 2.23. Ex-vivo tumor mapping through the theranostic NPs and the transparent bio-electronics. (a) An optical camera image of nanoparticle-targeted tumors attached to porcine intestine. The tumor is resected from tumor tissues grown on subdermal tissues of mouse. (b) IVIS fluorescence image corresponding to Fig. 2.23a. (c) Impedance mapping of tumors attached porcine intestine by using the tumor sensor (operation frequency: 10^4 Hz). The sensing positions are shown in Fig. 2.23a. (d) pH mapping of tumors attached porcine intestine by using the pH sensor. The sensing positions are shown in Fig. 2.23a. (e) An optical camera image of porcine intestine after RF ablation. (f) Viability mapping of porcine intestine after RF ablation by using the viability sensor. The sensing positions are shown in Fig. 2.23a (operation frequency: 10^4 Hz).

2.4 Conclusion

Materials, designs, and integration strategies for advanced, transparent bio-electronics onboard multifunctional endoscope systems have the potential to reduce the procedure time and improve the efficiency of minimally invasive surgical procedures for colon cancer treatment. These multifunctional endoscopic system for simultaneous *in-vivo* histologic detection, delineation, and rapid targeted treatment will be substantial for reduction of missed lesions, whether they are intraluminal mucosal lesion or extraluminal metastatic lesion. Furthermore, efficient therapy can contribute to the excellent oncologic and economic yield for various gastrointestinal cancers or precancerous lesions in the future. These systems facilitate access to internal organs and provide a significant amount of diagnostic feedback during treatment routines, thus highlighting the utility of this technology in the translational medicine.

References

1. Balog, J. *et al.* Intraoperative tissue identification using rapid evaporative ionization mass spectrometry. *Sci. Transl. Med.* **5**, 194ra93 (2013).
2. Tennant, D. A., Duran, R. V. & Gottlieb E. Targeting metabolic transformation for cancer therapy. *Nat. Rev. Cancer* **10**, 267-277 (2010).
3. Vanneman, M. & Dranoff, G. Combining immunotherapy and targeted therapies in cancer treatment. *Nat. Rev. Cancer* **12**, 237-251 (2012).
4. Kudo, S. *et al.* Colonoscopic diagnosis and management of nonpolypoid early colorectal cancer. *World J. Surg.* **24**, 1081–1090 (2000).
5. Mayer, R. *et al.* Colorectal cancer in inflammatory bowel disease. *Dis. Colon Rectum.* **42**, 343–347 (1999).
6. Kuribara, K. *et al.* Organic transistors with high thermal stability for medical applications. *Nat. Commun.* **3**, 723 (2012).
7. Kim, D.-H. *et al.* Stretchable and foldable silicon integrated circuits. *Science* **320**, 507-511 (2008).
8. Kim, D.-H. *et al.* Epidermal electronics. *Science* **333**, 838-843 (2011).
9. Kaltenbrunner, M. *et al.* An ultra-lightweight design for imperceptible plastic electronics. *Nature* **499**, 458-463 (2013).

10. Sekitani, T., Zschieschang, U., Klauk, H. & Someya, T. Flexible organic transistors and circuits with extreme bending stability. *Nat. Mater.* **9**, 1015-2022 (2010).
11. Kim, K. S. *et al.* Large-scale pattern growth of graphene films for stretchable transparent electrodes. *Nature* **457**, 706-710 (2009).
12. Bae, S. *et al.* Roll-to-roll production of 30-inch graphene films for transparent electrodes. *Nat. Nanotech.* **5**, 574-578 (2010).
13. Kikuchi, S. *et al.* Biological ablation of sentinel lymph node metastasis in submucosally invaded early gastrointestinal cancer. *Mol. Ther.* **20**, 522-532 (2015).
14. Clark, M. E. & Smith, R. R. Liver-directed therapies in metastatic colorectal cancer. *J. Gastrointest. Oncol.* **5**, 374-387 (2014).
15. Daher, R., Choulillard, E. & Panis, Y. New trends in colorectal surgery: single port and natural orifice techniques. *World J. Gastroenterol.* **20**, 18104-18120 (2014).
16. Lee, M.-S. *et al.* High-performance, transparent, and stretchable electrodes using graphene–metal nanowire hybrid structures. *Nano Lett.* **13**, 2814-2821 (2013).
17. Gallagher, F. A. *et al.* Magnetic resonance imaging of pH in vivo using hyperpolarized ^{13}C -labelled bicarbonate. *Nature* **453**, 940-943 (2008).

18. Jana, N. R., Gearheart, L. & Murphy, C. J. Wet chemical synthesis of high aspect ratio cylindrical gold nanorods. *J. Phys. Chem. B.* **105**, 4065-4067 (2001).
19. Kim, D.-H. *et al.* Materials for multifunctional balloon catheters with capabilities in cardiac electrophysiological mapping and ablation therapy. *Nat. Mater.* **10**, 316-323 (2011).
20. Chung, H. J. *et al.* Stretchable, multiplexed pH Sensors with demonstrations on rabbit and human hearts undergoing ischemia. *Adv. health. Mater.* **3**, 59-68 (2014).

Chapter 3. A graphene-based electrochemical device with thermoresponsive microneedles for diabetes monitoring and therapy

3.1 Introduction

High-quality, large area graphene, synthesized by a chemical vapour deposition (CVD) process^{1,2}, constitutes an extremely useful material for emerging transparent and deformable electronics. Graphene exhibits outstanding mechanical³, electrical⁴, and optical properties⁵, by virtue of its soft carbon-based nature⁶, high carrier mobility⁷, and ultrathin form factor. Large-scale processibility^{1,2} and biocompatibility⁸ of graphene further facilitate its numerous consumer and healthcare applications. However, the low defect density of CVD graphene compared to reduced graphene oxides^{9,10} results in poor electrochemical activity. Defect sites have high electrochemical activity and are useful for various electrochemical sensings⁸. Although high-quality CVD graphene has advantages in its large-area

arrayed configurations^{11,12}, it has limitations to be used as electrochemical devices for detection of biochemical markers, such as pH¹³, ions¹⁴, and biomolecules^{15,16}.

Meanwhile, point-of-care continuous monitoring of biomarkers based on electrochemical sensing, together with real-time physical sensing and actuation¹⁷⁻²⁰, provides unique solutions for the treatments of chronic, homeostasis-related diseases, such as diabetes mellitus. There are significant needs for noninvasive monitoring of important markers of such diseases using multifunctional portable/wearable device arrays^{21,22}. A feedback therapeutic system that completes the loop of sensing and therapy²¹ could significantly improve the quality of care management. Here, we report the development of skin-mounted graphene-hybrid (GP-hybrid) device arrays capable of not only the sweat-based glucose and pH monitoring in conjunction with a sweat-control layer but also the controlled transcutaneous drug delivery through bioresorbable temperature-responsive microneedles. Precise measurements of sweat glucose concentrations can be used to estimate levels of glucose in blood based on previously reported correlations²³⁻²⁵. Moreover, integrated sensors for tremor detection under hypoglycaemic conditions and skin temperature monitoring during thermal actuations induced by drug delivery could further help prevent the overdose

of drug and low-temperature burns, respectively. Finally, the connection of graphene-hybrid wearable devices to a portable/wireless power supply and data transmission unit enables point-of-care treatment of diabetes.

*** The contents of this chapter were published in Nature Nanotechnology (2016, 11, 566-572).**

3.2 Experimental Section

Fabrication process of the device array: The device fabrication begins with the spin-coating of the epoxy layer ($\sim 1.5\ \mu\text{m}$; SU8-2, Microchem, USA) on a nickel sacrificial layer ($\sim 50\ \text{nm}$; thermal evaporation) deposited on a silicon handle wafer. After curing of the coated epoxy, the bottom epoxy layer is patterned using photolithography. Thermal evaporation is used to form the Cr/Au ($\sim 7\ \text{nm}/\sim 70\ \text{nm}$) film, which is patterned as the Au mesh interconnects using photolithography and wet etching. The graphene synthesized on a Cu foil (Product #46365, Alfa Aesar, USA) through the CVD process is transferred and patterned. Finally, the device is encapsulated with another epoxy layer. The fabricated device is transfer-printed onto a PDMS substrate (Sylgard 184, Dow Chemical, USA) after the wet etching of the sacrificial nickel layer.

Electrochemical characterization of electrodes: AC impedance, CV, galvanostatic method, amperometric i-t curve, and OCP measurements are performed by using an electrochemical analyzer (CHI660E, CH instrument, USA). Characterization of electrodes and functional materials is carried out using the three-electrode method with the reference electrode (commercial

Ag/AgCl electrode, saturated calomel electrode (SCE), Ag electrode), Pt counter electrode, and fabricated working electrode (designed area is 1 cm² for intrinsic characterization of each electrodes).

Selective functionalization of electrochemical devices: Selective functionalization is carried out through electrodeposition by using the three-electrode method with the reference electrode (commercial Ag/AgCl electrode, saturated calomel electrode (SCE), Ag electrode), Pt counter electrode, and graphene-hybrid electrode as a working electrode. The process is as follows (from i to vi):

- i) Au doping: Prior to the selective functionalization, Au doping on the bilayer electrode of Au mesh and graphene is proceeded by the treatment with 20 mM AuCl₃ (Product #43360, Alfa Aesar, USA) aqueous solution for 5 min. After Au doping, active sites are gently washed with water.
- ii) Ag/AgCl electrodeposition: An aqueous solution of 5 mM AgNO₃ (Product #209139, Sigma-Aldrich, USA) and 1 M KNO₃ (Product #P8394, Alfa Aesar, USA) is prepared. The graphene-hybrid electrode is dipped into the prepared solution. The potential is swept from -0.9 to 0.9 V versus Ag electrode for 20 segments at a scan rate of 0.1 V s⁻¹. For chlorination, the electrode is dipped in an aqueous solution of 0.1 M KCl (Product #P5405,

Sigma-Aldrich, USA) and 0.01 M HCl (Product #H1758, Sigma-Aldrich, USA). The potential is swept from -0.15 to 1.05 V versus SCE for 4 segments at a scan rate of 0.05 V s^{-1} .

iii) PEDOT electrodeposition: A solution of 0.01 M 3,4-ethylenedioxythiophene (Product #483028, Sigma-Aldrich, USA) and 0.1 M LiClO_4 (Product #271004, Sigma-Aldrich, USA) in acetonitrile (Product #271004, Sigma-Aldrich, USA) is prepared. The graphene-hybrid electrode is dipped into the solution and the galvanostatic electrodeposition is performed with 0.5 mA of anodic current (potential vs. commercial Ag/AgCl electrode) for 40 s. PEDOT deposition starts when the potential is higher than 1.2 V.

iv) PANi electrodeposition: An aqueous solution of 0.1 M aniline (Product #242284, Sigma-Aldrich, USA) in 1 M HCl is prepared. The graphene-hybrid electrode is dipped into the solution and the potential is swept from -0.2 to 1 V versus commercial Ag/AgCl electrode for 40 segments at a scan rate of 0.1 V s^{-1} .

v) PB electrodeposition: An aqueous solution of 0.1 M KCl, 5 mM $\text{K}_3[\text{Fe}(\text{CN})_6]$ (Product #P702587, Sigma-Aldrich, USA), and 5 mM FeCl_3 (Product #236489, Sigma-Aldrich, USA) in 0.01 M HCl is prepared. The graphene-hybrid electrode is dipped into the solution and the potential is

swept from -0.2 to 1 V versus SCE for three segments at a scan rate of 0.1 V s⁻¹.

vi) Drop-casting of GOx on glucose sensor and Nafion passivation: A solution of 0.1 M KCl and 0.5 g mL⁻¹ GOx (Product #G7141, Sigma-Aldrich, USA) is prepared in 1X PBS (Dulbecco's phosphate-buffered saline, WELGENE Inc., Republic of Korea). A 2 µL of the solution is drop-casted on PB/ graphene-hybrid twice. After drying the electrodes, Nafion (Product #309389, Sigma-Aldrich, USA) is drop-casted on the humidity sensor (2 µL) and other sensors (10 µL).

Characterization of the humidity sensor: The humidity sensor is calibrated using the AC impedance method. Measurements are performed using the two-electrode method with PEDOT/ graphene-hybrid interdigital electrodes. Relative humidity (RH) is controlled by introducing a mixed stream of dry nitrogen and deionized water vapour into the test chamber. RH is measured using a commercial humidity meter (Center310, Center, Taiwan). The humidity sensor is calibrated between 20 % and 80 % RH at 100 Hz. For real-time monitoring of humidity, the impedance-time measurements are performed at 100 Hz.

Characterization of the glucose sensor: The glucose sensor is characterized under the air condition by using amperometric i-t curves (initial potential: -0.05 V vs. solid-state Ag/AgCl electrode).

i) Calibration and stretching test: The glucose sensor is calibrated in the glucose concentration range between 10 μ M and 0.7 mM. For the stretching test, measurements are performed from 0 to 0.7 mM under 10 %, 20 %, and 30 % applied strains.

ii) Selectivity test: Selectivity of the sensor is tested by the step-wise addition of 0.3 mM glucose (Product #G7141, Sigma-Aldrich, USA), 4 mM lactate (Product #69775, Sigma-Aldrich, USA), 10 μ M ascorbic acid (Product #A7506, Sigma-Aldrich, USA), 59 μ M uric acid (Product #U2625, Sigma-Aldrich, USA), and 0.5 mM glucose in every 60 s.

iii) pH and temperature dependency test: The pH dependency of the glucose sensor is estimated with solutions of 0 to 0.5 mM glucose at different pH values. The temperature dependency of the glucose sensor is estimated at 5, 15, and 25 °C.

iv) Time dependent stability test: Stability of the glucose sensing in artificial sweat (0.3 mM) for 6 hours with a 2 hours interval is estimated under room temperature. For the long-term stability test over several days, the glucose

sensor is tested under room temperature and stored under 4 °C condition while it is not used.

v) Drug interaction test: The effect of drug interactions on the sensitivity of the glucose sensor is estimated in a series of test solutions. Test solutions contain glucose and common drugs: glucose only (control), mixture of glucose and 20 $\mu\text{g mL}^{-1}$ acetaminophen (Tylenol; Product #A7085, Sigma-Aldrich, USA), mixture of glucose and 100 $\mu\text{g mL}^{-1}$ acetylsalicylic acid (Aspirin; Product #A5376, Sigma-Aldrich, USA), and mixture of glucose and 100 $\mu\text{g mL}^{-1}$ Metformin (Product #D150959, Sigma-Aldrich, USA).

Characterization of the pH sensor: pH-dependent changes in the zeta potential of the PANi/ graphene-hybrid are measured using an electrokinetic analyzer (SurPASS, Anton Paar, USA). The pH sensor is characterized under the air condition using real-time OCP measurements with an electrochemical analyzer. The two-electrode method with PANi/graphene-hybrid as the working electrode and the solid-state Ag/AgCl electrode as the counter electrode is used for the measurement. The pH sensor is calibrated using standard buffered pH solutions (buffered solutions pH from 5 to 8, Alfa Aesar, USA). The same measurement procedure is used for the stretching test under 10 %, 20 %, and 30 % applied strains. The effect of temperature

on the pH sensor is also tested by measuring open circuit potential change of pH sensor using the standard buffered pH solutions at 5, 15, and 25 °C.

Characterization of strain gauge, heater, and temperature sensor:

Changes in the resistance of the strain gauge are measured using a digital multimeter (USB-4065, National Instrument, USA). The temperature sensor is also calibrated using the same digital multimeter. The temperature is monitored using the fabricated temperature sensor while the heater is turned on. The temperature sensor data is compared with a commercial infrared camera data (FLIR E8, FLIR, USA).

Wireless control of graphene-hybrid electrochemical devices on the human skin: Graphene-hybrid electrochemical devices are connected to a portable electrochemical analyzer (PalmSens3, Palm instrument B.V., Netherlands) using anisotropic conductive film (HST-9805-210, Elform, USA). The electrochemical analyzer is controlled wirelessly using an Android application (PStouch from the Google Play Store) via Bluetooth. The humidity sensor first monitors relative humidity (RH) changes inside the patch during sweating on the human skin under the warm condition. When RH is over 80 %, glucose and pH sensors start to monitor. It takes ~15

minutes on average, which correspond to the warm-up time. Relative current changes of the glucose sensor are converted into the sweat glucose level according to the calibration curve with pH-based corrections.

Glucose level measurement process using glucose and pH sensors: Every glucose and pH sensor needs a two-step calibration process before their first use to ensure precise monitoring of glucose and pH levels. At first, glucose and pH sensors are calibrated using artificial sweat solutions. For the glucose sensing, we used the amperometric measurement that gives a current (i) versus time (t) curve under constant potential (initial potential: -0.05 V vs. solid-state Ag/AgCl electrode). Relative current changes ($\Delta I/I_0$) are obtained at different glucose concentrations. Then $\Delta I/I_0$ will be converted into the glucose concentration based on the calibration curve. For the pH sensing, measured open circuit potential is converted into the pH value by using the calibration curve. The measured pH value is then used to adjust the glucose concentration. After characterization of glucose and pH sensors *in vitro*, the correlation factor between glucose levels in sweat and blood is obtained by measuring blood and sweat glucose concentrations *in vivo*. In our device array, two glucose sensors are fabricated as a pair and likewise in the pH sensors. Therefore, glucose and pH sensing can be continued, although one

of the paired sensors is in failure. If all paired sensors are not functioning properly, the whole integrated system should be replaced.

Fabrication process of PCM-coated bioresorbable microneedles: The intaglio PDMS mould of microneedles is prepared by using commercial microneedles (PAMAS, Prestige, Republic of Korea) as a master. A microneedle has the base diameter and height of 250 μm and 1 mm, respectively. A liquid mixture of vinyl pyrrolidone (Product #V3409, Sigma-Aldrich, USA), 1 wt% free-radical initiator (azobisisobutyronitrile; Product #A1482, Samchun, Republic of Korea), and 5 wt% Metformin (Product #D150959, Sigma-Aldrich, USA) is casted onto the mould. Then a device array is placed on top and the sample is dried in a vacuum chamber at room temperature. The sample is then radiated with the UV light for 30 min at room temperature using a 40 W UV lamp. After the full crosslinking, microneedles are gently peeled off. Finally, the PCM (tridecanoic acid, Product #T0412, Tokyo Chemical Industry, Japan) is spray-coated on the microneedles. For the replacement of microneedles, a slightly different fabrication process is used. In this process, a polyethylene naphthalate (PEN) film (thickness $\sim 12 \mu\text{m}$; Teonex Q51, Teijin Dupont Film, Japan) is used as a substrate.

***In vivo* animal experiment:** Diabetic (db/db) female mice at the age of 8 to 10 weeks, which exhibit the type II diabetes, are used. Among 30 mice, 18 mice are selected at random without blinding. Drug-loaded microneedles on the heater and temperature sensor are attached on the mouse skin with the gentle pressure. Transcutaneous drug delivery is initiated by the thermal actuation. Changes in the blood glucose concentration are measured using a commercial glucose meter (Accu-chek performa, Roche, Switzerland). The measured blood glucose levels from treated and control (no patch application and patch with drug-unloaded microneedles) groups are analysed using ANOVA with post-hoc method.

***In vitro* and *in vivo* characterization of microneedles:** Temperature-dependent drug release from PCM-coated microneedles is characterized by using HPLC *in vitro*. The drug (Metformin; Product #D150959, Sigma-Aldrich, USA) is eluted in 4.3 min. The microneedles are dissolved by heating under droplets of artificial sweat. Changes in temperature are monitored using both a commercial infrared camera and the fabricated temperature sensor. Therapeutic effect of drug released from microneedles is also tested *in vivo* with the diabetic (db/db) mouse model. Changes of blood

glucose concentrations are monitored using a commercial glucose meter (Accu-chek performa, Roche, Switzerland).

Ethical approval for the animal experiment: All procedures are approved by the Institutional Animal Care and Use Committee (IACUC) of the Biomedical Research Institute of Seoul National University Hospital. All experiments are performed according to IACUC guidelines.

3.3 Result and Discussion

3.3.1 Device design and material strategy for diabetes patch

The integrated system consists of the following components: sweat-control components (sweat-uptake layer and water-proof film), sensing components (humidity, glucose, pH, and tremor sensor), and therapeutic components (microneedles, heater, and temperature sensor), as shown in Figs. 3.1a and b. The bilayer of Au serpentine mesh and gold-doped CVD graphene (Fig. 3.1c bottom) ensures high conductivity, mechanical reliability, and optical transparency for the stable electrical signal transfer as well as the semi-transparent skin look in the large-area deformable device array configuration. Selective, patterned functionalization of gold-doped CVD

graphene with electrochemically active, soft materials (Figs. 3.1a and b left and Fig. 3.1c top) establishes graphene-hybrid sensors with enhanced electrochemical activity and biochemical sensitivity/selectivity, while maintaining graphene's intrinsic softness. In contrast to conventional liquid-type bulky counter electrodes used for electrochemical sensing, solid-state Ag/AgCl counter electrodes (included in sensor components; Figs. 3.1a and b) provide portability and wearability of the electrochemical system. Bioresorbable polymer-based microneedles^{26,27} coated with the phase change material (PCM)²⁸ release drug into the bloodstream when the temperature exceeds the programmed threshold temperature (Fig. 3.1a right and Fig. 3.1b inset). Multichannel thermal actuators (Fig. 3.1b right) control the amount/rate of drug release in a step-wise manner. Soft materials with stretchable designs provide extremely conformal contacts to the human skin under deformations (Fig. 3.1d). This conformal and intimate interfacing enables the stable sensing and efficient drug delivery. If the patch is delaminated, sensing and drug delivery are not effective.

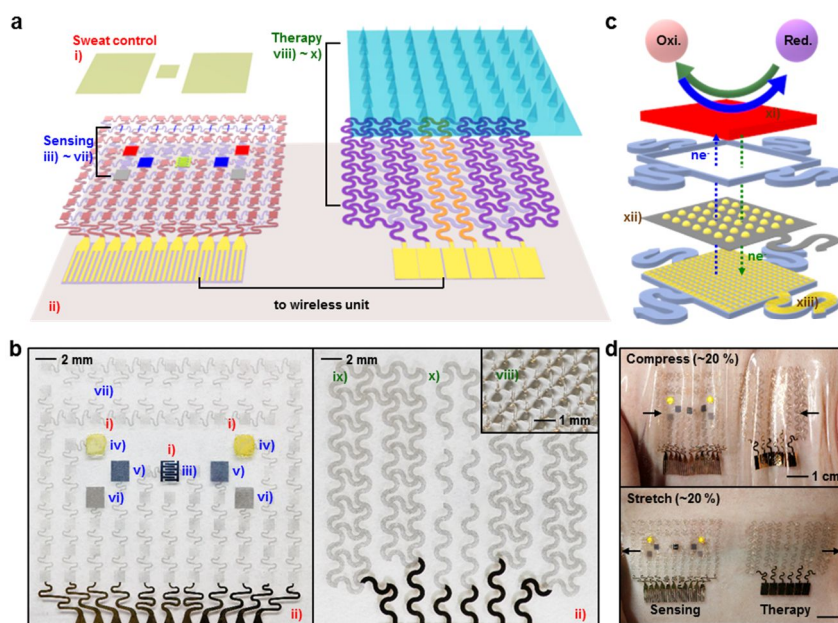


Figure 3.1. Schematic illustrations and corresponding images of graphene-hybrid electrochemical devices and thermo-responsive drug delivery microneedles. **a**, Schematic illustration of the diabetes patch, which is composed of the sweat-control (i, ii), sensing (iii ~ vii), and therapy (viii~x) component. Detailed explanation of (i~x) is in Fig. 1b. **b**, Optical camera image of the electrochemical sensor array (left), therapeutic array (right), and magnified view of the drug-loaded microneedles (inset). The Roman numerals in the figure are same as those in Fig. 1a. The Roman numerals mean each component and its material, *i.e.*, i) sweat-uptake layer (Nafion), ii) water-proof film (silicone), iii) humidity sensor (PEDOT), iv) glucose sensor (PB), v) pH sensor (PANi), vi) counter electrode (Ag/AgCl),

vii) tremor sensor (graphene), viii) microneedles with drugs (PVP@PCM), ix) heater (Au mesh/graphene), and x) temperature sensor (graphene). **c**, Schematic illustration of the graphene-hybrid electrochemical unit, which consists of electrochemically active and soft functional materials (xi), gold-doped graphene (xii), and serpentine Au mesh (xiii), from top to bottom. **d**, Optical camera images of the diabetes patch laminated on the human skin under mechanical deformations.

3.3.2 Characterization of graphene-hybrid

The electrochemical properties of the graphene-hybrid are characterized and compared to controls (Au film and Au mesh). Optical (left) and scanning electron microscope (SEM; right) images of individual electrodes with the poly(3,4-ethylenedioxythiophene) (PEDOT) functionalization by the galvanostatic electrodeposition are shown in Fig. 3.2a. The amount of functional materials deposited on the Au mesh (Fig. 3.2a, middle) is much less than that on the Au film (Fig. 3.2a, top) or graphene-hybrid (Fig. 3.2a, bottom) electrode because of the non-conducting square regions of the mesh. Au particles on doped graphene form scattered clusters of functional materials on the graphene-hybrid surface. The graphene-hybrid, therefore, exhibits better electrochemical performance characteristics due to its large electrochemically active surface area under bare electrode conditions (Figs. 3.2b–d) as well as during (Figs. 3.2e–g) and after (Figs. 3.2h–j) the functionalization.

Cyclic voltammograms (CV; Fig. 3.2b and Fig. 3.3a) and alternative current (AC) impedance measurements (Nyquist plots in Fig. 3.2c and Fig. 3.3b, Bode plots in Fig. 3.2d) for $\text{Fe}(\text{CN})_6^{3-/4-}$ redox couple demonstrate the higher charge storage capacity (CSC) and lower interfacial

impedance of the electrode of the graphene-hybrid than controls. Au mesh shows the highest charge transfer resistance (R_{ct}) and its CV peak shifts to higher potentials, due to the small active area and low electrochemical activity. The electrode of the graphene-hybrid, bilayer of gold-doped CVD graphene and Au mesh, however, compensates non-conducting regions of the Au mesh by doped graphene, which enlarges the electrochemically active surface area, slightly larger than that of Au film. The electrochemical stability/reliability of the graphene-hybrid electrode is further proven through temperature-dependent impedance measurements and multiple CV operations (Figs. 3.3c and d). This large electrochemically active surface area of the graphene-hybrid electrode is consistent with the nanostructured topography in visual observations (optical and SEM images), which corroborates its superb characteristics. In contrast, electrochemical characterization of undoped CVD graphene shows negligible redox reactions and high impedances due to its low electrochemical activity (Figs. 3.4a–c).

These electrochemical properties of the graphene-hybrid electrode are further highlighted through functionalization, which is supported by enhanced electrochemical activities during and after the electrodeposition of functional materials. Figures 3.2e–g show larger electrical current amplitudes and sharper characteristic peaks of the graphene-hybrid during

the controlled electrodeposition process of PEDOT, Prussian Blue (PB), and polyaniline (PANi). The electrode of the graphene-hybrid exhibits excellent electrochemical interactions with each monomer. The resulting graphene-hybrid film shows better electrochemical performances, including lower interfacial impedance of the PEDOT/graphene-hybrid (Fig. 3.2h and Fig. 3.5a) and more prominent characteristic redox peaks of the PB/graphene-hybrid (Fig. 3.2i and Fig. 3.5b), than others. However, the pH-dependent open circuit potential (OCP) of the PANi/graphene-hybrid shows comparable trends to that of the Au film and Au mesh (Fig. 3.2j and Fig. 3.5c). The graphene-hybrid clearly improves impedance-based (PEDOT) and charge-transfer-based (PB) electrochemical activities, for which reactions occur on the surface. However, the OCP depends on bulk properties of the PANi rather than surface properties and thereby similar results are observed.

High conductivity and mechanical robustness are important for efficient charge/signal injection into and extraction from electrochemical cells. Mechanical robustness under various deformations is another important requirement of skin-based wearable systems^{29,30}. In addition to the intrinsic softness of graphene (Fig. 3.6a; arrows show the typical fracture strain of each material^{3,31,32}), electrodes that use serpentine designs significantly enhance mechanical deformability (Fig. 3.6b left). To prevent

mechanical fractures in the Au mesh, we used serpentine designs^{33,34}. The neutral mechanical plane^{29,30} and ultrathin design³⁵⁻³⁷ further increase tolerance to mechanical deformations. These materials and design strategies minimize the induced strain occurring during deformations. These experimental results are confirmed with finite element modeling (FEM) analysis (Fig. 3.6b right). In our design, the serpentine-shaped Au mesh subjacent to gold-doped CVD graphene enhances electrical conductivity in comparison with conventional transparent electrodes, while minimizing mechanical fractures during a cyclic stretching test (Fig. 3.6c and its inset). An additional important advantage of the graphene-hybrid is in the optical transparency, providing the natural skin look of the diabetes patch (Fig. 3.7).

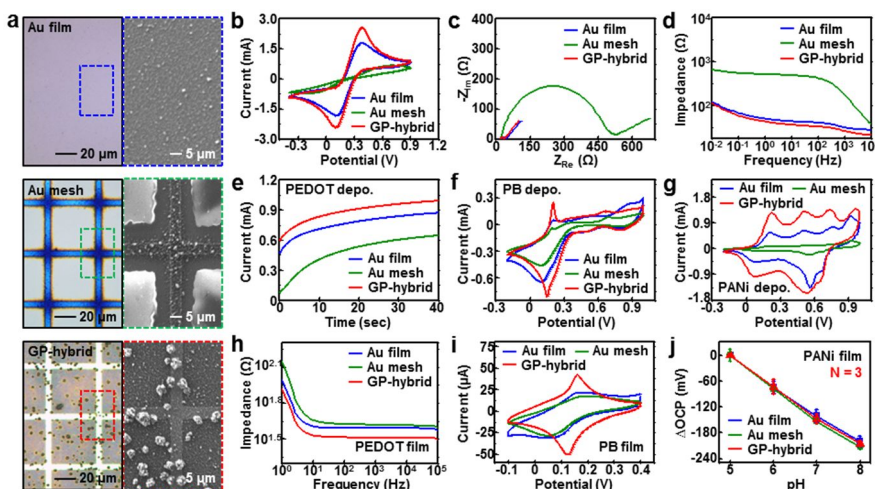


Figure 3.2. Electrochemical and electrical characterization of the graphene-hybrid. **a**, Optical (left) and SEM (right) images of the Au film (top), Au mesh (middle), and graphene-hybrid (bottom) after the PEDOT electrodeposition. **b**, CV plots of the Au film, Au mesh, and graphene-hybrid electrode in PBS with $\text{Fe}(\text{CN})_6^{3-/4-}$ (scan rate: 0.1 V s^{-1} with the commercial Ag/AgCl electrode). **c**, Nyquist plots of the Au film, Au mesh, and graphene-hybrid electrodes in PBS with $\text{Fe}(\text{CN})_6^{3-/4-}$ at the equilibrium potential. **d**, Bode plots of the Au film, Au mesh, and graphene-hybrid electrodes in PBS with $\text{Fe}(\text{CN})_6^{3-/4-}$ at the equilibrium potential. **e**, Amperometric curves of the Au film, Au mesh, and graphene-hybrid electrodes during the PEDOT electrodeposition process (initial potential: 1.25 V vs. commercial Ag/AgCl electrode). **f**, CV plots of the Au film, Au mesh, and graphene-hybrid electrodes during the PB electrodeposition process (scan rate: 0.1 V s^{-1} with

the commercial saturated calomel electrode). **g**, CV plots of the Au film, Au mesh, and graphene-hybrid electrodes during the PANi electrodeposition process (scan rate: 0.1 V s^{-1} with the commercial Ag/AgCl electrode). **h**, Bode plots of the Au film, Au mesh, and graphene-hybrid electrodes in PBS after electrodeposition of PEDOT. **i**, CV plots of the Au film, Au mesh, and graphene-hybrid electrodes in PBS after electrodeposition of PB (scan rate: 0.1 V s^{-1} with the commercial Ag/AgCl electrode). **j**, pH-dependent OCP changes in the Au film, Au mesh, and graphene-hybrid electrodes after electrodeposition of PANi (number of samples = 3, error bars show the standard deviation, OCP vs. commercial Ag/AgCl electrode).

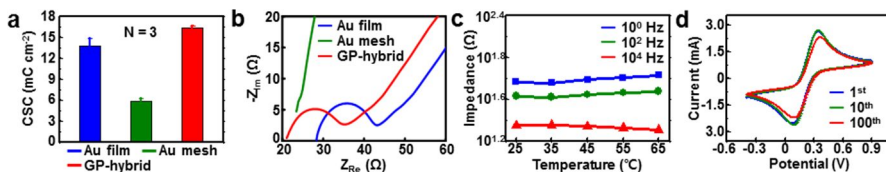


Figure 3.3. Electrochemical characterization of graphene-hybrid. **a**, Charge storage capacities of the Au film, Au mesh, and graphene-hybrid electrodes in Fig. 3.2b (number of samples = 3, error bars show the standard deviation). **b**, Magnified view of Nyquist plots of Au film, Au mesh, and graphene-hybrid electrode in PBS with $\text{Fe}(\text{CN})_6^{3-/4-}$ at equilibrium potential. **c**, Electrical stability test of graphene-hybrid electrode at different temperatures and AC frequencies in PBS with $\text{Fe}(\text{CN})_6^{3-/4-}$ at equilibrium potential. **d**, Stability test of graphene-hybrid electrode after multiple CV measurements in PBS with $\text{Fe}(\text{CN})_6^{3-/4-}$ (scan rate: 0.1 V s^{-1} with the commercial Ag/AgCl electrode).

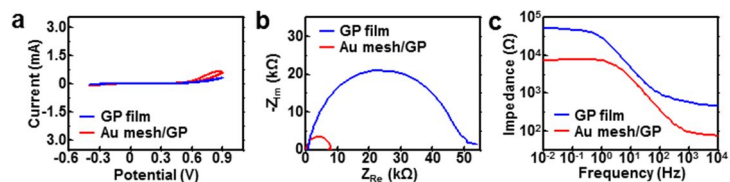


Figure 3.4. Electrochemical properties of graphene film and Au mesh/graphene. **a**, CV plots of the graphene film and the Au mesh/graphene in PBS with $\text{Fe}(\text{CN})_6^{3-/4-}$ (scan rate: 0.1 V s^{-1} with the commercial Ag/AgCl electrode). **b**, Nyquist plots of the graphene film and Au mesh/graphene in PBS with $\text{Fe}(\text{CN})_6^{3-/4-}$ at the same potential with that of Fig. 3.2c. **c**, Bode plots of graphene film and Au mesh/graphene in PBS with $\text{Fe}(\text{CN})_6^{3-/4-}$ at the same potential with that of Fig. 3.2d.

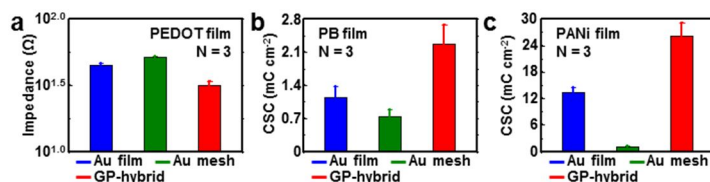


Figure 3.5. Reproducibility of electrochemical characterization of electrodes (Au film, Au mesh, and graphene-hybrid electrode) after functionalization. **a**, Impedances of the Au film, Au mesh, and graphene-hybrid electrodes at 100 Hz after electrodeposition of PEDOT under the same condition used in Fig. 3.2e (number of samples = 3, error bars show the standard deviation). **b**, Charge storage capacities of the Au film, Au mesh, and graphene-hybrid electrodes after electrodeposition of PB under the same condition used in Fig. 3.2f (number of samples = 3, error bars show the standard deviation). **c**, Charge storage capacities of the Au film, Au mesh, and graphene-hybrid electrodes after electrodeposition of PANi under the same condition used in Fig. 3.2g (number of samples = 3, error bars show the standard deviation).

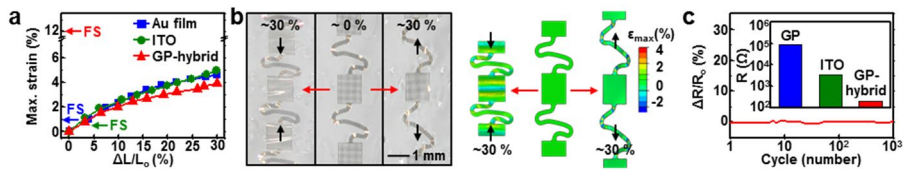


Figure 3.6. Mechanical characterization of the graphene-hybrid. **a**, Comparison of the maximum induced strain in the rectangular island of the graphene-hybrid electrode under the 0~30 % stretching with that of other electrodes (Au film and Indium Tin Oxide (ITO)). Arrows show the fracture strain (FS) of each electrode material. **b**, Optical images (left) and corresponding finite element modeling (FEM) strain distribution analysis results (right) of the graphene-hybrid interconnection under compressed (left red arrow, ~30 % compressed), undeformed, and stretched (right red arrow, ~30 % stretched) states. **c**, Relative resistance changes of the graphene-hybrid electrode after the multiple cyclic stretching test. The inset compares the resistance of the graphene-hybrid electrode with that of other transparent electrodes (graphene and ITO).

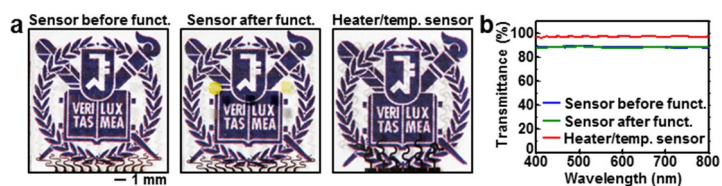


Figure 3.7. Transparency of the array of graphene-hybrid electrochemical sensors and the heater/temperature sensor. a, Optical camera images of the sensor array before (left) and after (center) functionalization on the university logo. Right frame shows the heater/temperature sensor array on the university logo. The logo can be clearly seen through devices due to the transparency. **b,** Corresponding transmittance data of each sample.

3.3.3 Characterization of diabetes patch *in vitro*

After the fabrication of the interconnected array layout on a handle substrate, the device is transfer-printed onto a thin silicone patch, followed by the selective, patterned electrochemical functionalization for graphene-hybrid sensors (Fig. 3.8). The step-wise selective electrodeposition of each functional material prevents cross-contamination (Fig. 3.9). The heater, tremor sensor (strain gauge), and temperature sensor are fabricated by the resistance modulation of graphene and Au mesh (Fig. 3.1b).

The sensors for humidity, glucose/pH, and tremor (strain gauge) and the heater/temperature sensor are described in Figs. 3.10-15. The humidity sensor monitors relative humidity (RH) changes based on impedance changes of interdigitated PEDOT electrodes to make sure enough amount of sweat is present on the skin (Fig. 3.10a). The glucose and pH sensors measure electrochemical signal changes of the PB/graphene-hybrid by the reduction of H_2O_2 generated from the glucose oxidase and those of the PANi/graphene-hybrid by pH changes, respectively, in conjunction with the solid-state Ag/AgCl counter electrode (Fig. 3.10b). The glucose sensor is calibrated before its first use and tested in the glucose concentration range between 10 μM and 0.7 mM (Fig. 3.10b middle and Fig. 3.11a-c). These

glucose concentrations correspond to typical sweat glucose concentrations of hypoglycaemic and hyperglycaemic patients as well as normal people²³⁻²⁵. The glucose sensor is found to be stable under mechanical deformations and maintains its sensitivity under various motions (Fig. 3.11b). The glucose sensor reacts specifically to glucose in the presence of other biomolecules contained in the sweat (*e.g.*, lactate, ascorbic acid, and uric acid; Fig. 3.11d,e). The glucose oxidase in the current device setting is active at least for a day under ambient conditions and for several days depending on storage conditions (see Fig. 3.11f). The low operation potential (initial potential: -0.05 V vs. solid-state Ag/AgCl electrode) of the glucose sensor prevents electrochemical interferences.

The pH sensor is calibrated with step-wise pH changes using standard pH buffer solutions and is stably operated under deformations (Fig. 3.10b bottom and Figs. 3.12a and b). The pH sensor is used to correct the pH-dependent deviation of the enzyme-based glucose sensor. The glucose oxidase (GOx) is affected by pH changes in the sweat. The sweat pH is typically lower than the neutral condition (*i.e.*, pH = 7) due to the metabolic lactic acid secretion during muscle movements (Fig. 3.12c) and varies among human subjects. The time dependent stability of the glucose sensor is also estimated. The tremor sensor (strain gauge) is calibrated and

successfully measures cyclic strain changes (Fig. 3.10c). The heater and temperature sensor are calibrated (Fig. 3.10d) and used in the drug delivery process.

The combined operation of these sensors using the artificial sweat *in vitro* is shown in Fig. 3.13a,b. First, the humidity sensor monitors RH and determines the starting point for glucose and pH sensing, which are stabilized at RH of > 80 % (Fig. 3.13a). The diabetes patch needs at least 20 μL of human sweat for measurement of the glucose concentration. No disturbance is found in larger volume of the sweat (Figs. 3.14a and b). The glucose and pH sensors measure glucose and pH changes in real-time. Simulated hyperglycaemia (0.3 mM sweat glucose level corresponding to 300 mg dL^{-1} blood glucose level)²³ is then successfully detected, as shown in Fig. 3.13b. Hyperglycaemia is defined when blood glucose level is above 126 mg dL^{-1} under fasting³⁸. However, due to continuous pH changes (blue), the efficiency of GOx and thereby the sensitivity of the glucose sensor is susceptible to error. Therefore, glucose monitoring with the real-time correction using *in situ* pH measurements (red) agrees much better with the real glucose concentration of the artificial sweat (dotted line, 0.3 mM) than the uncorrected one (green). The temperature dependency of glucose and pH sensors are estimated. The sensitivity of the glucose sensor is slightly

decreased as the temperature decreases, while the sensitivity of the pH sensor is similar at various temperatures (Figs. 3.15a and b). Our diabetes patch, therefore, provides more reliable sensing performances than previous devices due to systematic correction of sweat glucose measurements based on pH and temperature monitoring. Potential interactions of the glucose sensor with common drugs (Aspirin, Tylenol, and Metformin) are also estimated. Their influences on glucose sensing are minimal (Fig. 3.15c). The wearable tremor sensor detects simulated tremors possibly induced in hypoglycaemic states, where physiological tremors occur with frequency over 1 Hz (Fig. 3.13c)³⁹. After comparison with pre-programmed thresholds of the acceptable glucose concentration that is determined by a family doctor, the real-time glucose monitoring data can trigger the heater embedded in the patch to thermally activate the drug-loaded microneedles. The turned-off heater maintains microneedles coated with the PCM inactive.

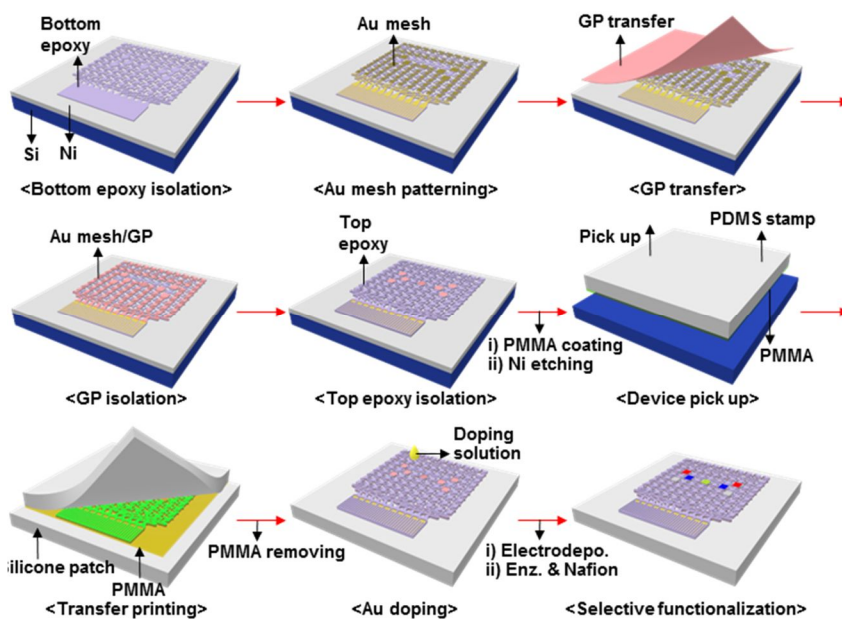


Figure 3.8. Device fabrication process. Schematic illustration of the fabrication process of the graphene-hybrid electrochemical sensor array.

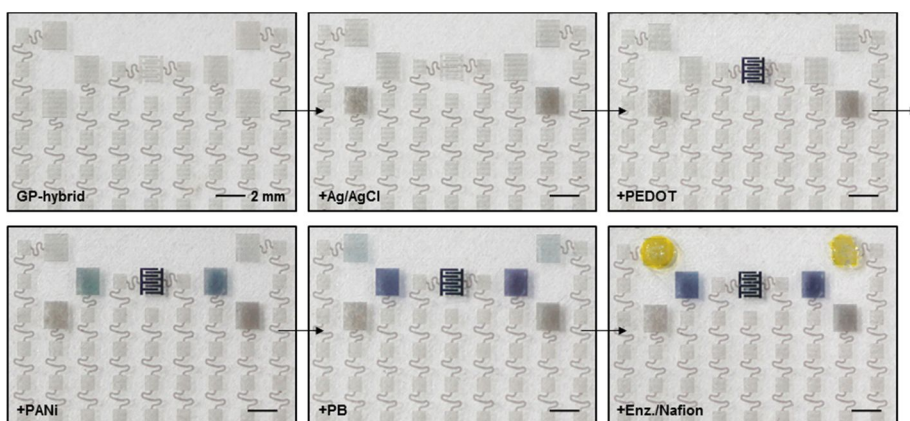


Figure 3.9. Selective functionalization process of the graphene-hybrid sensors and Ag/AgCl solid-state counter electrode. Optical camera images of the step-wise selective functionalization process of graphene-hybrid. No cross-contaminations are observed.

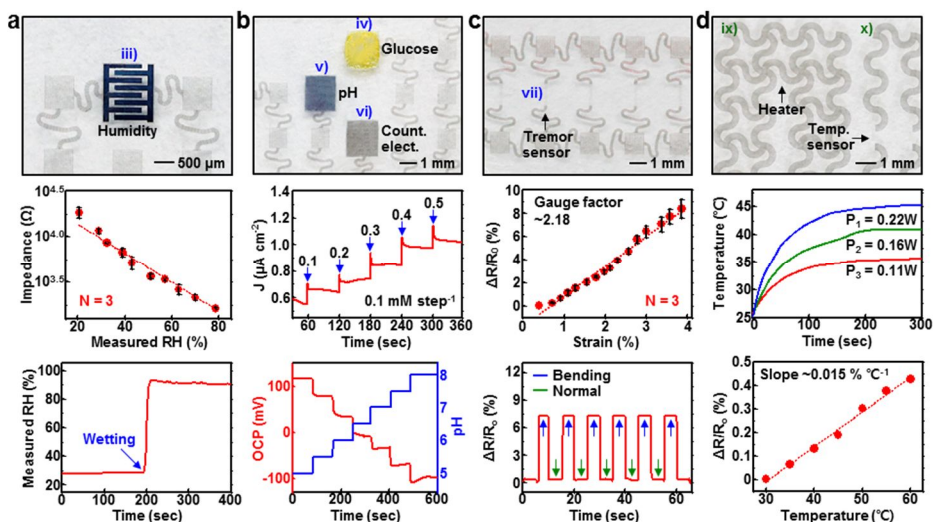


Figure 3.10. Electrochemical and electrical characterization of individual devices. **a**, Optical image (top) and calibration curve (middle; number of samples = 3, error bars show the standard deviation) of the humidity sensor. The bottom frame shows the measurement of impedance changes under wetting. **b**, Optical image (top) and calibration curve of the glucose (middle; blue arrows indicate glucose concentrations in each step) and pH (bottom; OCP vs. solid-state Ag/AgCl electrode) sensor. **c**, Optical image (top) and calibration curve (middle; number of samples = 3, error bars show the standard deviation) of the tremor sensor (strain gauge). The bottom frame shows the measurement of strain changes during repetitive bending deformations. **d**, Optical image (top) and characterization curves of the heater (middle; output temperature profiles at different power values ($P_1 \sim P_3$)) and temperature sensor (bottom; the slope indicates sensitivity of the

temperature sensor).

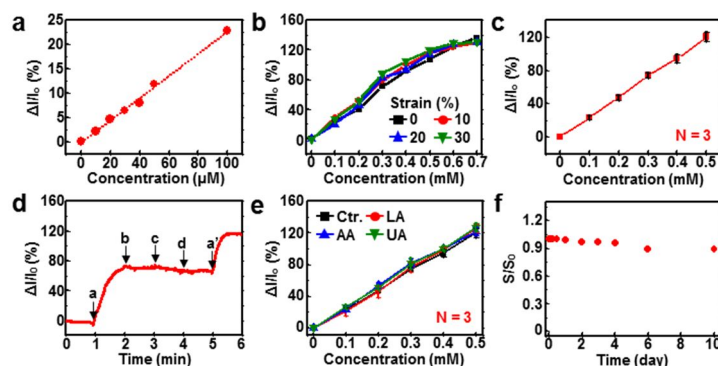


Figure 3.11. Characterization of glucose sensor. **a**, Calibration curves of the glucose sensor at low glucose concentrations (initial potential: -0.05 V vs. solid-state Ag/AgCl electrode). **b**, Calibration curves of the glucose sensor at different applied strains (initial potential: -0.05 V vs. solid-state Ag/AgCl electrode). **c**, Reproducible operation of the glucose sensor (number of samples = 3, error bars show the standard deviation, initial potential: -0.05 V vs. solid-state Ag/AgCl electrode). **d**, Selectivity of the glucose sensor (a: 0.3 mM glucose, b: 4 mM lactate, c: 10 μM ascorbic acid, d: 59 μM uric acid, a': 0.5 mM glucose, initial potential: -0.05 V vs. solid-state Ag/AgCl electrode). Glucose sensor responds to glucose concentration changes only. **e**, Selective operation of the glucose sensor (black: glucose only, red: glucose with 4 mM lactate, blue: glucose with 10 μM ascorbic acid, green: glucose with 59 μM uric acid, number of samples = 3, error bars show the standard deviation, initial potential: -0.05 V vs. solid-state Ag/AgCl electrode). **f**, Long-term stability of the glucose sensor (initial potential: -0.05 V vs. solid-

state Ag/AgCl electrode).

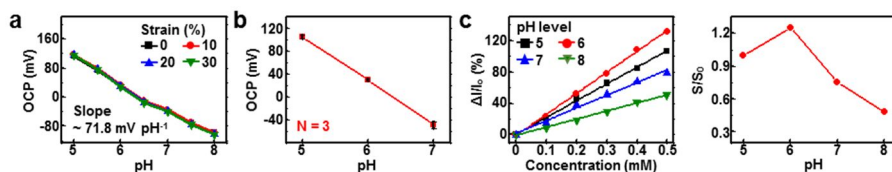


Figure 3.12. Characterization of pH sensor and pH dependency of glucose sensor. **a**, pH-dependent OCP changes of the pH sensor at different applied strains (OCP vs. solid-state Ag/AgCl electrode). **b**, Reproducible operation of the pH sensor (number of samples = 3, error bars show the standard deviation, OCP vs. solid-state Ag/AgCl electrode). **c**, pH dependency of the glucose sensor (left: relative current changes of the glucose sensor at different pH, right: relative sensitivity changes of glucose sensor at different pH, initial potential: -0.05 V vs. solid-state Ag/AgCl electrode).

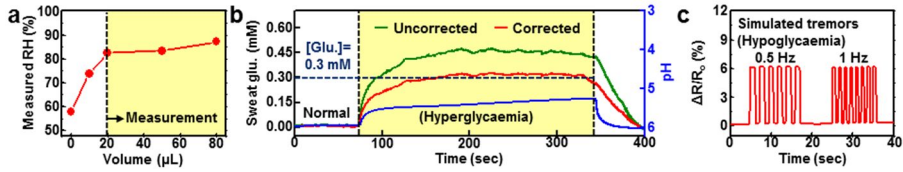


Figure 3.13. Combined operation of individual devices *in vitro*. **a**, Measurement of humidity changes with the application of different volumes of the artificial sweat. When measured RH is over 80 % (yellow region), sensors operate reliably. **b**, Monitoring of glucose (initial potential: -0.05 V vs. solid-state Ag/AgCl electrode) and pH (OCP vs. solid-state Ag/AgCl electrode) changes *in vitro* under the hyperglycaemia in artificial sweat (0.3 mM sweat glucose level corresponding to 300 mg dL⁻¹ blood glucose level). **c**, Tremor sensor in the patch detects tremors similar to those experienced by hypoglycaemic patients. Under hypoglycaemic condition, physiological tremors occur with frequency over 1 Hz.

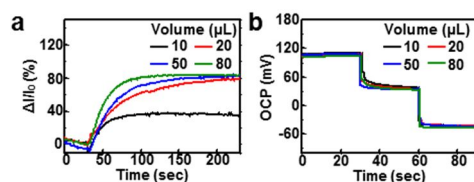


Figure 3.14. Influence of sweat amount test on glucose and pH sensors. a, Influence of sweat amount (or relative humidity) on the glucose sensor (initial potential: -0.05 V vs. solid-state Ag/AgCl electrode). **b,** Influence of sweat amount (or relative humidity) on the pH sensor (OCP vs. commercial Ag/AgCl electrode).

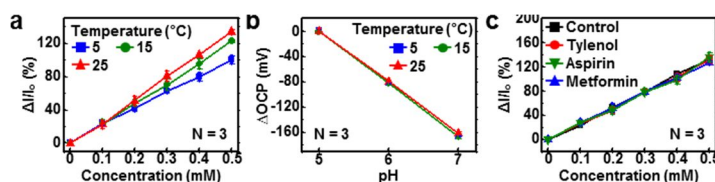


Figure 3.15. Temperature dependency of glucose/pH sensors and drug interaction test of the glucose sensor. **a**, Calibration curves of the glucose sensor at different temperatures (number of samples = 3, error bars show the standard deviation, initial potential: -0.05 V vs. solid-state Ag/AgCl electrode). **b**, Open circuit potential changes of the pH sensor at different temperatures (number of samples = 3, error bars show the standard deviation, OCP vs. commercial Ag/AgCl electrode). **c**, Calibration curves of the glucose sensor in a series of test solutions (black: glucose only, red: glucose with 20 $\mu\text{g mL}^{-1}$ Tylenol, green: glucose with 100 $\mu\text{g mL}^{-1}$ Aspirin, blue: glucose with 100 $\mu\text{g mL}^{-1}$ Metformin, number of samples = 3, error bars show the standard deviation, initial potential: -0.05 V vs. solid-state Ag/AgCl electrode).

3.3.4 Demonstration of sweat-based monitoring and therapy *in vivo*

Human sweat monitoring demonstrations of the wearable diabetes patch *in vivo* are described in Fig. 3.16. The diabetes patch is laminated on the human skin and is electrically coupled to a portable electrochemical analyzer (Fig. 3.17), which in turn, wirelessly transfers data to remote mobile devices (*e.g.*, smartphone or tablet computer) and supplies power to the patch (Fig. 3.16a). Sweat-based glucose monitoring operation begins upon sweat generation (Fig. 3.16b and Fig. 3.18a). The humidity sensor monitors the increase in RH. It takes ~15 minutes on average (10~20 minutes) to collect sweat by the sweat-uptake layer of the patch and thereby to reach the RH over 80% for measurements. The glucose and pH measurements are initiated after the RH reaches over 80 % (Fig. 3.16c).

Two healthy volunteers (both men in twenties), with no medical history of heart problems or diabetes, participate in the study. All subjects are informed of risks and benefits and provided informed consent. The pH of the human sweat is different among subjects as well as subject's conditions (Fig. 3.16d). The pH sensor monitors these changes/differences and corrects the pH-dependent glucose measurements *in situ*. Daily basis glucose

monitoring data *in vivo* are presented in Fig. 3.16e. Sweat glucose concentrations measured by the diabetes patch (red hollow dot) and a commercial glucose assay (red solid dot; Glucose assay kit, Cayman chemical, USA) are well-matched. In addition, changes of the sweat glucose concentration (red, left y axis) are well-correlated with those of the blood glucose concentration (blue, right y axis) (correlation factor: ~ 0.017 ; ratio of the sweat glucose concentration to the blood glucose concentration). Blood glucose concentrations are measured by the commercial glucose meter (Accu-chek performa, Roche, Switzerland). Statistical analysis confirms the reliable correlation between sweat glucose data from the diabetes patch and those from the commercial glucose assay ($P < 0.001$, $R^2 = 0.89$) (Fig. 3.18b) as well as the correlation between sweat glucose data from the diabetes patch and blood glucose data from the commercial glucose meter ($P < 0.001$, $R^2 = 0.83$) (Fig. 3.18c). The pH correction effect on the glucose monitoring is shown in Fig. 3.16f. Corrections using the measured pH (red) provide more accurate glucose monitoring data than those without corrections (orange) compared with the real glucose concentration measured by the glucose assay (green). Another practical advantage of the diabetes patch is that sensitivities of glucose and pH sensors are barely affected after multiple lamination/delamination processes for reuses (Fig. 3.16g and Figs. 3.18d and

e). The glucose and pH sensors also show similar sensitivities in multiple sensors (Fig. 3.18f).

Microneedle-based therapeutic demonstrations of the wearable diabetes patch *in vivo* are described in Fig. 3.19. Detection of hyperglycaemia triggers the thermal actuation of the drug-loaded microneedles. Details of the micro-needle fabrication process are provided in Fig. 3.20. A large-scale view of the fabricated microneedles is presented in Fig. 3.21a. Microneedles are composed of a bioresorbable polymer (polyvinyl pyrrolidone (PVP)^{23,24}) in combination with a pharmacological agent (Metformin⁴⁰; Product #D150959, Sigma-Aldrich, USA). A thermally active bioresorbable coating layer of PCM (tridecanoic acid; Product #T0412, Tokyo Chemical Industry, Japan)²⁵ further protects the PVP/drug from moistures and/or biofluids below the transition temperature ($T_c = 41\text{--}42\text{ }^\circ\text{C}$), as shown in Fig. 3.19a. Thermal actuation above T_c melts the PCM and releases drug into the bloodstream. Analysis using high performance liquid chromatograph (HPLC; Ultimate 3000, Dionex, USA) shows the elution of drug at elevated temperatures ($> 41\text{ }^\circ\text{C}$; Fig. 3.19b and Fig. 3.21b). The integrated temperature sensor monitors temperature changes on the skin and prevents any overheating (Fig. 3.21c). The patterned heating triggers drug release in a step-wise manner (two step release in Figs. 3.19c and d, and four

step release in Figs. 3.21d and e). By increasing the total area of microneedles, the maximum number and/or amount of the drug delivery can be increased.

Therapeutic effects are tested through *in vivo* using 8 to 10-week-old diabetic (db/db) mice (Fig. 3.22) based on a genetically-driven diabetic animal model. Treatment begins by laminating the patch on the skin near the abdomen of the db/db mouse (Fig. 3.19e). The microneedles penetrate through the mouse skin surface, reaching the subcutaneous region, as shown in optical images (Fig. 3.19f). Once the db/db mouse is treated with thermally-actuated microneedles (optical and infrared camera image in Fig. 3.19g), the drug (Metformin) is released into the bloodstream. The experimental group treated with microneedles shows significant suppression of blood glucose concentration with respect to the control groups (Fig. 3.19h; $P < 0.05$, ANOVA with post-hoc analysis). One can easily replace the used microneedles into a new one (Figs. 3.23a and b). The drug-loading capacity of microneedles can be further increased by utilizing its backing layer⁴¹⁻⁴³ (Fig. 3.23c). Treatment of Metformin through the skin is much more efficient than that through the digestive system⁴⁴ because the drug reaches directly to its metabolic circulation through the skin⁴⁵. More studies in the transdermal drug delivery for human patients are needed in the future. The

Metformin is effective not only to diabetes patients for the treatment purpose, but also to people with potential risks of the diabetes for the preventive purpose⁴⁶, which maximizes the utility of the current diabetes patch.

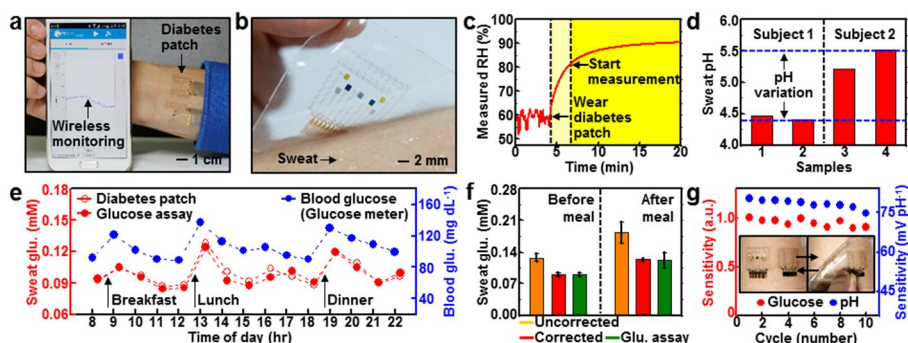


Figure 3.16. Demonstration of the wearable diabetes monitoring *in vivo*.

a, Optical image of the integrated wearable diabetes monitoring and therapy system connected to a portable electrochemical analyser. **b**, Optical image of the graphene-hybrid electrochemical device array on the human skin with perspiration. **c**, Relative humidity measurement by the diabetes patch (white region: before wearing the patch, light yellow region: after wearing the patch, yellow region: starting point of the measurement of glucose and pH levels). **d**, Measurement of the pH variation in two human sweat samples from two subjects. **e**, One-day monitoring of glucose concentrations in the human (subject 2 in Fig. 3.16d) sweat and blood (red hollow dot: sweat glucose concentration by the diabetes patch, red solid dot: sweat glucose concentration by the commercial glucose assay, blue solid dot: blood glucose concentration by the commercial glucose meter). **f**, Comparison of average glucose concentrations with commercial glucose assay data in Fig. 3.16e before and after the correction using the measured pH (error bars show the

standard deviation). **g**, Plots showing the stable sensitivity of glucose and pH sensors after the multiple reuse.

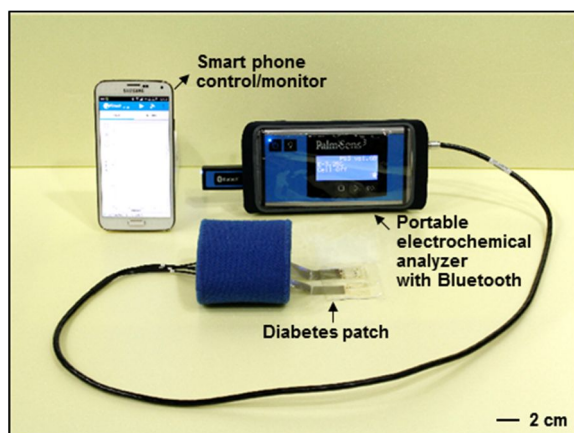


Figure 3.17. Portable electrochemical analyzer. Graphene-hybrid electrochemical devices are connected to the portable electrochemical analyzer that supplies power to and controls the devices and wirelessly transfers data to remote mobile devices (such as smart phone or tablet computer) via Bluetooth.

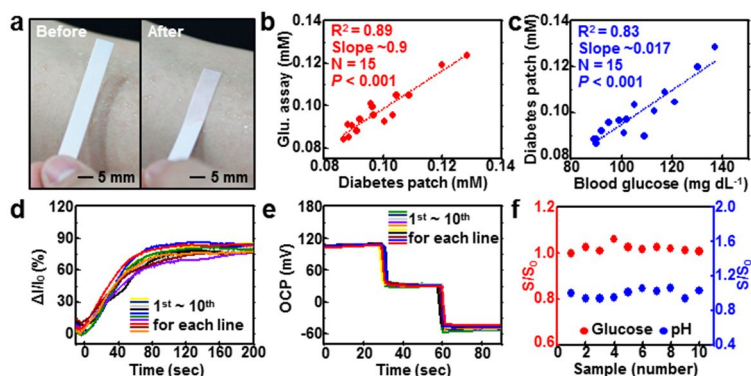


Figure 3.18. Sweat generation, statistical correlation, and multiple reuses. **a**, Optical camera images of the generated sweat, checked by the cobalt chloride paper. **b**, Statistical analysis of the correlation between the sweat glucose concentration measured by the diabetes patch and that measured by the commercial glucose assay. Small P value shows that the results are statistically reliable ($P < 0.001$). **c**, Statistical analysis of the correlation between the sweat glucose concentration measured by the diabetes patch and the blood glucose concentration measured by the commercial glucose meter. Small P value shows that the results are statistically reliable ($P < 0.001$). **d**, Stable operation of the glucose sensor after multiple reuses (initial potential: -0.05 V vs. solid-state Ag/AgCl electrode) using the artificial sweat (0.3 mM). **e**, Stable operation of the pH sensor after multiple reuses (OCP vs. solid-state Ag/AgCl electrode) using standard pH buffer solutions (pH 5, 6, 7). **f**, Plots showing the stable sensitivity of glucose and pH sensor in multiple sensors.

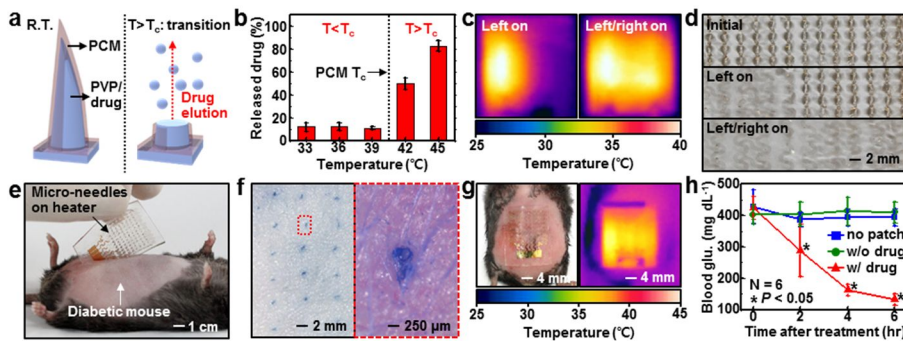


Figure 3.19. Demonstration of the wearable therapy system *in vivo*. **a**, Schematic illustrations of bioresorbable microneedles (PCM; phase change material, PVP; polyvinyl pyrrolidone, drug; Metformin, T_c ; critical temperature indicating the melting point of PCM). **b**, Drug release from microneedles at different temperatures ($n = 3$, error bars show the standard deviation). **c**, Infrared camera images of multichannel heaters showing the step-wise drug release (left on; left channel of the heater is turned on, left/right on; both channels of the heater are turned on). **d**, Optical images of the step-wise dissolution of microneedles (left on; left channel of the heater is turned on, left/right on; both channels of the heater are turned on). **e**, Optical image of the heater integrated with microneedles, which is laminated on the skin near the abdomen of the db/db mouse. Hair on the skin was shaved before the treatment with microneedles. **f**, Optical image (left) and its magnified view (right) of db/db mouse skin stained with the trypan blue to visualize micro-size holes made by penetration of microneedles. **g**, Optical

(left) and infrared (right) camera images of the patch with the thermal actuation. **h**, Blood glucose concentrations of db/db mice: treated group (n = 6; red: patch with drug-loaded microneedles), control groups (n = 6 for each; blue: no patch application, green: patch with drug-unloaded microneedles). Error bars show the standard deviation in each group and small P value shows that the results are statistically reliable.

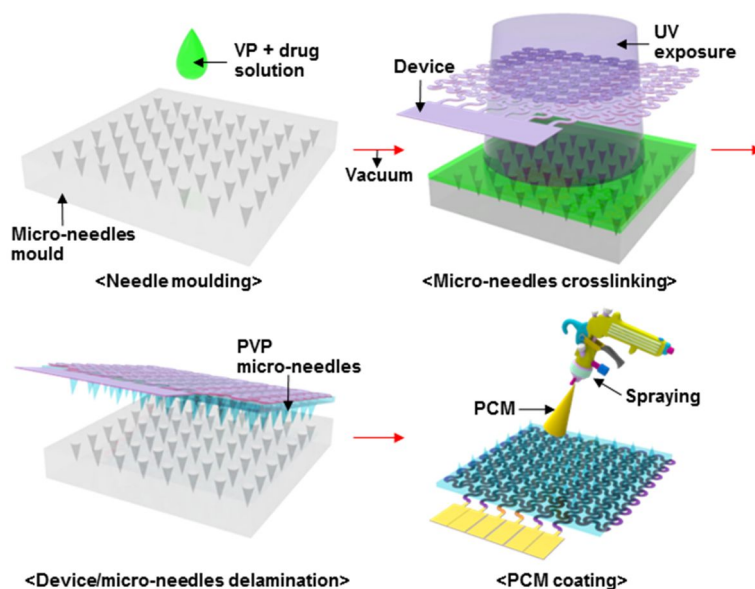


Figure 3.20. Fabrication process of the drug-loaded microneedles.

Schematic illustrations of the fabrication process of the drug-loaded microneedles. Microneedles are made of the bioresorbable polymer (PVP) and coated with the biocompatible PCM (tridecanoic acid).

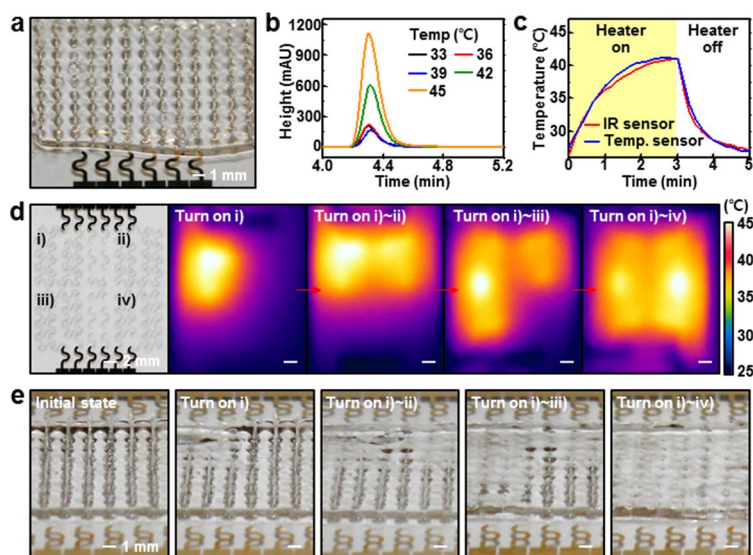


Figure 3.21. Characterization of microneedles, embedded heaters, and a temperature sensor. **a**, Optical camera image of microneedles integrated on the array of heaters and a temperature sensor. **b**, HPLC analysis data of drug concentrations during the thermo-responsive drug release of Fig. 3.19b. **c**, Temperature monitoring of the heater by using a commercial infrared camera and the integrated temperature sensor. **d**, Step-wise thermal actuation of microneedles by using the 4 channel heater array. This enables the multi-step drug release. **e**, Optical camera images of the step-wise dissolution of microneedles corresponding to the thermal actuation in Fig. 3.21d.

3.4 Conclusion

We report soft materials, device designs, and system integration strategies for a novel class of diabetes monitoring and therapy devices based on functionalized CVD graphene. Graphene biochemical sensors with solid-state Ag/AgCl counter electrodes show the enhanced electrochemical activity, sensitivity, and selectivity to detect important biomarkers contained in the human sweat. Graphene-hybrid interconnections and physical sensors efficiently transmit the signal through the stretchable array and supplement electrochemical sensors, respectively. The orchestrated monitoring of biomarkers and physiological cues with the sweat-control and transcutaneous drug delivery achieves the closed-loop, point-of-care treatment of diabetes. Detection of the humidity over a critical point due to the sweat begins the glucose sensing, which is corrected by simultaneous measurement of pH and temperature. A high glucose concentration triggers embedded heaters to dissolve PCM and thus bioresorbable microneedles containing Metformin as a feedback transdermal drug delivery to the glucose sensing. The use of intrinsically soft materials enhances the conformal integration of devices with the human skin and thus improves the effectiveness of biochemical sensors and drug delivery. The wireless connectivity further highlights the practical

applicability of the current patch system. These advances using nanomaterials and their devices provide new opportunities for the treatment of chronic diseases, such as diabetes mellitus.

References

- 1 Kim, K. S. *et al.* Large-scale pattern growth of graphene films for stretchable transparent electrodes. *Nature* **457**, 706-710 (2009).
- 2 Bae, S. *et al.* Roll-to-roll production of 30-inch graphene films for transparent electrodes. *Nature Nanotechnol.* **5**, 574-578 (2010).
- 3 Lee, C., Wei, X., Kysar, J. W. & Hone, J. Measurement of the elastic properties and intrinsic strength of monolayer graphene. *Science* **321**, 385-388 (2008).
- 4 Schwierz, F. Graphene transistors. *Nature Nanotechnol.* **5**, 487-496 (2010).
- 5 Bonaccorso, F., Sun, Z. & Ferrari, A. C. Graphene photonics and optoelectronics. *Nature Photon.* **4**, 611-622 (2010).
- 6 Sun, Q. *et al.* Transparent, low-power pressure sensor matrix based on coplanar-gate graphene transistors. *Adv. Mater.* **26**, 4735-4740 (2014).
- 7 Lee, W. H. *et al.* Transparent flexible organic transistors based on monolayer graphene electrodes on plastic. *Adv. Mater.* **23**, 1752-1756 (2011).
- 8 Chung, C. *et al.* Biomedical applications of graphene and graphene oxide. *Acc. Chem. Res.* **46**, 2211-2224 (2011).

- 9 Duy, L. T. *et al.* High performance three-dimensional chemical sensor platform using reduced graphene oxide formed on high aspect-ratio micro-pillars. *Adv. Funct. Mater.* **25**, 883-890 (2015).
- 10 Kim, D.-J. *et al.* Electrical graphene aptasensor for ultra-sensitive detection of anthrax toxin with amplified signal transduction. *Small.* **9**, 3352-3360 (2013).
- 11 Park, D.-W. *et al.* Graphene-based carbon-layered electrode array technology for neural imaging and optogenetic applications. *Nature Commun.* **5**, 5258 (2014).
- 12 Han, T.-H. *et al.* Extremely efficient flexible organic light-emitting diodes with modified graphene anode. *Nature Photon.* **6**, 105-110 (2012).
- 13 Xu, L. *et al.* 3D multifunctional integumentary membranes for spatiotemporal cardiac measurements and stimulation across the entire epicardium. *Nat. Commun.* **5**, 3329 (2014).
- 14 Guinovart, T. *et al.* A potentiometric tattoo sensor for monitoring ammonium in sweat. *Analyst* **138**, 7031-7038 (2013).
- 15 Jia, W. *et al.* Electrochemical tattoo biosensors for real-time noninvasive lactate monitoring in human perspiration. *Anal. Chem.* **85**, 6553-6560 (2013).

- 16 Bandodkar, A. J. *et al.* Tattoo-based noninvasive glucose monitoring: a proof-of-concept study. *Anal. Chem.* **87**, 394-398 (2015).
- 17 Tee, B. C-K. *et al.* An electrically and mechanically self-healing composite with pressure- and flexion-sensitive properties for electronic skin applications. *Nature Nanotechnol.* **7**, 825-832 (2012).
- 18 Schwartz, G. *et al.* Flexible polymer transistors with high pressure sensitivity for application in electronic skin and health monitoring. *Nat. Commun.* **4**, 1859 (2013).
- 19 Mineev, I. R. *et al.* Electronic dura mater for long-term multimodal neural interfaces. *Science* **347**, 159-163 (2015).
- 20 Gerratt, A. P. *et al.* Elastomeric electronic skin for prosthetic tactile sensation. *Adv. Funct. Mater.* **25**, 2287-2295 (2015).
- 21 Son, D. *et al.* Multifunctional wearable devices for diagnosis and therapy of movement disorders. *Nature Nanotechnol.* **9**, 397-404 (2014).
- 22 Kim, J. *et al.* Stretchable silicon nanoribbon electronics for skin prosthesis. *Nat. Commun.* **5**, 5747 (2014).
- 23 Moyer, J., Wilson, D., Finkelshtein, I., Wong, B. & Potts, R. Correlation between sweat glucose and blood glucose in subjects with diabetes. *Diabetes Technol. Ther.* **14**, 398-402 (2012).

- 24 Sakaguchi, K. *et al.* Evaluation of a minimally invasive system for measuring glucose area under the curve during oral glucose tolerance tests: usefulness of sweat monitoring for precise Measurement. *J. Diabetes Sci. Technol.* **7**, 678-688 (2013).
- 25 Olarte, O., Chilo, J., Pelegri-Sebastia, J., Barbé, K. & Moer, W. V. Glucose detection in human sweat using an electronic nose. *Conf. Proc. IEEE Eng. Med. Biol. Soc.* **2013**, 1462-1465 (2013).
- 26 Sullivan, S. P. *et al.* Dissolving polymer micro-needle patches for influenza vaccination. *Nature Med.* **16**, 915-920 (2010).
- 27 Sullivan, S. P. *et al.* Minimally invasive protein delivery with rapidly dissolving polymer microneedles. *Adv. Mater.* **20**, 933-938 (2008).
- 28 Hyun, D. C. *et al.* Emerging applications of phase-change materials (PCMs): teaching an old dog new tricks. *Angew. Chem. Int. Ed.* **53**, 3780-3795 (2014).
- 29 Xu, S. *et al.* Soft microfluidic assemblies of sensors, circuits, and radios for the skin. *Science* **344**, 70-74 (2014).
- 30 Jang, K.-I. *et al.* Soft network composite materials with deterministic and bio-inspired designs. *Nat. Commun.* **6**, 6566 (2015).
- 31 Lacour, S. P. *et al.* Stretchable gold conductors on elastomeric substrates. *Appl. Phys. Lett.* **82**, 2404-2406 (2003).

- 32 Cao, Q. *et al.* Highly bendable, transparent thin-film transistors that use carbon-nanotube-based conductors and semiconductors with elastomeric dielectrics. *Adv. Mater.* **18**, 304-309 (2006).
- 33 Guo, C. G. *et al.* Highly stretchable and transparent nanomesh electrodes made by grain boundary lithography. *Nat. Commun.* **5**, 3121 (2014).
- 34 Vandeparre, H. *et al.* Localization of folds and cracks in thin metal films coated on flexible elastomer foams. *Adv. Mater.* **25**, 3117-3121 (2013).
- 35 Kaltenbrunner, M. *et al.* An ultra-lightweight design for imperceptible plastic electronics. *Nature* **499**, 458-463 (2013).
- 36 Sekitani, T., Zschieschang, U., Klauk, H. & Someya, T. Flexible organic transistors and circuits with extreme bending stability. *Nature Mater.* **9**, 1015-1022 (2010).
- 37 Sekitani, T. *et al.* Organic nonvolatile memory transistors for flexible sensor arrays. *Science* **326**, 1516-1519 (2009).
- 38 Ismail-Beigi, F. Glycemic management of type 2 diabetes mellitus. *N. Engl. J. Med.* **366**, 1319-1327 (2012).
- 39 Hallett, M. Classification and treatment of tremor. *JAMA.* **266**, 1115-1117 (1991).

- 40 Bailey, C. J., Path, M. R. C & Turner, R. C. Metformin. *N. Engl. J. Med.* **334**, 574-579 (1996).
- 41 Lee, J. W., Park, J.-H. & Prausnitz, M. R. Dissolving microneedles for transdermal drug delivery. *Biomaterials* **29**, 2113-2124 (2008).
- 42 Kochhar, J. S. *et al.* Microneedle integrated transdermal patch for fast onset and sustained delivery of lidocaine. *Mol. Pharm.* **10**, 4272-4280 (2013).
- 43 Cai, B., Xia, W., Bredenberg, S. & Engqvist, H. Self-setting bioceramic microscopic protrusions for transdermal drug delivery. *J. Mater. Chem. B* **2**, 5992-5998 (2014).
- 44 Scarbrough, C. A., Scarbrough, S. S. & Shubbrook J. Transdermal delivery of metformin. US Patent 13/504, 799 filed 12, May, 2010, and issued 16, Jul, 2012.
- 45 Prausnitz, M. R. & Langer, R. Transdermal drug delivery. *Nature Biotechnol.* **26**, 1261-1268 (2008).
- 46 Knowler, W. C. *et al.* Reduction in the incidence of type 2 diabetes with lifestyle intervention or metformin. *N. Engl. J. Med.* **346**, 393-403 (2002).

Chapter 4. Wearable/disposable sweat glucose monitor for non-invasive blood glucose monitoring

3.1 Introduction

Diabetes is one of the most prevalent chronic diseases, causing uncontrollable blood glucose levels¹. Patients with diabetes are advised to check their blood glucose level daily and take periodic insulin shots for continuous management of their blood glucose level². However, patients often do not follow this recommendation because of the pain and accompanying intense stress of repetitive blood collection and insulin shots. This leads to various severe diabetic complications, such as cardiovascular and kidney diseases, stroke, blindness, and nerve degeneration. In addition, insulin overtreatment causes an abrupt drop in the blood glucose concentration, which may cause seizures, unconsciousness, and even death. Therefore, a novel method for painless and stress-free glucose monitoring³⁻⁵ is highly desired.

The estimation of the blood glucose concentration based on the sweat-based glucose measurement is a potential solution^{6,7}. However, many challenges still exist for the accurate sweat-based glucose measurement^{8,9}. For example, the sweat collection procedure is tedious, and the sweat collection times vary depending on the environmental conditions. In addition to the difficulty of measuring glucose levels in sweat because of its much smaller concentration than that in blood, lactic acid in sweat, ambient temperature changes, and various medications induce errors in the enzyme-based glucose sensing. Mechanical friction and deformations of devices on the soft human skin can delaminate the enzyme from the glucose sensor, and cause mechanical fractures in devices.

In this study, we develop a patch-based wearable/strip-type disposable system for noninvasive sweat glucose monitoring. Key advantages of the developed system include i) a miniaturized sensor design that allows measurement with an infinitesimal amount of sweat, ii) multiple sweat control and uptake layers for efficient sweat collection, iii) a porous gold nanostructure to maximize the electrochemically active surface area and robustly immobilize the enzyme, iv) multi-modal glucose sensing with real-time correction based on pH and temperature monitoring for enhanced accuracy. This novel system for high-fidelity sweat glucose measurement

enables efficient management of blood glucose concentration without pain and stress.

3.2 Experimental Section

Fabrication process of the device array: The wearable device fabrication begins with spin-coating of the PI precursor ($\sim 1.5\ \mu\text{m}$, Product #575798, Sigma-aldrich, USA) on a SiO_2 wafer followed by thermal curing of the PI. A Cr/Au thin film ($\sim 30\ \text{nm}/\sim 70\ \text{nm}$) is deposited on electrodes by thermal evaporation. The Cr/Au thin film is patterned through photolithography and wet etching. A Cr/Pt thin film ($\sim 10\ \text{nm}/\sim 100\ \text{nm}$) is deposited by sputtering and patterned using photolithography for the temperature sensor and the counter electrode of the glucose sensor. The top epoxy layer ($\sim 1.5\ \mu\text{m}$; SU8-2, Microchem, USA) is coated and patterned with photolithography. The bottom PI layer is selectively isolated by photolithography and reactive ion etching. The device is transfer-printed onto a PDMS substrate (Sylgard 184, Dow chemical, USA) by using a water soluble tape (Product #5414, 3M, USA). The strip-type device is fabricated on the PI film ($125\ \mu\text{m}$; isoflex, Republic of Korea) with the same procedures.

Functionalization of sensors and electrodes with electrochemically active materials: i) PEDOT electrodeposition: A solution of $0.01\ \text{M}$ 3,4-ethylenedioxythiophene (Product #483028, Sigma-Aldrich, USA) and $0.1\ \text{M}$

LiClO₄ (Product #271004, Sigma-Aldrich, USA) in acetonitrile (Product #271004, Sigma-Aldrich, USA) is prepared. The gold electrode is dipped into the solution, and galvanostatic electrodeposition is performed for 40 s at 1.2 V (potential vs. commercial Ag/AgCl electrode).

ii) Ag/AgCl electrodeposition: An aqueous solution of 5 mM AgNO₃ (Product #209139, Sigma-Aldrich, USA) and 1 M KNO₃ (Product #P8394, Sigma-Aldrich, USA) is prepared. The gold electrode is dipped into the prepared solution. The potential is swept from -0.9 to 0.9 V versus an Ag electrode for 14 segments at a scan rate of 0.1 V s⁻¹. For chlorination, the electrode is dipped in an aqueous solution of 0.1 M KCl (Product #P5405, Sigma-Aldrich, USA) and 0.01 M HCl (Product #H1758, Sigma-Aldrich, USA). The potential is swept from -0.15 to 1.05 V versus a commercial Ag/AgCl electrode for 4 segments at a scan rate of 0.05 V s⁻¹.

iii) Porous gold electrodeposition: An aqueous solution of 2 mM HAuCl₄ (Product #70-0500, STERM chemical, USA) in 2 M H₂SO₄ (Product #320501, Sigma-Aldrich, USA) is prepared. The gold electrode is dipped into the prepared solution. The porous gold is electrodeposited by the galvanostatic method for 5 min at -1 V with a Pt counter electrode and a commercial Ag/AgCl electrode (total charge: ~0.5 C).

iv) Prussian blue electrodeposition: An aqueous solution of 10 mM KCl, 2.5

mM $\text{K}_3[\text{Fe}(\text{CN})_6]$ (Product #P702587, Sigma-Aldrich, USA), and 2.5 mM $\text{FeCl}_3 \cdot 6\text{H}_2\text{O}$ (Product #236489, Sigma-Aldrich, USA) in 0.1 M HCl is prepared. The gold electrode is dipped into the solution and the potential is swept from -0 to 0.5 V versus a commercial Ag/AgCl for 2 segments at a scan rate of 0.02 V s^{-1} .

v) GOx immobilization: 1 wt% chitosan (Product #C3646, Sigma-Aldrich, USA) solution is prepared by dissolving chitosan in 2 wt% acetic acid (Product #695092, Sigma-Aldrich, USA). The chitosan solution is mixed with an exfoliated graphite (Product #282863, Sigma-Aldrich, USA) solution (2 mg mL^{-1}) in 1X phosphate-buffered saline (Dulbecco's PBS, WELGENE Inc., Republic of Korea). The chitosan/graphene solution is mixed with 0.05 g mL^{-1} GOx (Product #G7141, Sigma-Aldrich, USA) and 0.01 g mL^{-1} bovine serum albumin (Product #A2153, Sigma-Aldrich, USA). A solution of 0.05 g mL^{-1} GOx and 0.01 g mL^{-1} bovine serum albumin is also prepared in 1X PBS. $0.8 \mu\text{L}$ of GOx and BSA in a PBS solution is drop-casted on the porous gold-deposited electrode. After drying the electrodes, $0.8 \mu\text{L}$ of GOx in the chitosan/graphene solution is drop-casted on the electrode. After drying the electrodes, $2 \mu\text{L}$ of 0.5 wt% Nafion (Product #309389, Sigma-Aldrich, USA) is drop-casted on the glucose sensor. After drying of Nafion, $0.8 \mu\text{L}$ of 2 wt% glutaraldehyde (Product #G5882, Sigma-

Aldrich, USA) is drop-casted on the glucose sensor for cross-linking of the enzyme layer.

vi) PANi electrodeposition: An aqueous solution of 0.1 M aniline (Product #242284, Sigma-Aldrich, USA) in 1 M HCl is prepared. The gold electrode is dipped into the solution, and the potential is swept from -0.2 to 1 V versus a commercial Ag/AgCl electrode for 60 segments at a scan rate of 0.1 V s^{-1} .

Characterization of the humidity sensor: The humidity sensor is calibrated using the AC impedance method with an electrochemical analyzer (CHI660E, CHI Instruments, USA). Measurements are performed by the two-electrode method by using PEDOT-deposited interdigitated electrodes. The humidity sensor is calibrated by measuring its impedance changes and adding an artificial sweat solution. The impedance–time measurements are used for real-time humidity monitoring.

Characterization of the glucose sensor: i) Calibration process: The glucose sensor is characterized by the galvanostatic method with an electrochemical analyzer (CHI660E, CHI Instruments, USA). The three-electrode method is used for the measurement. The three electrodes include an enzyme layer/PB/porous gold-deposited working electrode, a Pt counter electrode,

and an Ag/AgCl reference electrode. The galvanostatic measurement is conducted at an initial potential of -0.2 V for 20 s for each measurement using the artificial sweat solution with glucose concentrations from 0 to 1 mM (Product #G5767, Sigma-Aldrich, USA) in 1X PBS (Dulbecco's phosphate-buffered saline, WELGENE Inc., Republic of Korea).

ii) Other characterizations: Other characterizations are performed by the same procedure of the calibration process. The stretching test is conducted under 0–20 % applied strains. The temperature dependency of the glucose sensor is tested with the artificial sweat solution between 20 and 45 °C. The selectivity of the glucose sensor is tested with the solution of PBS, 0.1 mM glucose, 10 μ M ascorbic acid (Product #A7506, Sigma-Aldrich, USA), 59 μ M uric acid (Product #U2625, Sigma-Aldrich, USA), 4 mM lactic acid (Product #69775, Sigma-Aldrich, USA), 132 μ M acetaminophen (Product #A7085, Sigma-Aldrich, USA), 555 μ M acetylsalicylic acid (Product #A5376, Sigma-Aldrich, USA), and 774 μ M metformin (Product #D150959, Sigma-Aldrich, USA). For long-term stability, the glucose sensor is tested under ambient temperature and stored under 4 °C when it is not used. The pH dependency of the glucose sensor is estimated with the artificial sweat solution at pH values of 4 to 7.

Characterization of the pH sensor: The pH sensor is characterized through the open circuit potential (OCP) measurement with an electrochemical analyzer (CHI660E, CHI Instruments, USA). The two-electrode method is used for the measurement. The two electrodes are a PANi-deposited working electrode and an Ag/AgCl-deposited counter electrode. The pH sensor is calibrated using standard buffered pH solutions (pH of buffered solutions from 4 to 7, Alfa Aesar, USA). The stretching test is conducted under 0–20 % applied strains. The temperature dependency of the pH sensor is tested between 20 °C and 45 °C.

Characterization of the heater and temperature sensor: The heater temperature is controlled by the power supply module (U8031A, Agilent, USA). The temperature is monitored with an IR camera (FLIR E8, FLIR, USA). The temperature sensors in the wearable sweat glucose sensors and the transdermal drug delivery device are calibrated using a semiconductor device analyzer (B1500A, Agilent, USA).

Human sweat analysis: Human sweat study is performed in compliance with the protocol approved by the institutional review board at the Seoul National University (IRB No. 1605/003-002). Five healthy subjects, aged

20–60 years, participated in the study. All subjects are informed of the risks and benefits, and they provided informed consent. For obtaining the correlation factor between glucose levels in sweat and blood, the blood glucose level is tested using a commercial glucose meter (Accu-Check Performa, Roche, Switzerland) 1 h before and after a meal. After testing the blood glucose level, a sweat monitoring patch is attached on the skin to monitor sweat hydration, glucose/pH levels, and temperature while the subject uses a cycle ergometer. The sweat monitoring patch is integrated with a sweat-uptake layer (Half sponge sheet, Swisspure, Republic of Korea) and a water-proof layer (Tegaderm 1624W, 3M, USA) for efficient sweat collection. For the electrochemical measurement, the sweat monitoring patch is connected to a portable electrochemical analyzer (PalmSens3, Palm instrument B.V., Netherlands) via an anisotropic conductive film (HST-9805-210, Elform, USA). To examine the accuracy of the sweat glucose monitoring result, the glucose level measured from the patch is compared with a glucose level measured by a commercial glucose assay (Glucose assay kit, Cayman chemical, USA).

3.3 Result and Discussion

3.3.1 System design of the wearable diabetes patch and disposable strip

The patch-based devices have ultrathin¹⁰⁻¹² and stretchable design^{13,14} (Figs. 4.1a and b), which enable conformal contact with the skin for efficient sweat collection and high performance under physical deformations^{15,16}. The same sensors can be further miniaturized and fabricated as a disposable strip (Fig. 4.2). Depending on the sweat glucose concentration, an appropriate amount of metformin (or chlorpropamide) is transdermally delivered through microneedles. The drug delivery can be thermally controlled in a multi-stage manner. These patch-type devices are fabricated on a handle substrate and then transfer-printed onto a thin silicone patch (Fig. 4.3). The strip-type sensor is fabricated on a thin polyimide (PI) substrate. Patterned electrochemical functionalization completes the fabrication.

After wearing the patch, sweat accumulates in the porous sweat-uptake layer. A water-proof band behind the silicone patch aids in sweat collection and prevents delamination of the patch from the skin. A Nafion

layer between the sensors and the sweat-uptake layer helps in the immobilization of the enzyme¹⁸ and screens out molecules that could interfere with glucose sensing^{18,19} (*e.g.*, drug molecules contained in sweat such as acetaminophen or acetylsalicylic acid). A humidity sensor monitors the critical amount of sweat for reliable glucose sensing. Above the critical humidity, the glucose, the pH, and temperature sensors begin measurements. The pH and temperature sensors correct potential errors of the enzyme-based glucose sensing in real time. Upon hyperglycemia, thermal actuation controls the feedback transdermal delivery of metformin loaded in PCNs.

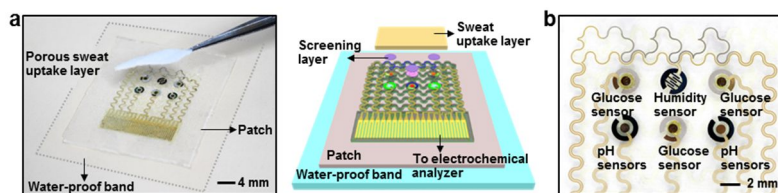


Figure 4.1. Images and system design of wearable sweat monitoring patch. **a**, Optical camera image (left; dotted line: edges of the patch) and schematic illustration (right) of the wearable sweat monitoring patch. A porous sweat-uptake layer is placed on a Nafion layer and sensors. **b**, Optical camera image of wearable sweat analysis sensors.

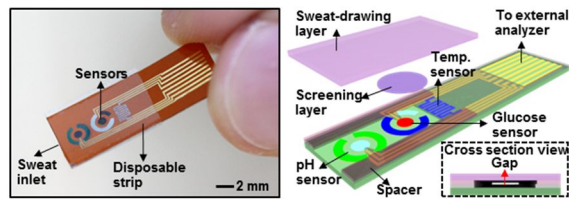


Figure 4.2. Images and system design of disposable sweat monitoring strip. Optical camera image (left) and schematic illustration (right) of the disposable sweat monitoring strip.

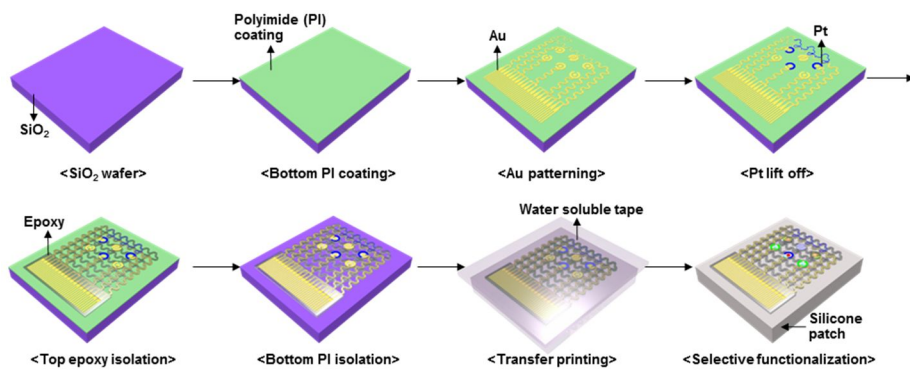


Figure 4.3. Device fabrication process. Schematic illustration of the fabrication process of the sweat analysis sensors.

3.3.2 Materials and key device design

A series of stretchable sensors (humidity, glucose, pH, and temperature) are monolithically integrated (Fig. 4.1a) for efficient sweat-based glucose sensing. Multi-point sensing for glucose (triple) and pH (quadruple) improves the detection accuracy (Fig. 4.1b). In the glucose and pH sensors, the reference and counter electrodes are designed to be packed as closely as possible to minimize the required amount of sweat (Fig. 4.4a). As the working electrode diameter (D_{work}) decreases, the required sweat amount can be reduced to as small as 1 μL (Fig. 4.4b), which is a 20 fold decrease from the previous report⁵. The working electrode consists of porous gold formed by electrodeposition and enzymes (glucose oxidase) cross-linked on it by drop casting (Fig. 4.4c). The porous structure allows for a larger electrochemically active surface area^{21,22} and stronger enzyme immobilization^{22,24}. Cyclic voltammograms (CV) (Fig. 4.5a) and alternating current (AC) impedance measurements (Figs. 4.5b and c) using the $\text{Fe}(\text{CN})_6^{3-/4-}$ redox couple show a high charge storage capacity and low interfacial impedance in the porous structure. High H_2O_2 reducing catalytic activity of the porous structure (Fig. 4.5d) confirms the enhanced sensitivity. Robustly cross-linked enzymes on the porous metal structure also enhance

the reliability of the sensor under mechanical friction and deformations.

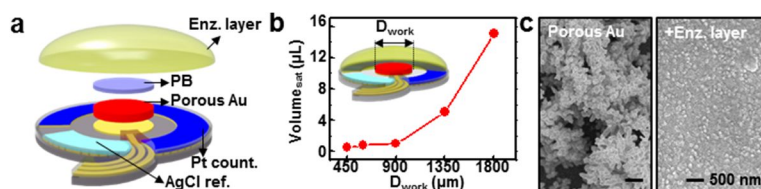


Figure 4.4. Miniaturization and electrode design of the glucose sensor. a, Schematic drawing of the glucose sensor in an exploded view. **b,** Minimum volume of the artificial sweat required for the sensing with different sizes of the glucose sensor. **c,** SEM images before (left) and after (right) immobilization of the enzyme on the porous gold electrode.

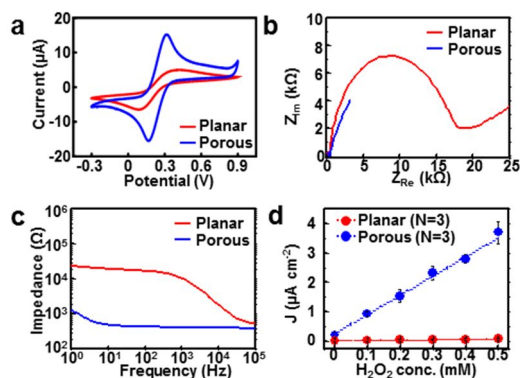


Figure 4.5. Electrochemical analysis of the planar and porous gold electrode. **a**, CV plots of the planar and porous gold electrode in PBS with $\text{Fe}(\text{CN})_6^{3-/4-}$. **b**, Nyquist plots of the planar and porous gold electrode in PBS with $\text{Fe}(\text{CN})_6^{3-/4-}$ at the equilibrium potential used in Fig. 4.5a. **c**, Bode plots of the planar and porous gold electrode in PBS with $\text{Fe}(\text{CN})_6^{3-/4-}$ at the equilibrium potential used in Fig. 4.5a. **d**, Comparison of the H_2O_2 sensitivity in the planar and porous gold electrode deposited with Prussian Blue at different H_2O_2 concentrations.

3.3.3 Sweat control optimization

Efficient use of the generated sweat is an important issue in the sweat-based monitoring system, which is enabled by the sweat-uptake layer and water-proof layer. A porous and hydrophilic sweat-uptake layer^{24,25} (Fig. 4.6a inset), which is placed on the Nafion layer and sensors, absorbs sweat, and delivers it to the sensors through the Nafion layer (Fig. 4.6b). The water-proof band added on the elastomeric silicone patch covers the outside to separate the sweat from external humidity (Fig. 4.6a), suppresses sweat evaporation (Fig. 4.6c), and prevents delamination of the patch during skin deformations (Fig. 4.6d). The strip-type sensor absorbs sweat by the capillary force formed by the gap (fluidic channel) between the sweat-drawing layer and substrate (Figs. 4.2 bottom inset and 4.7). The miniaturized sensor design (Figs. 4.4a and b) and the fast collection of sweat enable rapid sensing. The miniaturized glucose sensor can be stably operated with only 1 μL of sweat (Fig. 4.8a-c).

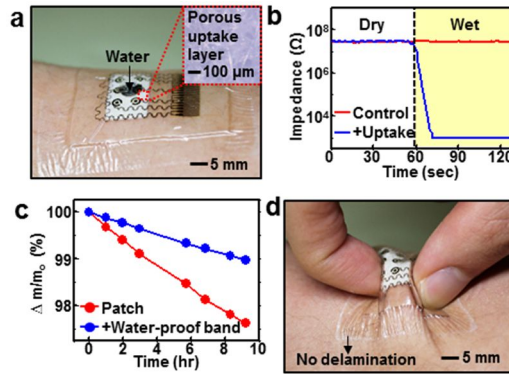


Figure 4.6. Sweat control layers. **a**, Optical image of the wearable sweat analysis patch with a sweat-uptake layer and a water-proof band. The inset shows the magnified view of the porous sweat-uptake layer. **b**, Impedance change of the humidity sensor with (blue) and without (red) sweat uptake layer during addition of artificial sweat. **c**, Relative mass change of water by evaporation with (blue) and without (red) the water-proof band. **d**, Optical image of the sweat analysis patch under deformation.

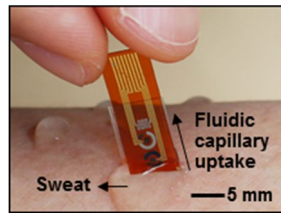


Figure 4.7. Sweat absorption of the disposable sweat analysis strip.

Optical image of the disposable sweat analysis strip on the human skin with perspiration.

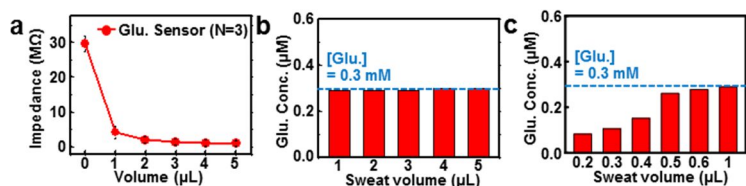


Figure 4.8. Reliable operation of the glucose sensor with small volume of sweat. **a**, Impedance change of the glucose sensor at different volumes of the artificial sweat solution. **b**, Galvanostatic measurement of the glucose sensor at different sweat volumes (sweat volume over 1 μL , 0.3 mM artificial sweat). **c**, Galvanostatic measurement of the glucose sensor at different sweat volumes (sweat volume below 1 μL , 0.3 mM artificial sweat).

3.3.4 Electrochemical and electrical characterization of individual sensors

The humidity sensor monitors the sweat collection procedure through impedance changes of poly(3,4-ethylenedioxythiophene) (PEDOT) interdigitated electrodes to estimate an appropriate starting point of sweat analysis (Fig. 4.9). The glucose sensor based on a Prussian blue-deposited porous gold electrode is calibrated to the glucose concentration range between 10 μ M and 1 mM (typical glucose concentrations in human sweat) by a galvanostatic method (Figs. 4.10a-d). The glucose sensor is stable under mechanical deformations (Fig. 4.11a) and selectively detects glucose in the presence of other biomolecules (*e.g.*, ascorbic, uric, and lactic acid) and drugs (*e.g.*, acetaminophen, acetylsalicylic acid, and metformin) (Fig. 4.11b) contained in the sweat. The glucose sensor works for one full day without additional calibration under ambient conditions and for several days depending on storage conditions (Fig. 4.11c).

The enzyme-based glucose sensor shows deviations at different pH levels (Fig. 4.11d) and thus simultaneous monitoring of pH levels is important. The pH sensor measures changes in the open circuit potential (OCP) between a polyaniline (PANI)-deposited working electrode and an

Ag/AgCl electrode. The pH sensor is calibrated using standard pH buffer solutions (Figs. 4.12a and b) and maintains stable operation under deformations (Fig. 4.12c). The pH sensor is reliable over repeated use at different pH levels (Fig. 4.12d) and at different temperatures (Fig. 4.12e). The resistor-based temperature sensor is also calibrated for skin temperature monitoring (Fig. 4.13). The simultaneous use of these co-integrated sensors can enhance the accuracy of glucose sensing. For example, metabolic secretion of lactic acid in sweat lowers the pH level to 4–5. The simultaneous pH sensing can correct this pH-dependent deviation (Figs. 4.12e and 4.14a) of the enzyme-based glucose sensor. Simulated hyperglycemia—0.3 mM of sweat glucose concentration—is monitored *in vitro* under two different pH variation settings (5→4→5 and 5→6→5; Figs. 4.14b left and right). In both cases, real-time correction increases glucose measurement accuracy. The glucose sensor with the current device setting does not show significant deviations at different temperatures (Fig. 4.14c).

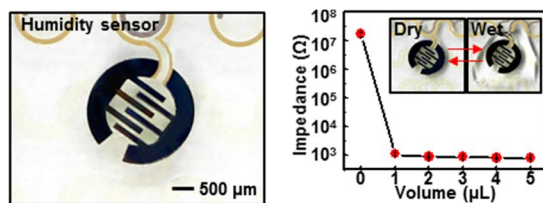


Figure 4.9. Characterization of the humidity sensor. Optical image (left) and calibration curve (right) of the humidity sensor (number of sample = 3). Inset shows an image before and after wetting of the sensor.

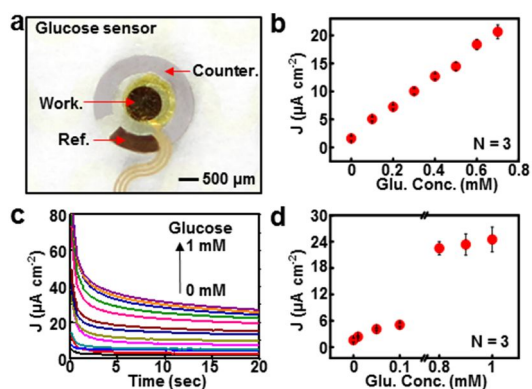


Figure 4.10. Characterization of the glucose sensor. **a**, Optical image of the glucose sensor. **b**, Calibration curve of glucose sensor. **c**, Calibration curves of the glucose sensor in artificial sweat solutions (glucose concentration: from 0 to 1 mM). **d**, Detection limit of the glucose sensor.

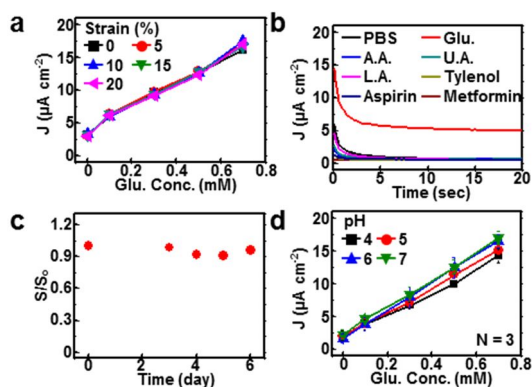


Figure 4.11. Characterization of the glucose sensor. a, Calibration curves of the glucose sensor at different applied strains. **b,** Selectivity of the glucose sensor (PBS, 0.1 mM Glucose (Glu.), 10 μM ascorbic acid (A.A.), 59 μM uric acid (U.A.), 4 mM lactic acid (L.A.), 132 μM acetaminophen (Acetami.), 555 μM acetylsalicylic acid (Acetyl.), and 774 μM Metformin). **c,** Long-term stability of the glucose sensor. **d,** pH dependency of the glucose sensor.

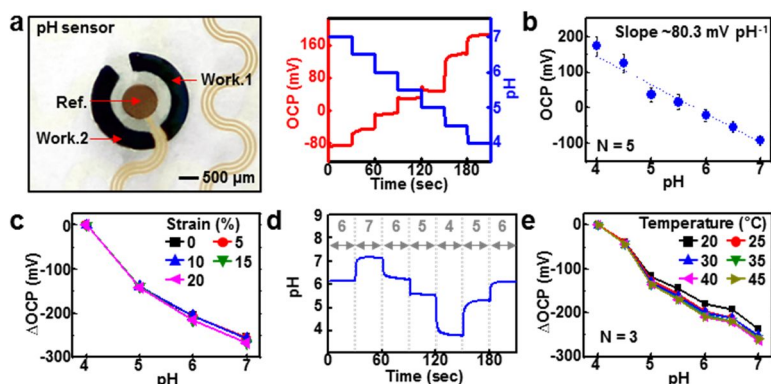


Figure 4.12. Characterization of the pH sensor. **a**, Optical image (left) and calibration curve (right) of the pH sensor. **b**, Open circuit potential changes of the pH sensor. **c**, pH-dependent OCP changes of the pH sensor at different applied strains. **d**, Characterization of the pH sensor in standard buffered solutions whose pH changes are 6→7→6→5→4→5→6. **e**, Open circuit potential changes of the pH sensor at different temperatures.

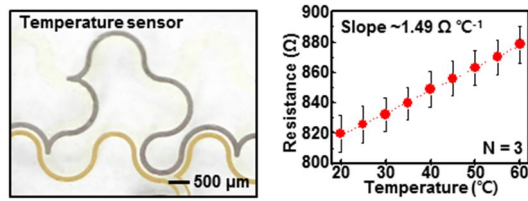


Figure 4.13. Characterization of the temperature sensor. Optical image (left) and calibration curve (right) of the temperature sensor.

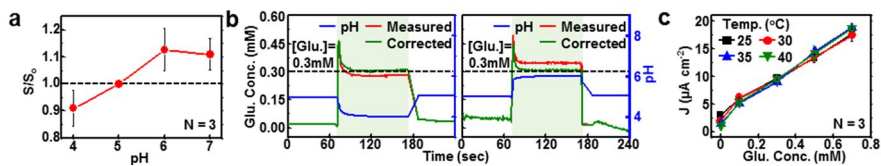


Figure 4.14. Effect of pH and temperature variation on the glucose sensor. **a**, Changes of relative sensitivity of the uncorrected glucose sensor at different pH. **b**, *In vitro* monitoring of the glucose change with (green) and without (red) correction using simultaneous pH measurement (blue). **c**, Calibration curves of the glucose sensor at different temperatures.

3.3.5 Sweat monitoring from human subjects

Wearable/disposable sweat-based glucose sensors are employed for human sweat analysis. The wearable patch is connected to a portable electrochemical analyzer (Figs. 4.15a and b). The monitoring starts with humidity sensing (Fig. 4.16a). When the sweat-uptake layer absorbs a sufficient amount of sweat, the glucose and pH sensors detect the sweat glucose and pH levels, respectively. The triple glucose and quadruple pH sensing (Fig. 4.1b) improve the detection accuracy (Fig. 4.16b). The correction using the measured pH enables more accurate glucose sensing (Fig. 4.16c). The patch works reliably under changes of skin temperature (minimum temperature: 30 °C, maximum temperature: 34 °C) during physical movements (Figs. 4.17a and b). The changes of skin temperature with the current experimental setting are small due to homeostatic functions of the nervous system²⁶. The patch is reusable and/or reattachable multiple times (Figs. 4.17c and d).

The disposable strip-type sensor is more convenient for the sweat analysis. The strip-type sensor first absorbs sweat (Fig. 4.7) due to the capillary effect. Then it is connected to the hardware for sweat analysis through a zero insertion force (ZIF) connector (Fig. 4.18a). The absorbed

sweat should cover the surface of both pH and glucose sensors (Fig. 4.18b). The amount of absorbed sweat can be monitored by measuring the impedance between the electrodes of the glucose sensor (Pt counter electrode and Ag/AgCl reference electrode) or those of the pH sensor (two PANi-deposited working electrodes) (Fig. 4.18c). When the sweat covers both glucose and pH sensors, the measurements begin (Fig. 4.18d). The calibration curves for a strip-type device are shown in Figs 4.18 e and f.

The sweat pH levels vary among subjects and depending on physiological conditions of each subject (Fig. 4.19a). The sweat glucose levels corrected by pH measurements before and after a meal agree well with the sweat glucose levels measured among subjects using a commercial glucose assay kit (Fig. 4.19b). The statistical analysis confirms the reliable correlation of sweat glucose levels measured by the wearable and disposable sweat glucose sensors with the blood glucose levels measured by a commercial glucose meter (Fig. 4.19c). As a result, the blood glucose concentration shows similar tendency with the measured sweat glucose concentration before and after a meal (Fig. 4.19d).

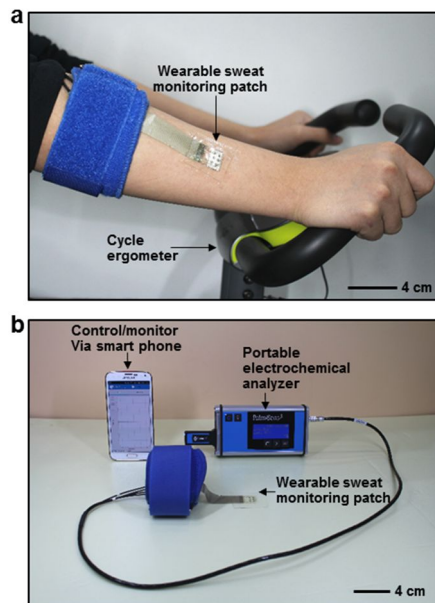


Figure 4.15. System set up for human sweat analysis by using wearable sweat monitoring patch. a, Optical camera image of the subject using a cycle ergometer for sweat generation after wearing the wearable patch. **b,** The wearable sweat monitoring patch is connected to the portable electrochemical analyzer that supplies the power and controls the patch. The portable electrochemical analyzer can communicate with commercial mobile devices wirelessly via Bluetooth.

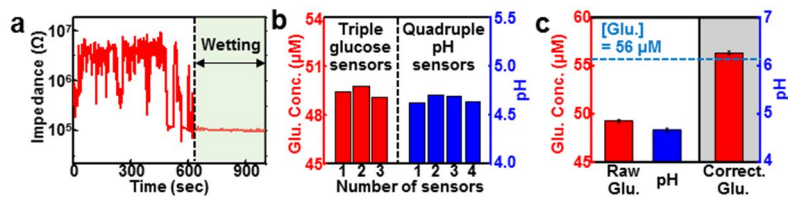


Figure 4.16. Human sweat monitoring by wearable sweat monitoring patch. **a**, Real-time humidity monitoring to check the accumulation of sweat. **b**, Multi-modal glucose and pH sensing to improve detection accuracy. **c**, Measured sweat glucose concentrations (N = 3), pH levels (N = 4), and corrected sweat glucose level (N = 3) based on the averaged pH (dotted line: glucose concentration measured by a commercial glucose assay).

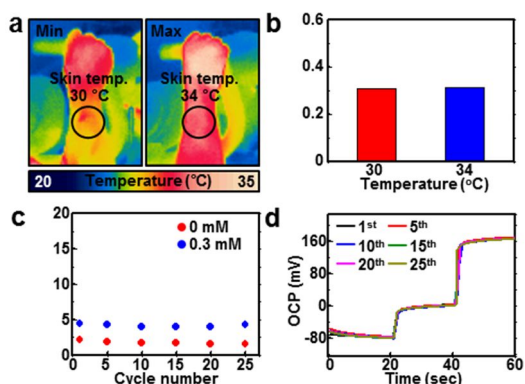


Figure 4.17. Temperature stability and reuse test of the wearable sweat monitoring patch. **a**, IR camera image of the human skin in using a cycle ergometer (minimum temperature: 30 °C, maximum temperature: 34 °C). **b**, Stable glucose sensing of the artificial sweat (0.3 mM) on 30 and 34 °C of the skin. **c**, Stable glucose sensing of the artificial sweat (0.1 mM) after multiple reuse. **d**, Stable pH sensing by using standard buffer solutions (pH 6→5→4) after multiple reuse.

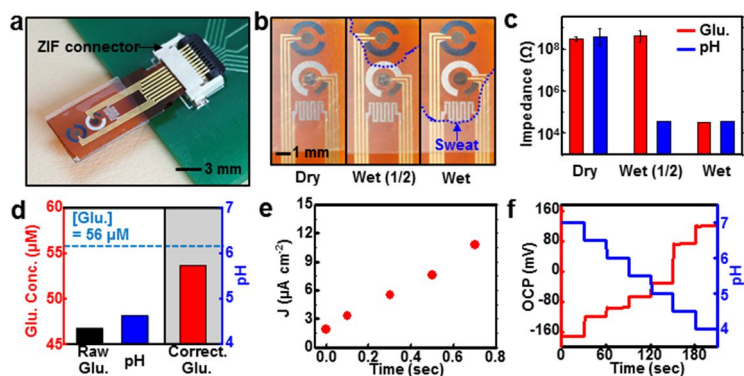


Figure 4.18. Human sweat monitoring by disposable sweat monitoring strip. **a**, Optical camera image of the disposable strip-type sensors connected to a ZIF connector. **b**, Optical camera images of the sweat uptake via the fluidic channel of the strip. **c**, Humidity monitoring of the disposable strip by using impedance measurements. **d**, Sweat glucose and pH monitoring by using the disposable strip. **e**, Calibration curves of the strip-type glucose sensor by using artificial sweat solutions. **f**, Calibration curves of the strip-type pH sensor.

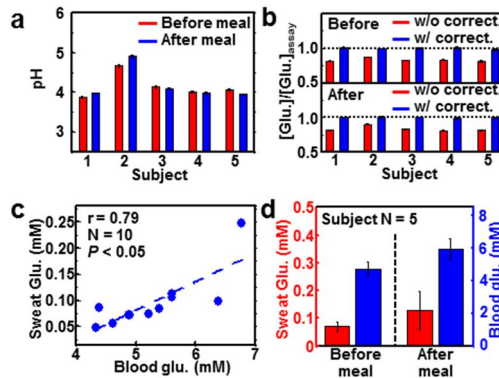


Figure 4.19. Human sweat analysis and correlation between glucose concentrations in sweat and blood. a, Measurement of pH levels ($N = 4$) in sweat from five subjects before and after a meal. **b,** Ratio of sweat glucose concentrations ($N = 3$) measured by the patch and a commercial glucose assay with and without the pH-based correction before and after a meal. **c,** Statistical analysis of the correlation between the sweat glucose concentrations and the blood glucose concentrations ($r = 0.79$, $P < 0.05$, Pearson's correlation test). **d,** Comparison of the sweat and blood glucose concentrations before and after a meal.

3.4 Conclusion

We report a novel material structure, device design, and system integration strategy for a sweat glucose monitoring device. Depending on the design, the device can be either wearable-patch type or disposable-strip type. For efficient sweat control and sensing, the sweat monitoring patch is assembled with multiple sweat-uptake and water-proof layers, and sensor sizes are miniaturized to the point that $\sim 1\ \mu\text{L}$ of sweat is sufficient for the reliable measurement. The measurement of sweat glucose levels with real-time correction based on pH, temperature, and humidity sensing are accurate under various environment changes. The sweat glucose data are well correlated with the blood glucose levels. Although there are still points to improve, the current sweat-based sensing provides important new advances toward the painless and stress-free point-of-care treatment of diabetes mellitus.

References

1. Whiting, D.R., Guariguata, L., Weil, C. & Shaw, J. IDF diabetes atlas: global estimates of the prevalence of diabetes for 2011 and 2030. *Diabetes Res. Clin. Pract.* **94**, 311-321 (2011).
2. Control, D. & Group, C.T.R. The effect of intensive treatment of diabetes on the development and progression of long-term complications in insulin-dependent diabetes mellitus. *N. Engl. J. Med.* **329**, 977-986 (1993).
3. Bandodkar, A.J. *et al.* Tattoo-based noninvasive glucose monitoring: a proof-of-concept study. *Anal. Chem.* **87**, 394-398 (2015).
4. Gao, W. *et al.* Fully integrated wearable sensor arrays for multiplexed in situ perspiration analysis. *Nature* **529**, 509-514 (2016).
5. Lee, H. *et al.* A graphene-based electrochemical device with thermoresponsive microneedles for diabetes monitoring and therapy. *Nature Nanotech.* **11**, 566-572 (2016).
6. Moyer, J., Wilson, D., Finkelshtein, I., Wong, B. & Potts, R. Correlation between sweat glucose and blood glucose in subjects with diabetes. *Diabetes Technol. Ther.* **14**, 398-402 (2012).
7. Sakaguchi, K. *et al.* Evaluation of a minimally invasive system for

- measuring glucose area under the curve during oral glucose tolerance tests: usefulness of sweat monitoring for precise measurement. *J. Diabetes Sci. Technol.* **7**, 678-688 (2013).
8. Vashist, S.K. Non-invasive glucose monitoring technology in diabetes management: a review. *Anal. Chim. Acta.* **750**, 16-27 (2012).
 9. Tierney, M., Kim, H., Burns, M., Tamada, J. & Potts, R. Electroanalysis of glucose in transcutaneously extracted samples. *Electroanalysis* **12**, 666-671 (2000).
 10. Kaltenbrunner, M. *et al.* An ultra-lightweight design for imperceptible plastic electronics. *Nature* **499**, 458-463 (2013).
 11. Sekitani, T., Zschieschang, U., Klauk, H. & Someya, T. Flexible organic transistors and circuits with extreme bending stability. *Nature Mater.* **9**, 1015-1022 (2010).
 12. Kim, J. *et al.* A wearable multiplexed silicon nonvolatile memory array using nanocrystal charge confinement. *Sci. Adv.* **2**, e1501101 (2016).
 13. Kim, D.-H. *et al.* Epidermal electronics. *Science* **333**, 838-843 (2011).
 14. Jang, K.I. *et al.* Soft network composite materials with deterministic and bio-inspired designs. *Nat. Commun.* **6**, 6566 (2015).
 15. Son, D. *et al.* Multifunctional wearable devices for diagnosis and therapy of movement disorders. *Nature Nanotech.* **9**, 397-404 (2014).

16. Kim, J. *et al.* Stretchable silicon nanoribbon electronics for skin prosthesis. *Nat. Commun.* **5**, 5747 (2014).
17. Zhang, M. *et al.* Highly sensitive glucose sensors based on enzyme-modified whole-graphene solution-gated transistors. *Sci. Rep.* **5**, 8311 (2015).
18. Hossain, M.F. & Park, J.Y. Plain to point network reduced graphene oxide-activated carbon composites decorated with platinum nanoparticles for urine glucose detection. *Sci. Rep.* **6**, 21009 (2016).
19. Zhang, Y. *et al.* Elimination of the acetaminophen interference in an implantable glucose sensor. *Anal. Chem.* **66**, 1183-1188 (1994).
20. Niu, Z. *et al.* A universal strategy to prepare functional porous graphene hybrid architectures. *Adv. Mater.* **26**, 3681-3687 (2014).
21. Wang, W. *et al.* Bioinspired nanosucker array for enhancing bioelectricity generation in microbial fuel cells. *Adv. Mater.* **28**, 270-275 (2016).
22. Pan, L. *et al.* Hierarchical nanostructured conducting polymer hydrogel with high electrochemical activity. *Proc. Natl. Acad. Sci.* **109**, 9287-9292 (2012).

23. Claussen, J.C. *et al.* Panostructuring platinum nanoparticles on multilayered graphene petal nanosheets for electrochemical biosensing. *Adv. Funct. Mater.* **22**, 3399-3405 (2012).
24. Huang, X. *et al.* Stretchable, wireless sensors and functional substrates for epidermal characterization of sweat. *Small* **10**, 3083-3090 (2014).
25. Rose, D.P. *et al.* Adhesive RFID sensor patch for monitoring of sweat electrolytes. *IEEE Trans. Biomed. Eng.* **62**, 1457-1465 (2015).
26. Nakamura, K., Morrison, S. F. A thermosensory pathway that controls body temperature. *Nat. Neurosci.* **11**, 62-71 (2008).

(요약) 국문초록

다기능성 수술용 내시경과 당 모니터링 시스템을 위한 집적된 전기화학적 센서와 엑추에이터 시스템 구현

지난 수년 동안 휘거나 늘일 수 있는 유연소자 기술은 생체 의학적 적용을 위하여 재료, 디자인, 그리고 공정과정측면에서 큰 발전을 해왔다. 유연 전자 소자의 물리적 특성은 소자와 부드럽고 비선형적인 생체 표면 사이의 본질적인 기계적 특성의 차이 문제를 해결하였다. 이를 바탕으로 비침습적인 소자, 최소 침습적인 소자, 바탕으로 입을 수 있는 소자로의 다양한 형태의 응용이 가능해졌다. 본 논문에서는 두 가지 예시로서 대장암과 당뇨병 진단 및 치료를 위한 두 가지 종류의 다기능성 전자소자 시스템을 다루고 있다.

첫째는 대장암의 최소 침습 수술을 위한 기기로서 다기능성 내시경을 소개한다. 그래핀 복합체 기반의 투명 전자소자를 활용하여 임피던스와 산성도 측정을 기반으로 대장암을 진단하고, 고주파 어블레이션을 활용하여 피드백 치료를 가능하게 하였다.

내시경에 결합된 투명 전자소자는 내시경 고유의 광학적 진단기능을 유지하면서도 추가적인 대장암의 진단과 치료를 가능하게 하였다.

둘째는 비침습적 혈당모니터링 패치 및 일회용 센서와 피드백 치료를 위한 마이크로니들 기반의 피부를 통한 약물전달 시스템을 소개한다. 땀 속 당 농도와 혈액 속 당 농도의 상관관계를 활용하여 비침습적인 혈당 분석을 할 수 하였다. 당 모니터링 패치는 산성도, 온도와 습도의 영향을 보정하여 정확한 땀 속 당의 농도를 확인할 수 있었다. 또한, 약물이 담지된 열감응성 마이크로 니들을 활용하여 열적자극으로 약물전달을 활성화 시켜 피부를 통한 선택적인 약물전달이 가능하게 하였다.

두 가지 종류의 다기능성 전자소자 시스템들을 통하여 진단에서부터 치료까지 가능한 통합적 접근법의 예시를 보여주었다. 체외실험과 동물실험을 통하여 개발한 시스템들의 대장암과 당뇨관리를 위한 유용성과 응용 가능성을 확인하였다.

주요어: 굽힐 수 있는 전자소자, 늘일 수 있는 전자 소자, 입을 수 있는 전자소자, 전기화학 센서, 내시경, 당 모니터링 시스템

학번: 2010-21007